INTERNATIONAL STRATEGY FOR DISASTER REDUCTION

Monitoring and Predicting Acceleration and Deceleration of Large Landslides Part of TU Wien

Final Report
2008 – 2013

Principal investigator: Em. Univ. Prof. Dr. Ewald Brückl
Reporter: Mag. Stefan Mertl

Department of Geodesy and Geoinformation
Vienna University of Technology
Vienna, January 2014

ISBN-Online: 978-3-7001-7617-6 doi:10.1553/ISDR-24

1 Introduction 2
2 Study sites 3
2.1 Deep-seated gravitational slope deformation Gradenbach 4
2.2 Rockslide Steinlehnen 8
3 Seismic monitoring networks 10
3.1 Gradenbach 10
3.2 Steinlehnen 12
3.3 Near real-time data transmission 14
4 Data archive 14
4.1 Gradenbach 14
4.2 Steinlehnen 16
5 Seismic activity of the Gradenbach landslide during the acceleration phase 2009 17
5.1 Earthquakes, anthropogenic- and natural noise 18
5.2 Events induced by processes related to the movement of the slope 20
5.3 Source regions of the slope events 24
5.4 Slope displacement and seismic events 26
6 Seismic activity of the Steinlehnen rockslide during the acceleration phase in June, 2010 28
6.1 Interactive screening and classification 29
6.2 Automatic classification 31
6.3 Localization of the seismic events 32
6.4 The relation of the seismic activity to the displacement of the slope 35
7 Patterns in seismic background noise related to precipitation and groundwater infiltration 38
7.1 Visualization and screening of the ambient seismic noise 38
7.2 Ambient seismic noise events related to precipitation 41
8 Polarization of seismic waves recorded with surface-based stations at the Gradenbach landslide 42
8.1 Polarization of local earthquakes recorded at the seismic network Gradenbach 43
8.2 Polarization of event classes of the acceleration phase 2009 46
9 Relation of displacement rate to hydrological parameters 47
10 Unsupervised classification of seismic events using self-organizing maps 49
11 Near real-time visualization of seismicity at the Gradenbach landslide 51
12 Data processing methods 52
12.1 STA/LTA event detection 52
12.2 Pattern extraction event detection 54
12.3 Event localization using seismic waveform amplitudes 58
12.4 Interactive event screening and classification 59
12.5 Objective classification using fuzzy logic 60
13 Processing software Seismon 63
13.1 Software design 63
13.2 Use of Seismon within other projects 65
References 68

1 Introduction

Deep-seated gravitational slope deformation (DGSD) in rock is a frequently observed phenomenon on high alpine valley flanks. These mass movements may exhibit episodic phases of high creep or sliding velocity and examples are known where the motion changed to a rapid and catastrophic rock slide. Several representative examples of deep creep were investigated by geodetic and geophysical methods within the scope of IDNDR, ISDR, and cooperation with alpS-Centre for Natural Hazard Management, Innsbruck, Austria. Main scientific achievements by these projects are continuous deformation monitoring by GPS at the Gradenbach (GB) mass movement, structural models of GB and other representative examples of deep creep and sliding in rock, integrated interpretation of GPS, photogrammetric and geophysical data, and observation of strain and seismic activity. Furthermore, generation of deep creep in rock slopes was modelled by FE-methods, subcritical crack growth as the controlling mechanism of rock disintegration. The further development after strain concentration at a basal sliding surface was modelled by rotational slider blocks and the application of state and velocity dependent friction laws.

Results from previous ISDR projects showed that there are episodic phases of accelerated movement, starting and stopping without any cause recognized so far. Investigation, understanding, and modelling of these characteristics have been a main task of this project. In order to achieve this goal we continued and intensified the ongoing monitoring at GB by GPS and a seismic network, we tried to reconstruct the deformation history using available measurements and historic documents By the use of the seismic records and data from other high resolution monitoring devices (e.g., strain rosette) we tried to resolve the spatio-temporal microstructure of the deformation. Hydro-meteorological data supplied by the Federal Research Centre of Forests (BFW) have been of great value and built, together with the GPS and seismic data the basis for an in time warning for a significant acceleration of the GB mass movement. By cooperation with alpS GmbH, Innsbruck, seismic monitoring could be extended to a second mass movement, Steinlehnen, Sellrain, Tyrol.

The research goals of the project have been pursued by cooperation with TU Graz. The team of TU Graz has been responsible for the geodetic part of the project. They also realized another major goal: dissemination of basic data on the deformation and seismicity, as well as other monitoring data relevant for hazard estimation (see Final Report of TU Graz, August 2008 - December 2013). The team of TU Wien concentrated on the continuation and extension of the GB seismic monitoring network, the reconstruction of the deformation history since 1962, and the relation between creep velocity and hydro-meteorological data. Detection, localization, and further seismological evaluation were substantially improved by further development of the “SEISMON” software package. The observation of single seismic events, as well as the analysis of seismic tremor caused by the mass movement increased our understanding of the processes behind acceleration and deceleration. Additional information will be available by the (already submitted) dissertation of Stefan Mertl “Characterization of local seismic events on the deep-seated gravitational slope deformation Gradenbach” in few months.

2 Study sites

Two landslides in the Austrian Alps have been selected as study sites for this project. The deep-seated gravitational slope deformation (DGSD) Gradenbach (see figure 2.1) in the Möll valley, Carinthia, and the Steinlehnen rockslide (see figure 2.2) in the Sellrain valley, Tyrol (see figure 2.3). The DGSD Gradenbach (GB) represents the main study site with an emphasis on multidisciplinary, long-term monitoring and the Steinlehnen rockslide (SL) was choosen for a short-term comparative study. The two landslides have been chosen because they represent well explored case studies and re-occurring acceleration phases have been observed in the past[1,2].

Figure 2.1: The Gradenbach deep-seated gravitational slope deformation. (left) aerial photo from the year 2006 and (right) view from the opposite slope from the year 2011.

Figure 1.2: The Steinlehnen rockslide.

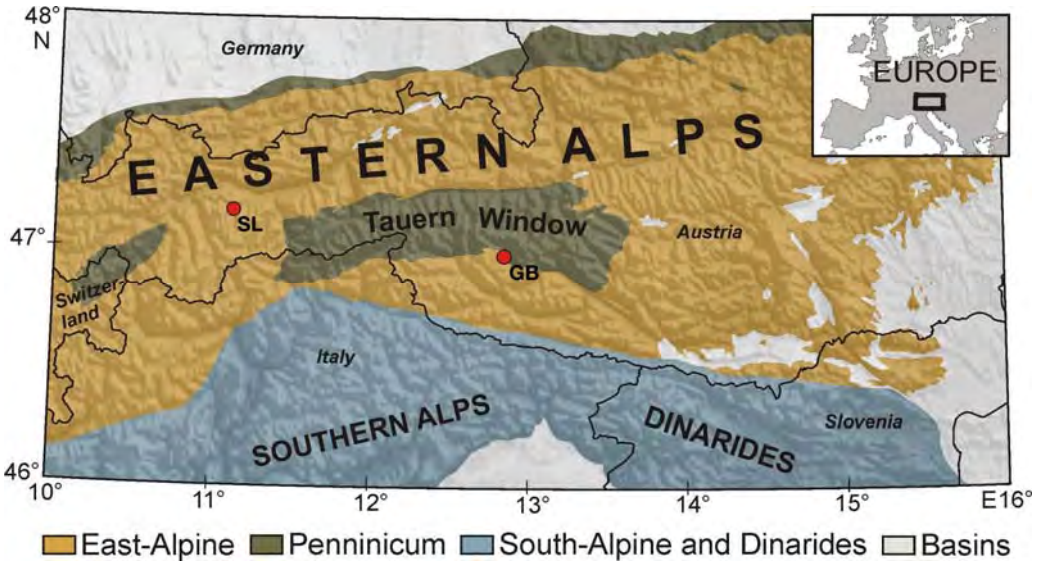

Figure 2,2: Locations of the Gradenbach deep-seated gravitational slope deformation (GB) and the Steinlehnen rockslide (SL).

2.1 Deep-seated gravitational slope deformation Gradenbach

The deep-seated gravitational slope deformation Gradenbach, located in the central Eastern Alps, is part of the Matrei zone, which consists mainly of phyllitic Bündner-schists, carbonates, and Alpine Verrucano (see figure 2.4). The Matrei zone is dipping to the south below the Upper East-Alpine Schober crystalline and overlies the Glockner nappe and the Venediger nappe.

The structure and morphology of the deep-seated gravitational slope deformation Gradenbach is given in figure 2.5. The main scarp with an extent of about 30-40m, the bulging at the zone of accumulation and the oversteepened valley flanks at the toe of the slope can be clearly identified. Several small, surface based landslides and rockfall areas are visible near the main scarp and at the toe of the slope. The boundary of the landslide outlined in figure 2.5 generally follows the description given by Moser and Glumac[3]. It was slightly adapted using up-to-date orthophotos and the displacement rates determined by photogrammetric methods[4]. The depth of GB was determined by refraction seismic measurements[5,6]. From these data and the information from two boreholes[5], a map of the basis of the mass movement was constructed[6]. The basal zone, which may be a discontinuity or a transition zone, defines the base of the moving rock mass. The maximum vertical depth of the basal zone is ~130m and the computed volume of the sagging rock mass is 120 10^6 m^3. The average P-wave velocity of the compact rock beneath the basal zone is ~4740 m/s. From the 1D P-wave velocity model (equation (1)), which was created by Brückl and Brückl[6] by diving wave tomography using the first arrival travel time[6], a 3D P-wave velocity model was created[7].

$$V_p = 455\, D^{0.4} \qquad (1)$$
$$D \ldots depth[m]$$

Because the 1D velocity model in equation (1) is defined for depths D measured vertical from the surface, the computation of the 3D P-wave velocity model was done in a rotated coordinate system. Cross-sections of the 3D velocity model are given in figure 2.6.

Many geodetic, geotechnical, meteorological, hydrological and seismic measurements have been accomplished at GB[2] and many of them are still running. In strong cooperation with the Graz University of Technology (TUG) and the Federal Research Centre of Forests (BFW), the monitoring systems operating at GB were combined to a common observation system named the Gradenbach Observatory[2]. Figure 2.7 provides an overview of the locations of all the relevant measurements and monitoring sites which are currently operating at GB and details about the individual measurements are described by Brückl et al.[2]. The near real-time data of the monitoring stations of the Gradenbach Observatory given in figure 2.7 is available online at http://gbonline.tugraz.at.

Using the long-term geodetic and geotechnical measurements, the deformation history of the deep-seated gravitational slope deformation GB has been reconstructed[2]. The reconstruction of the deformation history as averaged horizontal displacement back to 1962 is shown in figure 2.8. This figure clearly shows the potential of the landslide GB for episodic phases of increased sliding velocities overlying a steady-state velocity (named the base activity). However, these phases diminish in their intensity after the catastrophic events of 1965 and 1966. The last large acceleration phase began in May 2009 and lasted for about 4 months. The total displacement measured with the wire extensometer at the toe of the slope was ~40 cm and the max. velocity was ~ 8 mm/d.

The current base activity of GB is ~10 cm/a. The last acceleration phase in autumn 2012 showed a displacement of ~40 cm at the top of the slope and 20 cm at the toe of the slope (see figure 2.9). More details about the displacement of the slope can be found in the final report of the project “Acceration and Deceleration of Large Landslides: TUG” Final Report, August 2008 - December 2013, ISDR, Austrian Academy of Sciences conducted by the Institute of Engineering Geodesy and Measurement Systems at the Graz University of Technology.

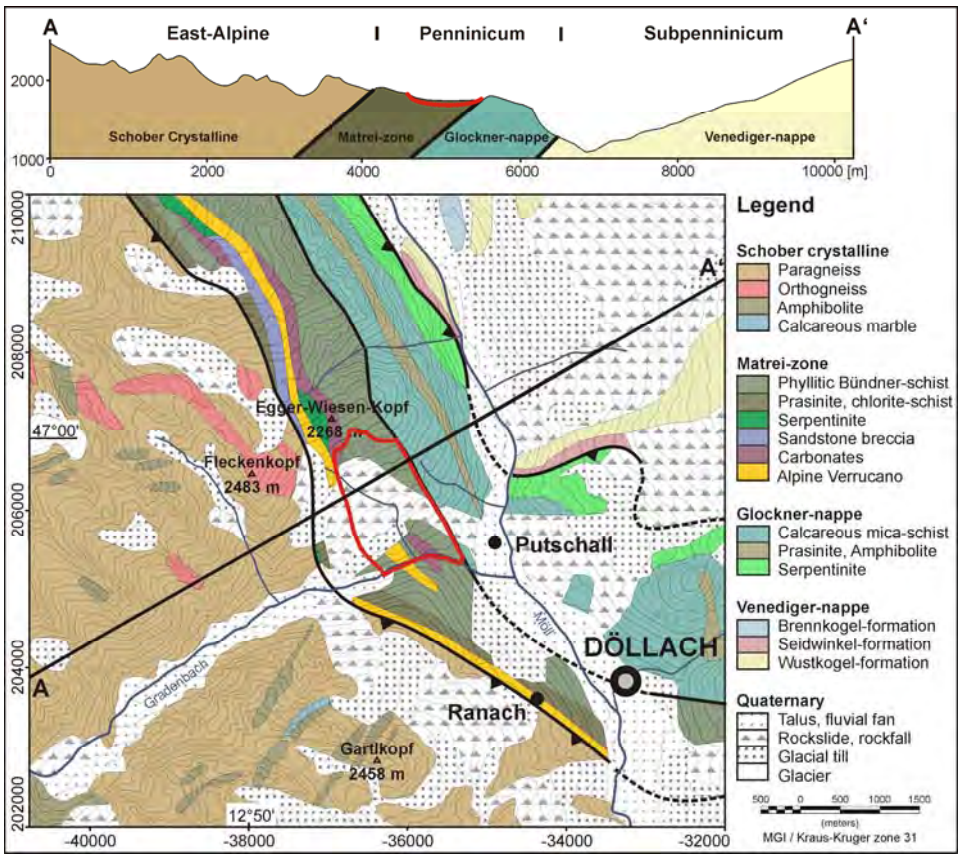

Figure 2.3: Geological map and cross section of the Gradenbach deep-seated.

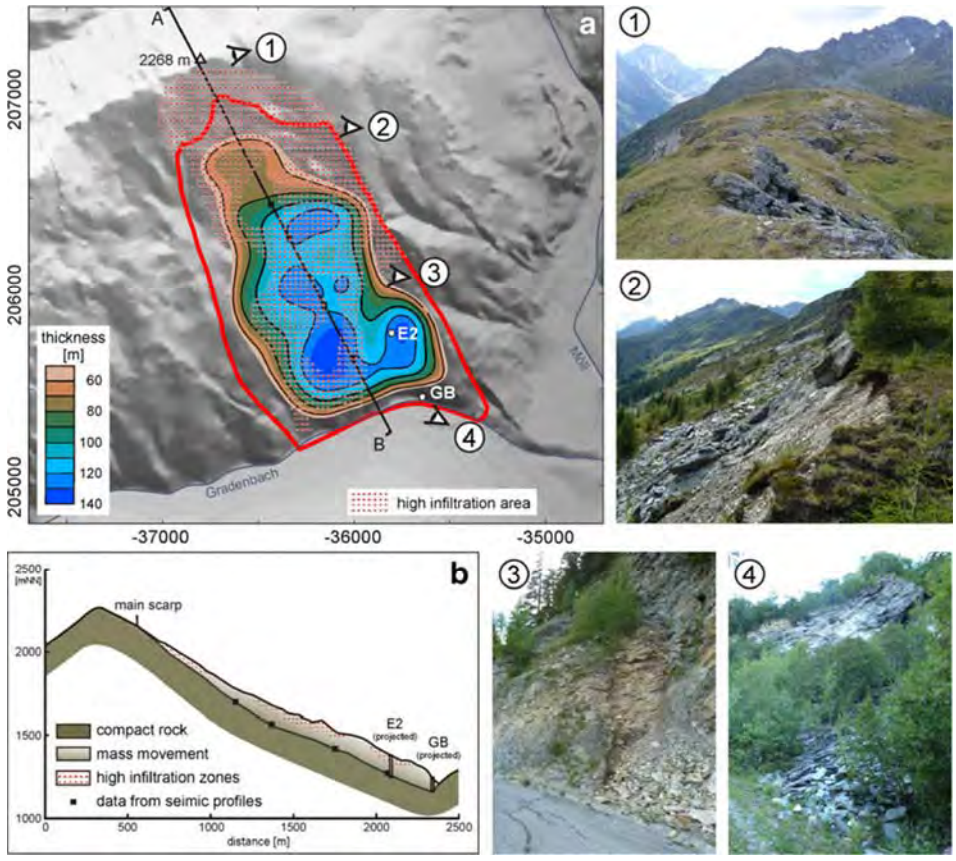

Figure 2.4: Structure and morphology of the Gradenbach deep-seated gravitational.

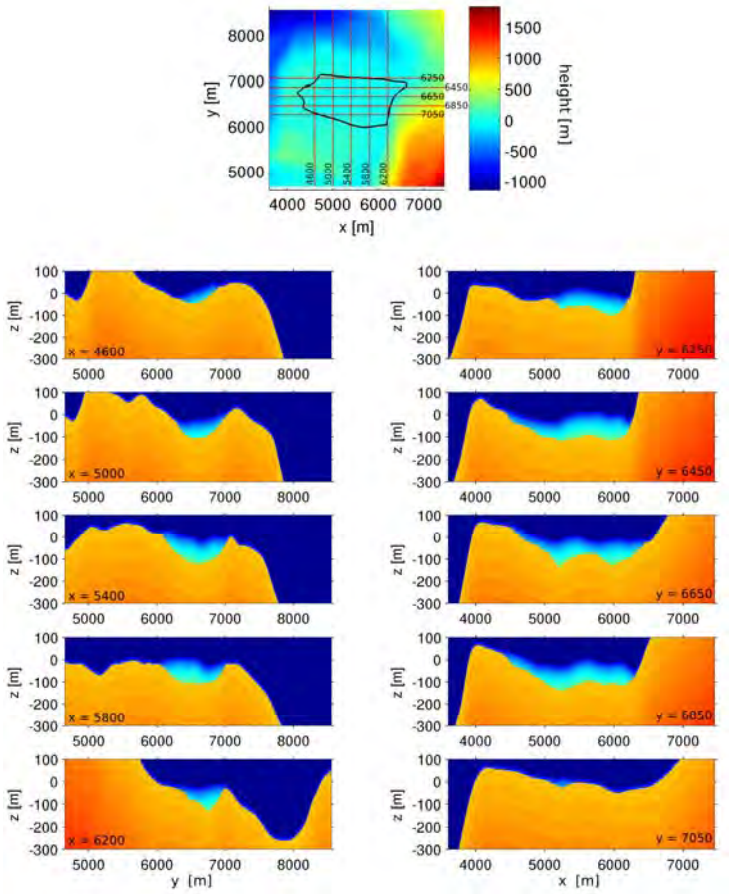

Figure 2.5: Slices along the x- and y axes of the 3D P-wave velocity model. The topmost image shows (black polygon) the boundary of the mass movement and (red lines) the x- and y-slices of the velocity model. The map is in rotated coordinate system.

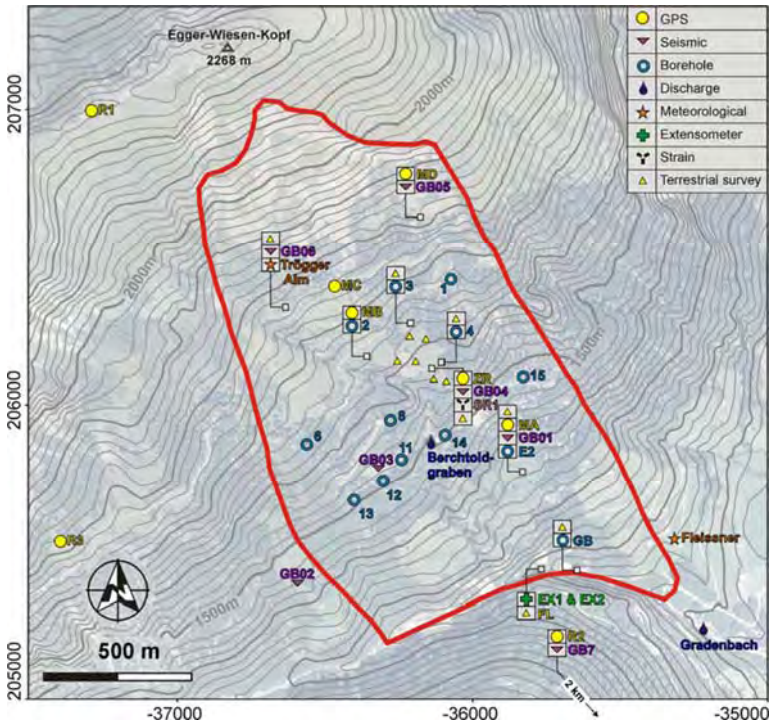

Figure 2.6: The monitoring stations which are currently active at Gradenbach.

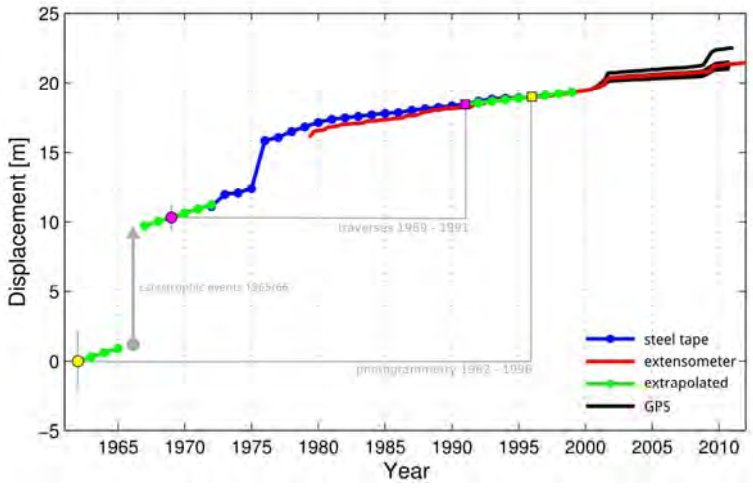

Figure 2.7: Displacement reconstruction of the Gradenbach deep-seated gravitational slope deformation.

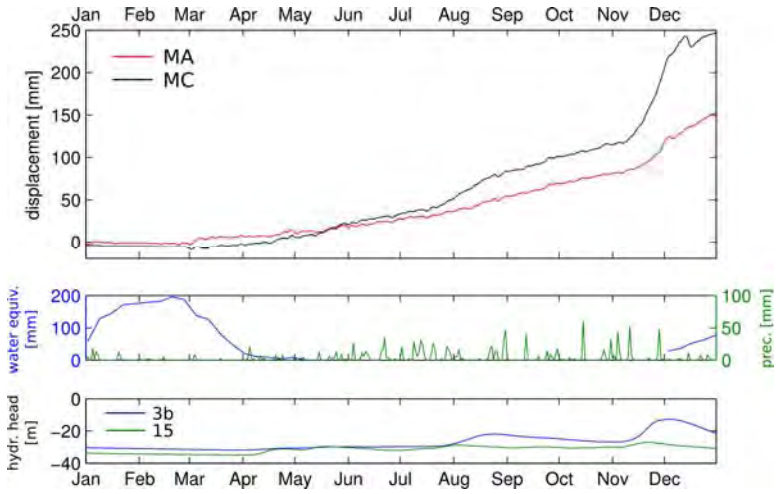

Figure 2.8: The slope displacement of the year 2012 measured by GPS.

2.2 Rockslide Steinlehnen

The unstable mass of the rockslide Steinlehnen consists of paragneisses, amphibolites and granodiorite-gneisses and the lithological contacts dip shallowly into the slope[1]. The whole rockslide comprises several sliding masses bounded by primary scarps and different sliding rates[1]. The total thickness of the main deep-seated rockslide is estimated to about 70 – 100 m. On top of this main rockslide, a highly active slab with a depth of ~10-20 m was identified in June/July 2003, when this slab accelerated and induced a series of rock-fall events. Velocities of up to 4 m/day were measured during the acceleration of the slope. After about 1 month of high slope velocities, the slope started to re-stabilize to a velocity of ~ 1mm/day. The max. displacement of the slope measured during this acceleration phase was ~24 m[8]. In spring 2004, another acceleration phase with a duration of about 4 months occurred with velocities of ~ 4 cm/day[1].

In June 2010, a continuous ground-based synthetic aperture radar (GB-SAR) instrument IBIS-L was installed by the Institute of Geodesy, TU Darmstadt, to

monitor the displacement of the rockslide Steinlehnen. The GB-SAR was operating from June 9 to July 7, 2010 at a location opposite of the rockslide (see figure 3.4). The GB-SAR measurment rate was ~ 1 image every 7 minutes, delivering a continuous displacement data series of the whole slope.
From about June 20 to June 23, the high active slab showed a minor acceleration with a mean total displacement of ~ 7cm and a max. velocity of ~1.8 mm/hour[9]. The aerial displacement derived from the GB-SAR measurement (see figure 2.10) showed, that the area of the maximum displacement was bound to a small region on the north-western boundary of the high active slab. The maximum velocity of the slope happened around June 20 (see figures 2.11 to 2.13) and was accompanied by frequent rock-falls.

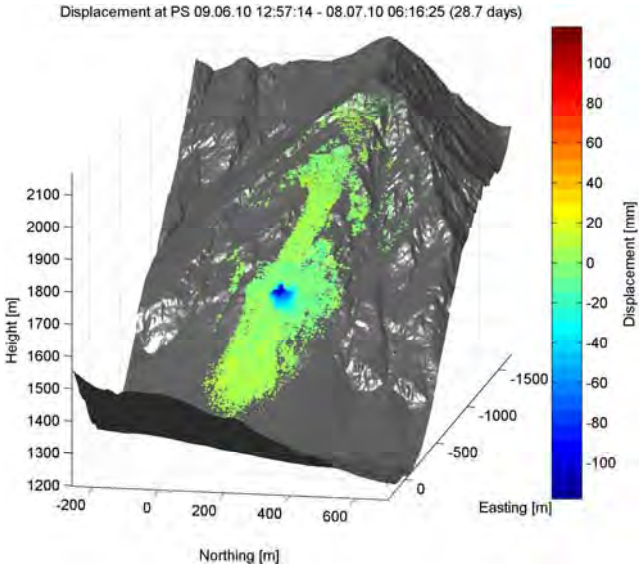

Figure 2.9: Total displacement of the rockslide during the time-span from June 6 to July 7 2010.

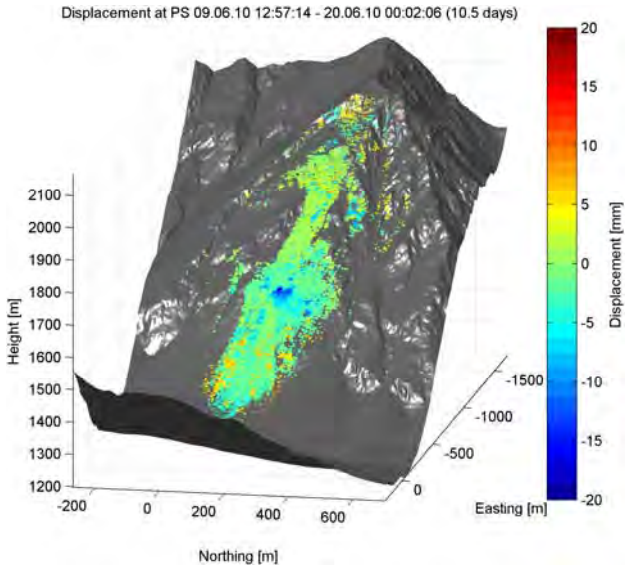

Figure 2.10: Displacement of the rockslide before the acceleration of the slope on June 20, 2010. The displacement shown covers the periof from June 6 to June 20.

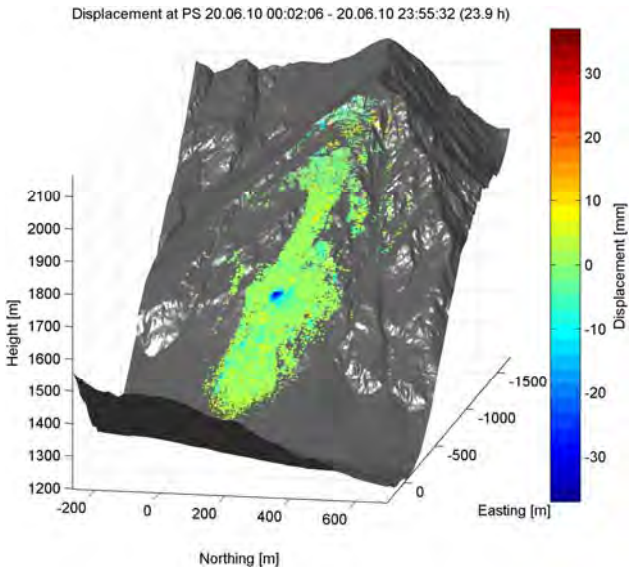

Figure 2.11: Displacement of the rockslide during the most active period on June 20, 2010. The displacement shown covers one day.

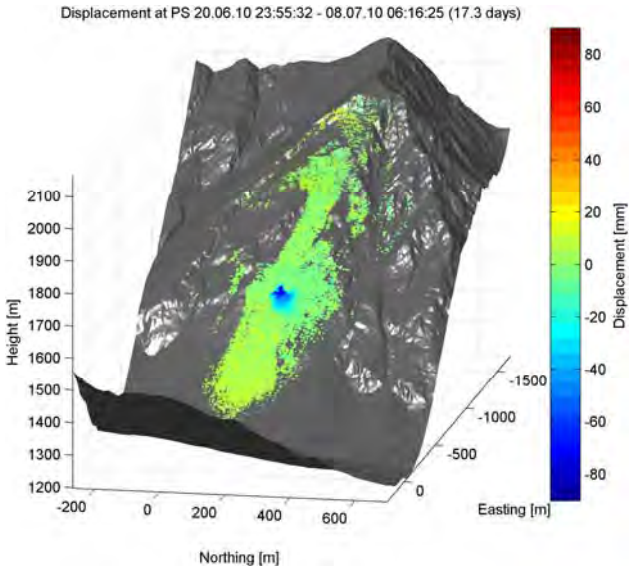

Figure 2.12: Displacement of the rockslide after the most active period. The displacement shown covers the period from June 21 to July 8, 2010.

3 Seismic monitoring networks

3.1 Gradenbach

The seismic monitoring network Gradenbach was installed during the ISDR20 project "Hazard estimation of deep seated mass movements by microseismic monitoring"[10]. At the end of the project duration in September 2008, 6 stations (GB01 - GB06) have been operating. In June 2009, during service-run sr20090811, a seventh station (GB07) was installed (see map in figure 3.1). This station is situated at a stable location at a distance of ~3.5km from the landslide. GB07 acts as a reference station to compare the signals recorded on the unstable

slope with signals recorded at a stable site. To control the stability of the location of station GB07, it has been placed at the GPS reference station REF2 of the geodetic network run by the Graz University of Technology.

Currently, all seven stations of the seismic network are equipped with Reftek 130-01 datalogger, Geospace GS-11D 3-component 4.5Hz geophones, a solar power supplies (70W solar panel and Sunsaver SS-10L-12 solar regulator) and 70Ah lead acid gel batteries. The electronic equipment is stored in a metal box (see figure 3.2) and the geophone is burried at a depth of ~50 cm. The equipment box and the solar panels are placed inside a small plot protected by a fence (see figure 3.3).
Until July 31, 2012, at station GB04 a 1Hz Geospace Seismonitor seismometer was installed. It was replaced to establish a network with uniform seismometers.

On June 11, 2009, a custom-built microphone (type Panasonic WM-64PNT) was installed at station GB04. The microphone was moved to station GB05 on August 11, 2009 were it was installed until autumn 2013. The microphone was removed because it was damaged by weathering and no longer operational.

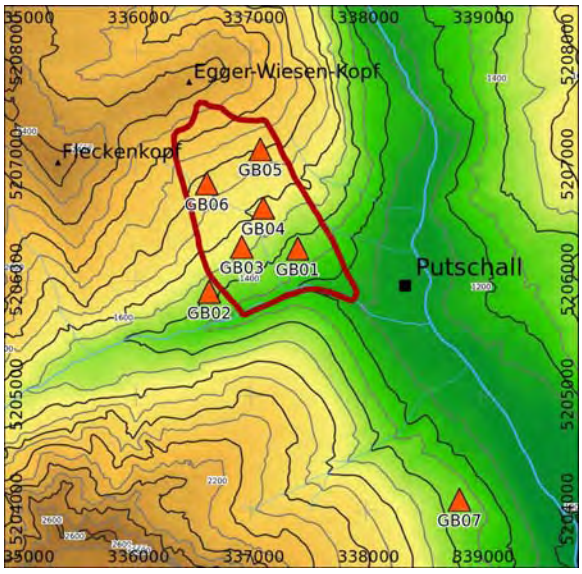

Figure 3.1: The seismic monitoring network Gradenbach. The dark-red polygon marks the boundary of the landslide.

Figure 3.2: The metal box containing the electronic equipment and the 12V battery.

Figure 3.3: Station GB02.

3.2 Steinlehnen

The seismic network Steinlehnen was installed at the Steinlehnen rockslide in autumn 2009 and it was operating until October 2010. The installation was done in cooperation with the alpS GmbH Innsbruck. Four stations (SL01 - SL04) have been deployed in 2009, the fifth station (SL05) was deployed in July 2010. The locations of the stations were chosen with the focus to observe seismic events generated by the displacement of the highly active slab (see figure 3.4). The stations were deployed in autumn 2009, to test, whether the seismic stations can operate during winter and record seismic data during the snow melt in the following spring. All instruments physically withstood the deployment during the winter season, but the data recording showed some gaps due to power supply problems or problems with the recording software (see section 4.2).
The seismic stations were equipped with a SARA SL06C3 3-channel data recorder and a 4.5Hz 3-component GS-11D geophone. The power supply was established with a 30W solar panel and a 12V 42Ah lead battery. The equipment was housed in a plastic box (see figure 3.5) and the geophones were installed in earth vaults at a depth of ~50cm. The recorded data was stored by the data recorder on an internal 8GB memory device.
For the identification of earthquakes, the data of a nearby observatory WTTA of the ZAMG was used. WTTA was located at a distance of ~36km from the Steinlehnen rockslide (see figure 7). The data from this station was requested using the AutoDRM service of the ZAMG.

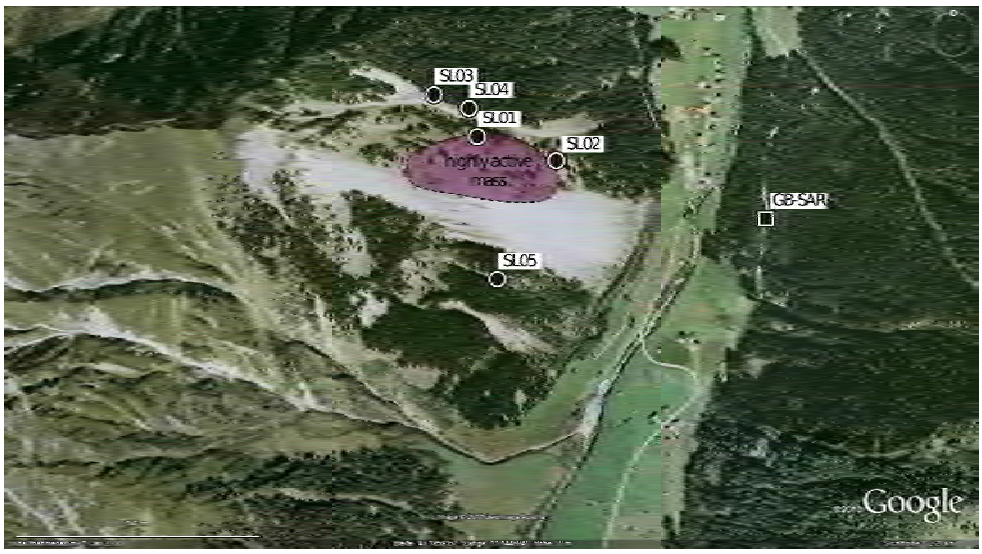

Figure 3.4: The seismic network Steinlehnen. The seismic stations SLO1 to SLO5 (black dots) and the location of the GB-SAR station (black square) is shown. The area of the highly active slab, which was the main target of the seismic monitoring study, is colored in purple.

Figure 3.5: Example of a seismic station deployed at Steinlehnen.

Figure 3.6: Map showing the region around Innsbruck (Tyrol, Austria) with the rockslide Steinlehnen and the observatory station WTTA marked with blue pins.

3.3 Near real-time data transmission

At Gradenbach, the stations of the seismic network are equipped with a HSPA router (Insys Moros HSPA 2.1 Pro) for data communication using the mobile phone network. This enables a better control of the status of the recording units, a better planning of needed maintenance work or data downloading and the availability of near real-time (NRT) data for up-to-date data processing. As the telemetric data transmission is subject to outages due to transmission problems, the seismic data is stored locally at the datalogger on CF-cards as well to guarantee a complete data set. This locally stored data is the primary data for all processing, the NRT data is only used for selected tasks which require the immediate availability of the data (see chapter 11).
The HSPA router establishes a virtual private network (VPN) connection to a server at the Vienna University of Technology. There, the near real-time (NRT) data transmitted by the seismic stations is archived in the Reftek raw – and miniseed data format. The NRT data transmission is in addition to the local storage of the seismic data on CF storage cards.
Software tools developed by Reftek are used for monitoring the state of health of the recorders and to remotely configure the recorder settings. The RTPD software is used for the data transmission and communication between the data server and the recorder units. RTP-Monitor is used for monitoring the state of health of the recorders and the remote configuration is done using RTCC.
The telemetry was installed on September 24, 2009 for all seven stations of the seismic network. After first experiences during the winter time, the HSPA router of station GB04 was disabled because of the frequent outages caused by a too weak solar power supply caused by partly shading of the solar panels. The connection to station GB02, which is located at the toe of the slope inside the Gradenbach valley, is generally weak and therefore, the NRT data is not sent reliable. Although the connection to GB02 is stable enough to get information on the state of health of the data recorder. Currently, 6 stations of the seismic network are transmitting the data sampled with 200 Hz in near real-time to the Vienna University of Technology.

4 Data archive

A large amount of continuous seismic data was recorded during this project. At Gradenbach, 600 GB of Reftek raw data and at Steinlehnen 20.8 GB of miniseed data have been collected. This chapter describes the available data, the methods used to archive the data and the data structure used to store the data for later use.

4.1 Gradenbach

The data of the seismic monitoring network was stored locally in Reftek raw data format at the dataloggers on CF storage card. This data was downloaded during the service runs performed regularly during the year and added to a Reftek raw data archive at a server located at the Vienna University of Technology. The management of the Reftek raw data archive was done using the ArcUtils software. Additionally to the Reftek raw data archive, which contains the waveform data and information about the state of health of the datalogger, a miniseed data archive was created. The miniseed data archive contains the data from the Reftek raw archive converted to the miniseed data format. Hourly miniseed files were created.The miniseed data

was used for any further processing. Figures 4.1 to 4.5 show the content of the miniseed archive for the years 2009 to 2013.

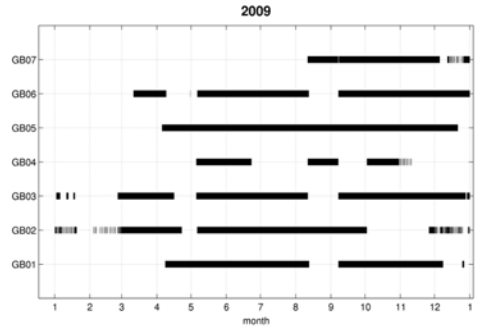

Figure 4.1: Inventory plot of the available seismic data of the year 2009.

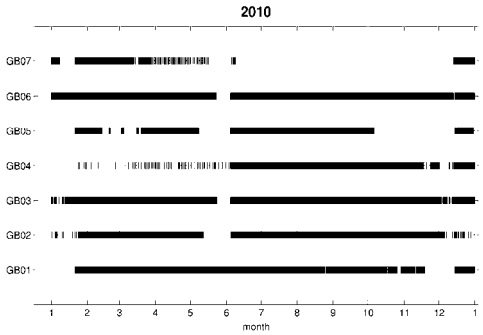

Figure 4.2: Inventory plot of the available seismic data of the year 2010.

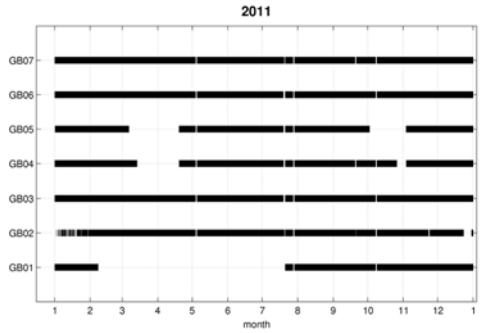

Figure 4.3: Inventory plot of the available seismic data of the year 2011.

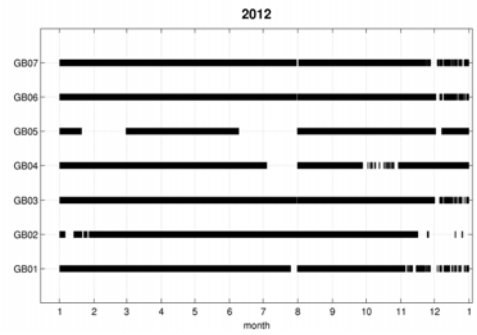

Figure 4.4: Inventory plot of the available seismic data of the year 2012.

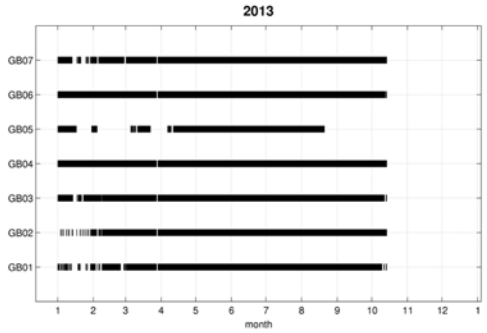

Figure 4.5: Inventory plot of the available seismic data of the year 2013.

4.2 Steinlehnen

The seismic network Steinlehnen was recording data from April 2010 to October 2010. The available data is shown in figure 4.6. Station SL04 didn't resume the operation after the retreat of the snow cover due to a failure of the recording software. At station SL02, which was located at the border to wood land, the shadowing of the solar panel caused irregular operation until June. Station SL05 was installed on July 7. It stopped operation after some weeks due to a failure of the recording software.
The data was sampled with a sampling rate of 100 Hz, on June 7 the sampling rate was increased to 200 Hz. The data was stored in the miniseed file format locally at the dataloggers.

Despite the problems with the recording equipment, a good data set was gathered during the period with the GB-SAR measurements.

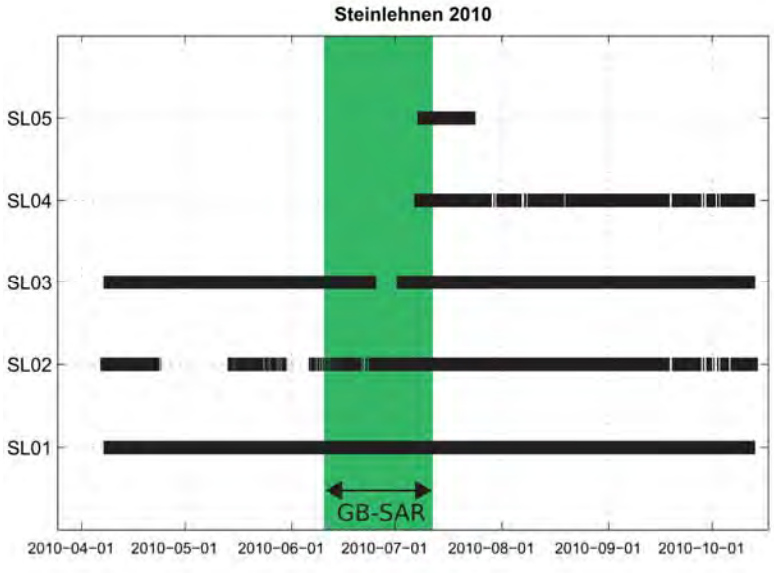

Figure 4.6: Inventory plot of the seismic network Steinlehnen. The green area marks the time period for which the displacement information from GB-SAR monitoring was available.

5 Seismic activity of the Gradenbach landslide during the acceleration phase 2009

The seismic data from March 1, 2009 to October 1, 2009, containing the acceleration phase 2009, has been studied in detail. This work was done within the dissertation of Stefan Mertl "Characterization of local seismic events on the deep-seated gravitational slope deformation Gradenbach"[7] which is currently in review. This chapter depicts the results of the thesis. For detailed information, especially concerning processing algorithms and data material, the reader is referred to the dissertation.

The events were detected using the pattern extraction method (see chapter 12.2) and interactively screened and classified (see chapter 12.4). A first screening of the data resulted in a separation of the events into the three categories: candidate, earthquakes and other events. Figure 5.1. shows the cumulative number of all detected events and the subdivision into candidates, earthquakes and other events. In total, 2005 events were classified. 815 events were identified as earthquakes, 408 as candidates and 782 as other events.

The cumulative sum of all detected events shows a strong increase at the beginning of April. This increase was caused by the L'Aquila earthquake on April 6, 2009, 01:32 UTC and the subsequent aftershocks. Another minor increase around the same time is visible in the candidate- and slope events. This increase doen't coincide exactly with the L'Aquila earthquake and it is mainly caused by the occurrence of a special type of events from April 2 to April 6, 2009 (see chapter 5.2). The increase of other events from the middle of May on is mainly caused by an increased thunderstorm activity in the mountains during summer.

The main categories have been further subdivided into different event types. Following the description given in chapter 12.4 , the candidates have been classified according to their similarity of selected criteria (e.g. spectral content, waveform shape). Furthermore, for each event type it was evaluated, whether the events were induced by the displacement of the slope. Those candidate events with a relation to the displacement of the slope were labeled as *"slope events"*. 159 of the 408 candidates were identified as slope events. Earthquakes were split into local, regional and teleseismic earthquakes and for frequently reoccurring other events, the sources of the events were determined if possible (e.g. thunderstorms, air- or car traffic).

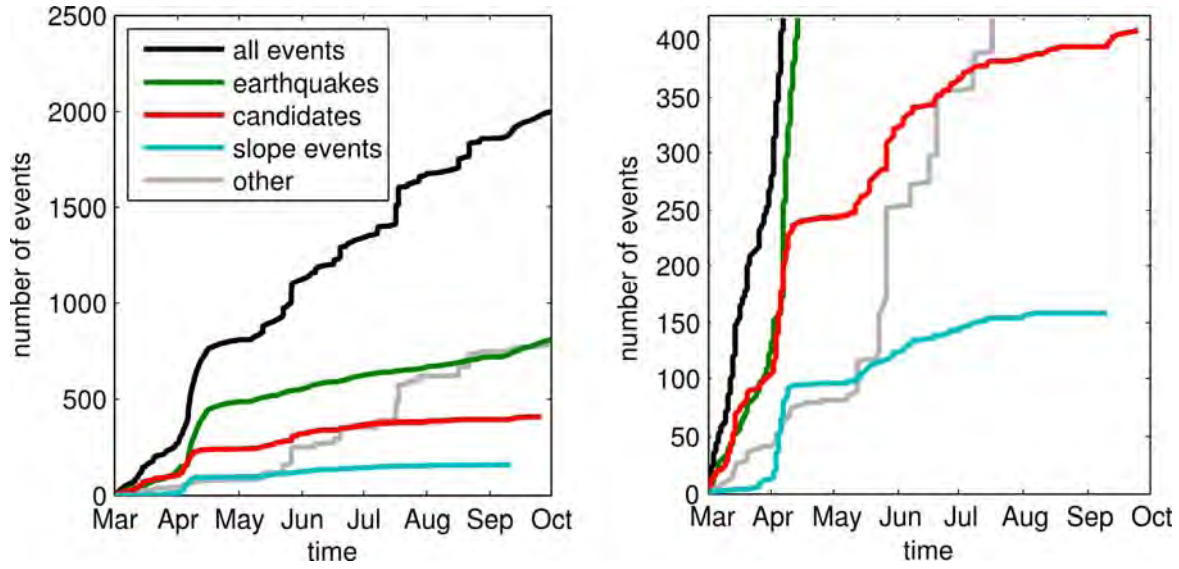

Figure 5.1: The cumulative number of events recorded during the period from March 1, 2009 to October 1, 2009 at Gradenbach. The cumulative number of all events and the identified event classes is shown on the left. To better visualize the detected events related to the slope displacement, the right image shows a zoomed view. The strong increase of earthquakes beginning on 6. April was caused by the l'Aquila earthquake sequence.

5.1 Earthquakes, anthropogenic- and natural noise

The already mentioned co-occurrence of the L'Aquila with the acceleration phase 2009 led to a more detailed investigation of the earthquakes recorded at the Gradenbach monitoring network. During the processed time period 812 earthquakes were recorded at the Gradenbach landslide. 530 of these earthquakes (B-earthquakes) were listed in the earthquake bulletin of the Central Institute of Meteorology and Geodynamics Austria (ZAMG) provided by their AutoDRM service. The remaining 282 earthquakes (NB-earthqaukes) have been identified as earthquakes using the waveform data of nearby observatory stations (ABTA, KBA, MYKA, WTTA). The earthquakes were classified depending on their epidistance d into local (d <= 150 km), regional (150 km < d <= 1668 km) and teleseismic (d > 1668 km)[11]. 105 local, 293 regional and 132 teleseismic B-earthquakes, and 70 local, 204 regional and 0 teleseismic NB-earthquakes were recorded.
A large amount of detected events was assigned to the group "other events". This group mainly contained anthropogenic and natural noise. Some of these noise signals which reoccurred in the seismic records were identified an related to anthropogenic or natural sources: a jet plane passing the seismic network at high altitude (figure 5.2), a helicopter passing the seismic network (figure 5.3), a motorcycle on the mainroad in the valley (figure 5.4) and a thunderstorm (figure 5.5). The comparison of the microphone and the geophone spectrograms show almost identical patterns. Thus it can be concluded, that the signal recorded with the geophone is created by coupling of the acoustic wave with the ground at the station location.

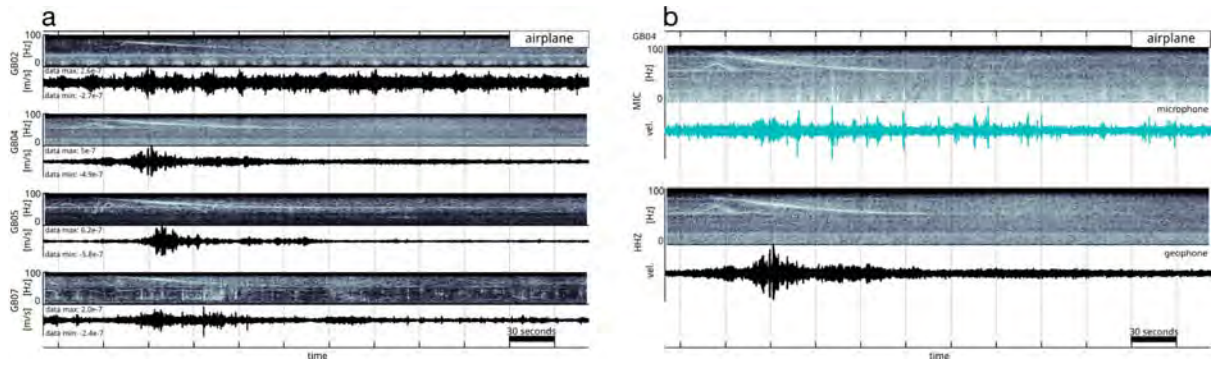

Figure 5.2: Example recording of an jet plane passing the seismic network at high altitude. (a) shows the seismograms and related spectrograms of the vertical component of 4 stations of the seismic network and (b) shows the microphone recording (turquoise) and the geophone recording at station GB04.

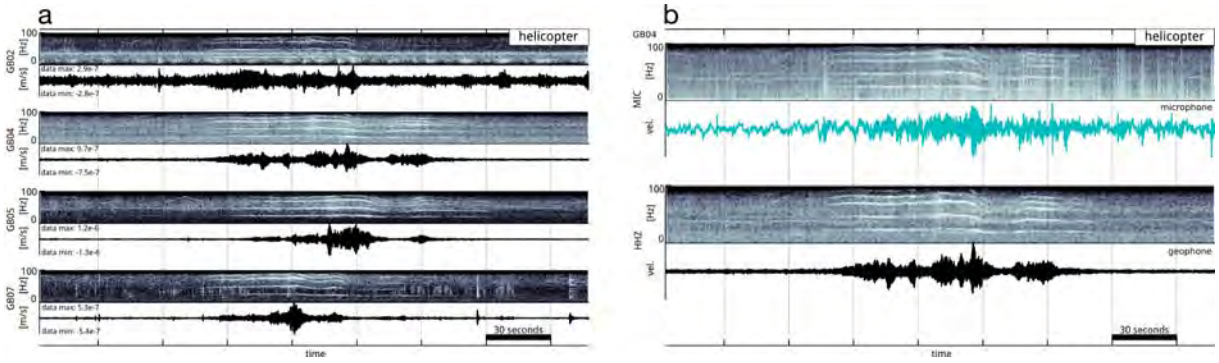

Figure 5.3: Example recording of a helicopter passing the seismic network. (a) shows the seismograms and related spectrograms of the vertical component of 4 stations of the seismic network and (b) shows the microphone recording (turquoise) and the geophone recording at station GB04.

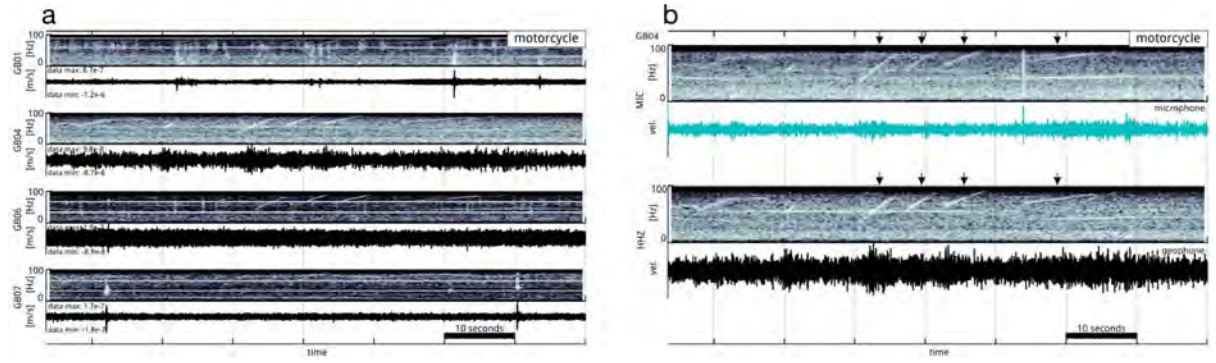

Figure 5.4: Example recording of a motorcycle passing the seismic network a the mainroad in the valley. The changing of the gears is visible in the seismic- and accoustic recordings. (a) shows the seismograms and related spectrograms of the vertical component of 4 stations of the seismic network and (b) shows the microphone recording (turquoise) and the geophone recording at station GB04.

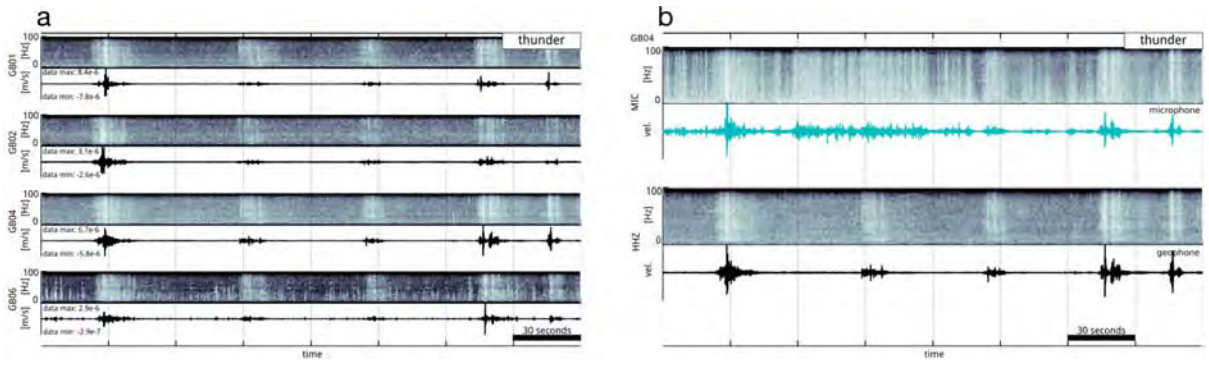

Figure 5.5.: Example recording of a thunder recorded at the seismic network. (a) shows the seismograms and related spectrograms of the vertical component of 4 stations of the seismic network and (b) shows the microphone recording (turquoise) and the geophone recording at station GB04.

5.2 Events induced by processes related to the movement of the slope

During the period of the acceleration phase 2009 (see chapter 2.1), 6 event types (type A, AA, B, D, RF and tremor) of the candidate events were identified as slope events. Representative waveforms and spectrograms of each event type are shown in figure 5.6 highlighting the difference between the event types, both in waveform and spectral content. The cumulative number of events recorded during the acceleration phase is given in figure 5.7 and some characteristics of the slope events are listed in table 5.1. To better characterize the spectral shape of the event types, the mean spectral variation from the general background noise of each event was computed (see figure 5.8).

Type A

Type A events have an abrupt first motion and a median signal duration of 14.1 seconds. The interquartile range (IQR), which is the difference between the upper and lower quartile, is 4.6 seconds. The recordings of the type A events have a SNR with a median of 3.6 and an IQR of 2.7. In general the signal is visible on all stations. The frequency content of the event is between 5 Hz and 40 Hz. The onset of the event is usually more broadband than the trailing. The energy of the event weakens with its duration and sometimes the energy is bound to a frequency band between 10 Hz and 20 Hz.

Type AA

Type AA events are short events with an abrupt first motion and a median signal duration of 3.1 seconds. The IQR is 0.3 seconds. The recordings of the type AA events have a high SNR with a median of 5.2 and an IQR of 1. In general the signal is visible on all stations. The events show a high frequency onset between 3 Hz and 100 Hz. The onset is followed by a low frequent waveform with frequencies between 3 Hz and 30 Hz. Only 4 of these events have been recorded during the acceleration phase 2009. 3 events occurred with 5 days in June.

Type B
Type B events have an emergent onset and a long duration with a median of 24.1 seconds and an IQR of 11.8 seconds. The events have a low SNR (median = 2.4, IQR = 1.1) and are sometimes not visible in an unfiltered seismogram. Mostly, the events are not visible at the station GB02. Most of the energy is present in a low frequency band between 3 Hz and 10 Hz. Some of the events have energy in a second frequency band between 15 Hz and 25 Hz. All of the events show a similar frequency spectrum and a decreasing energy with time (see figure 5.8). The later type B events (beginning with event number 14 in figure 5.8) have a different spectrum than the events happening earlier.

Type D
Type D events are short events with a weak first onset, that is sometimes hidden in the background noise. The median event length is 5.6 seconds (IQR = 5.6 s) and the median SNR is 3.4 (IQR = 3.8). The onset of the events shows frequencies above 10 Hz whereas the later part of the events is dominated by frequencies below 10 Hz. The separation between the high frequent onset and the low frequent ending of the events is clearly visible in the waveform. The low frequent part sometimes shows quite a monotone characteristic. Sometimes two or three successive type D events have been recorded.

Type rf
The type rf events have a long duration (median = 32.1 s, IQR = 38.3 s) and a SNR that varies strongly among the stations. The median SNR is 3.6 with an IQR of 32.3. It was possible to link one of these events to a rockfall happening on June 7, 2009 at 22:15:35 UTC[7]. The waveform of the type rf events generally shows a series of short impulsive events with large amplitudes on one of the topmost stations GB05 and GB06. The amplitudes are attenuated strongly with distance and sometimes the waveform is not visible on the stations deployed at the toe of the slope. The daytime distribution of the events shows, that the type rf events occurred mainly during the nighttime[7].

Type tremor
The type tremor events have the longest duration (median = 50.4 s, IQR = 38.2 s) among the slope event types. The events have a high SNR (median = 4.9) with large variations (IQR = 11.5) among the individual events. The bandwidth of the events generally is quite broad with maximum frequencies of up to 100 Hz. The dominant energy is located in the frequency bands around 10 Hz. The waveform and time-frequency patterns correlate well among the individual stations and the amplitudes show noticeable attenuation over the seismic network. The main occurrence of the type tremor events is bound to a narrow time-span of 5 days from April 2, 2009 to April 6, 2009. 42 of the 49 tremor events occurred during this period.

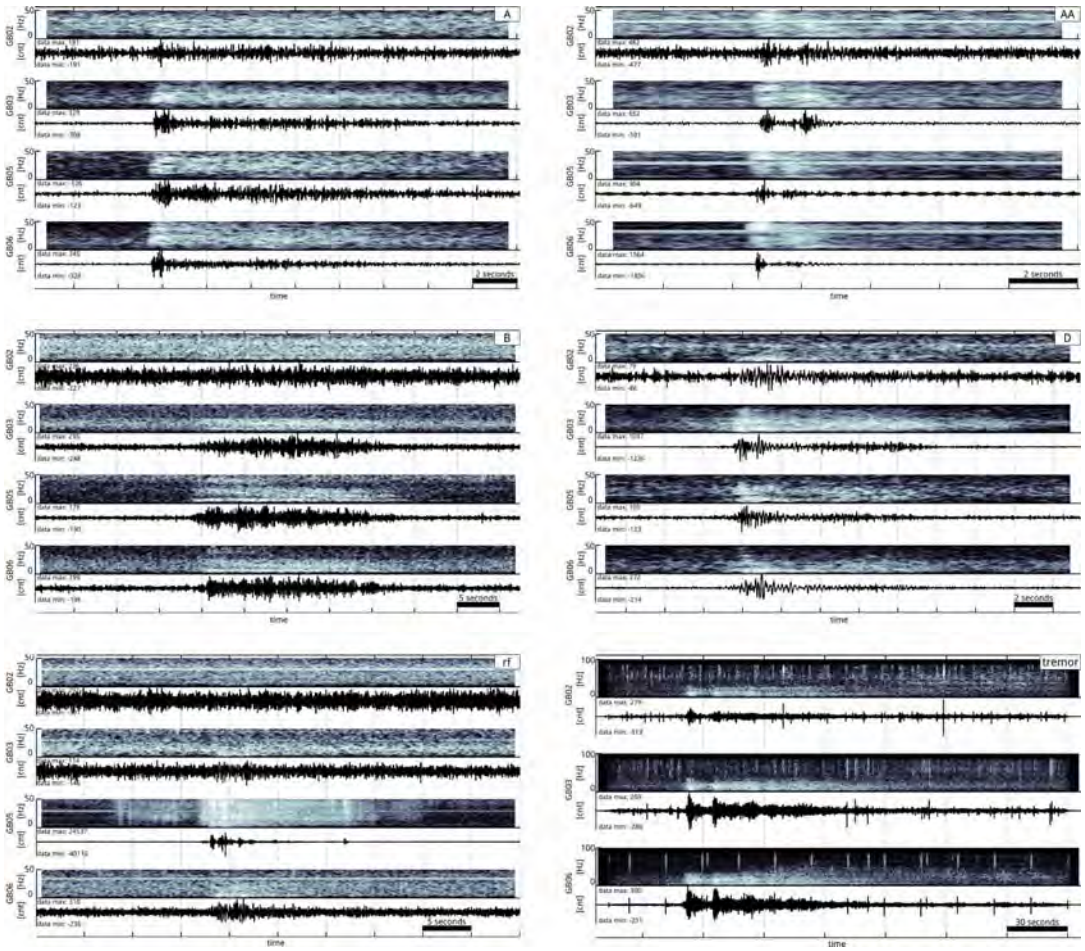

Figure 5.6: Representative waveforms and spectrograms of the slope events.

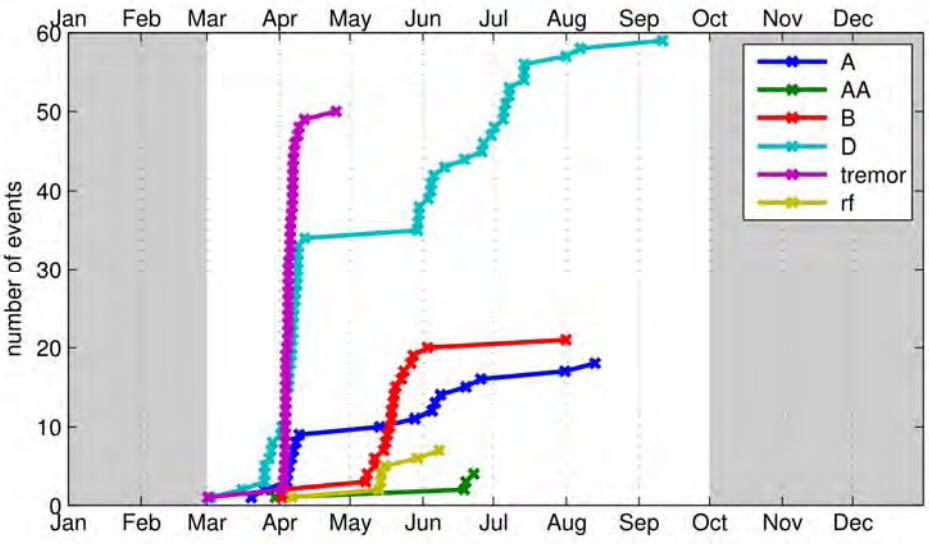

Figure 5.7: The cumulative number of slope events.

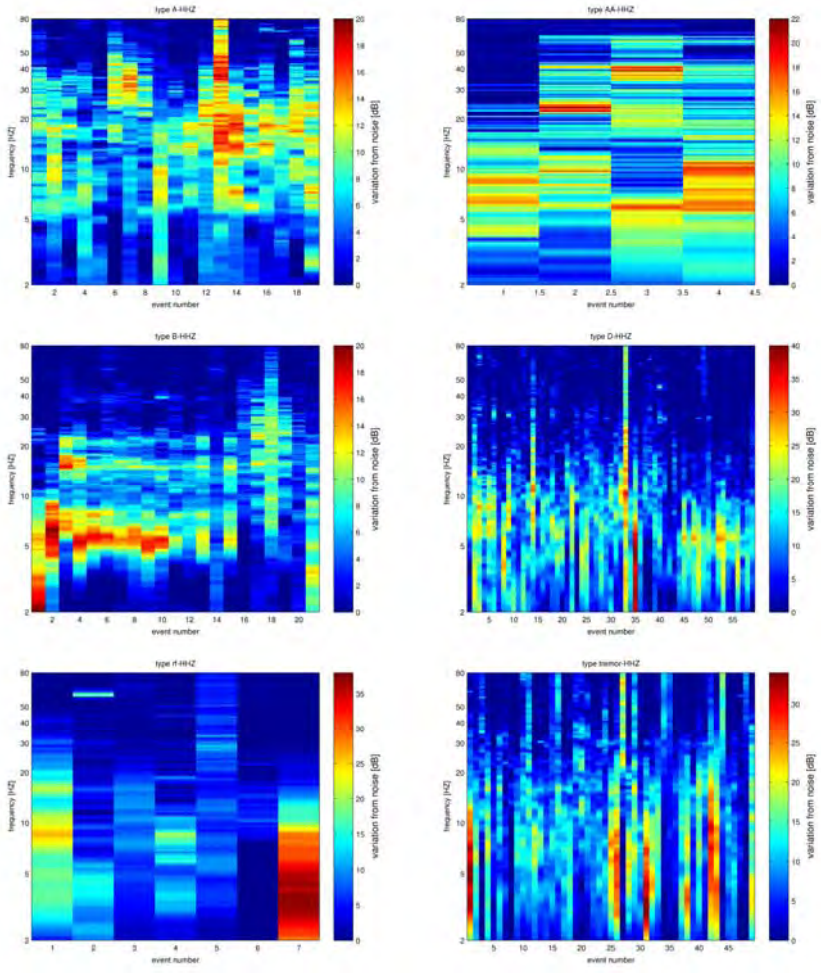

Figure 5.8: The spectral variation from noise of type A events. Each vertical bar represents the variation of the event power spectral density from the noise power spectral density. The noise power spectral density was computed using a 300 seconds long time window before the event. The event numbers are sorted by ascending date.

event type	number of events	Length [s]	length range [s]	Snr	snr range [s]
A	19	14.1	4.6	3.6	2.7
AA	4	3.1	0.3	5.2	1.0
B	21	24.1	11.8	2.4	1.1
D	59	5.6	5.6	3.4	3.8
tremor	49	50.4	38.3	4.9	11.5
rf	7	32.1	31.3	3.6	32.3

Table 5.1: 159 events of the 408 candidate events have been related to the acceleration phase of the slope. They have been classified into six event type groups: A, AA, B, D, tremor and rf. The median values of the eventlength and the signal to noise ration (snr) is given along with the number of events of the individual event types. The range of the event length and the snr is the interquartile range.

5.3 Source regions of the slope events

The localization of seismic events usually requires reliable time picks of the first onset and if possible additional seismic phases. Only for some slope events reliable time picks of the first onset could be determined. For the other events, a macro-seismic approach was used. The localization with NonLinLoc[12,13] of the events with a clear onset is given in figure 5.9, which shows the spatial frequency of possible epicenters, the best fit epicenters given by NLLoc and observed morphological changes caused by the displacement of the slope. 18 events (6 A, 4 AA, 5 D, 3 rf) were localized using NonLinLoc. The scatterplots of the event localizations were used to create a cell-hit matrix of the possible epicenters. The cell-hit matrix was created by counting the number of scatter points within a grid-cell of a regular grid. The cell-hit matrix highlights the zones of the seismic activity taking into account the uncertainty of the localization of each individual event. Figure 5.9 indicates a limitation of the source region of the localized events to the western and upper part of the slope. Morphological changes like scarps or bulging were observed in this area during the acceleration phase as well (see figure 5.10). In the eastern part and at the toe of the slope no similar morphological features were found.
Because only a small number of events were localized using NLLoc, the station-wise distribution of the peak ground velocity (PGV) was used to estimate the source region of the events (see figure 5.11). Before measuring the PGV, the instrument response was removed from the data, an amplitude correction was applied[7] and the data was filtered with a bandbass filter (1-15Hz for type B events, all other events: 1-30Hz).

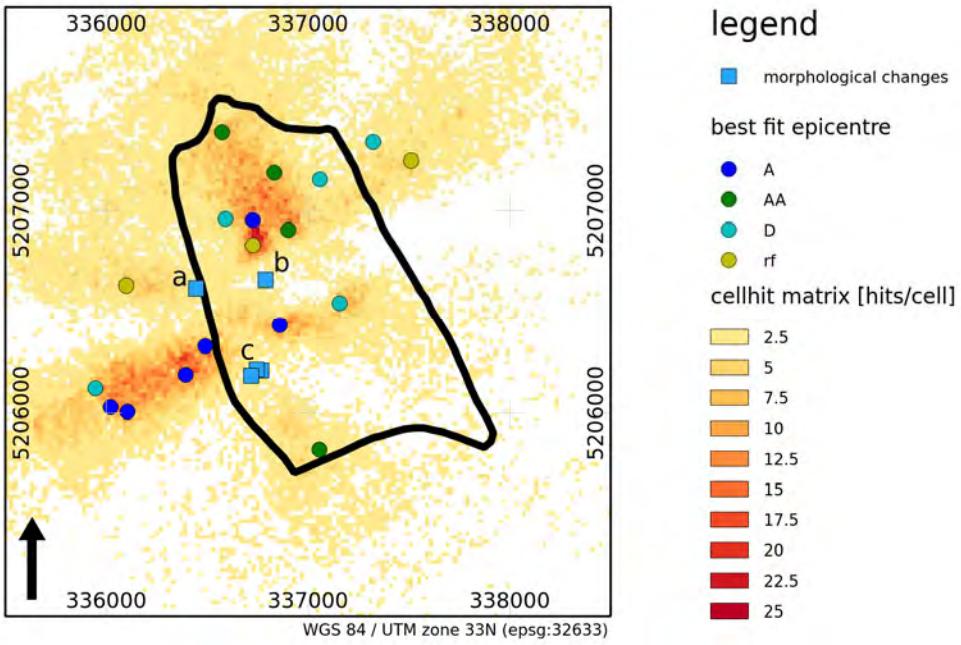

Figure 5.9: Cell-hit matrix of the scatterplots of the NLLoc localizations of 18 slope events. The best-fit epicenters of the events are colored according to the related event type. The labels (a,b,c) of the locations of the observed morphological changes reference the photos in figure 5.10.

The PGV was measured using the envelope of the waveform. For each event the PGV of all three channels at each station was determined. The station-wise PGV value was computed by taking the mean value of the three channels. The PGV was normalized to the absolute maximum of the event. The median of the normalized PGV values per station for all events of a common event type was determined and plotted on a map. This map represents the macroseimically determined source region of the individual event types. If a certain event type is bound to a common source region it is reflected in the distribution of the normalized PGV values. Stations with a high PGV value are located closer to the epicenter than those with low PGV values. Type A events show a quite uniform distribution with an emphasis to the western and upper part of the slope. The source region of type AA events is also located in the western and upper part of the slope. Type B events show increased PGV values at the eastern part of the slope, whereas the highest PGV values of type D events are situated at the western part. Type rf and type tremor events have clear source regions at the top of the slope.

Figure 5.10: Morphological changes observed during the acceleration phase 2009. The photos a, b and c correspond with the labeled markers in figure 5.9.

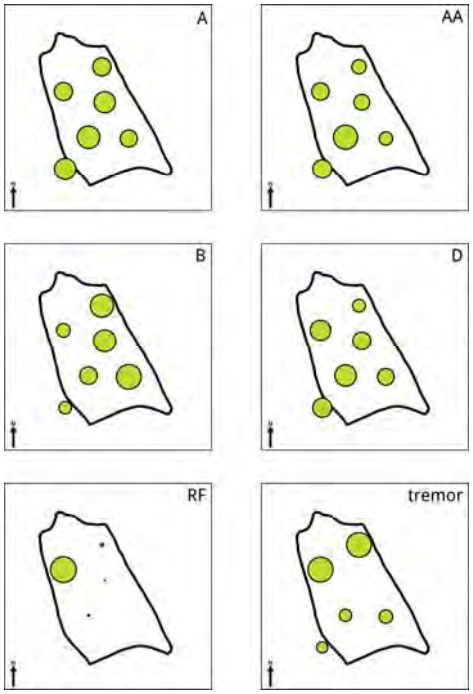

Figure 5.11: Distribution of the mean normalized peak ground velocity (PGV) of the event types.

5.4 Slope displacement and seismic events

In figure 5.12 the seismic events recorded during the period from March 1 to Oct 1 2009 are presented along with geodetic, hydrological, and meteorological data. The temporal distribution of the various seismic event types shows significant patterns and correlation with geodetic and hydrological parameters of the slope.

The seismic activity of the slope starts with the increase of type A, type D and type tremor events at the beginning of April. The type tremor events occur only during a period of 1 week. This isolated occurrence of type tremor events and the accumulation of type A and type D events at the beginning of April coincides with the beginning of the snow-melt which is indicated by a decrease of the snow water-equivalent and an increased discharge of the Berchtoldgraben creek which drains the Gradenbach slope (see figure 5.12). This period of increased seismic activity is followed by a quite period until the beginning of May. Then, the accumulation of slope events coincides with the beginning of the acceleration of the slope measured with the wire-extensometer at the toe of the slope. During the period of the acceleration of the slope up to the beginning of June, mainly type B and type rf events were recorded. With the change of the slope from acceleration to re-stabilization the type B events vanished more or less abruptly and type D events dominated the seismic records from this time on. Type A events were recorded during both, the acceleration and the deceleration phase. The separation of the event types in time as well as the different source regions of the event types (see chapter 5.3) indicates that various processes caused the individual event types.

The type tremor events were bound to the upper part of the slope and occurred during a limited time period coinciding with the snow-melt. Infiltrating water can be regarded as a major triggering factor of the acceleration of the slope[2]. This finding and the fast response of the type tremor events to the beginning of the snow-melt support the assumption, that infiltrating water triggers the type tremor events. Their source region at the top of the slope is an area of high infiltration and possible fissure water ways which would allow a fast infiltration of a large amount of water.

The source region of type B events was in the eastern part of the slope and their occurrence was bound to the period of acceleration of the landslide. Moreover, no type D events were recorded during this period. Proposed by Brückl and Parotidis[14] and Brückl et al.[4], the displacement of the deep-seated gravitational slope deformation Gradenbach can be described with a rotational slider block model. If a block-displacement of the whole slope along the basal sliding zone is assumed, the concentration of the type B epicenters to the eastern part of the slope implies an aseismic slip of the slope in the western part or the release of seismic energy with events below the detection threshold of the network during the acceleration of the slope. Therefore, the accumulation of the type B events in the eastern part would require the creation of stronger events in this area to overcome the detection threshold of the seismograph. This increased event magnitude could be created by irregularities of the topography of the sliding zone (see figure 2.5). The topography of the sliding zone shows a nose- shaped ridge in the eastern part which could have acted as a barrier blocking the downslope movement. Higher shear stress caused by this barrier could have caused the type B events with a magnitude large enough to be detected by the seismic network. The similarity of the spectra of the type B events as well as the polarization analysis further strengthen the assumption of a

common source region and mechanism of these events. Müller et al.[15] draw a similar conclusion concerning the blockade of the slope movement based on GPS measurements.
A possible scenario which could explain the recorded seismic events is given by Stefan Mertl[7]

: *"It is assumed, that for long term observations, the slope behaves according to the slider block model introduced by Brückl and Parotidis[14]. For short-term observations, the landslide doesn't deform as a rigid body in a block-like manner. The main deformation is concentrated to a basal sliding zone. Nevertheless, deformation can occur throughout the entire body of the landslide and it can vary with the location on the slope. The deformation in the basal sliding zone is caused by sub-critical crack growth[2], although other mechanisms might cause the deformation at small depths within the sliding mass. The onset of the deformation of the landslide is located at the top part of the slope. The observations of the recorded seismic events, the geodetic- and the geotechnical measurements can be described with the hypothesis, that the deformation behaviour of the landslide is mainly controlled by a 'wave' of infiltrating groundwater. The infiltrating water of the snow-melt triggers a minor displacement of the upper, shallow part of the slope inducing the type tremor events as well as type D events. The displacement of the upper part of the slope induces additional stress to the middle and lower part of the landslide. The main acceleration of the slope is triggered by a change of the pore-pressure at the basal sliding zone caused by infiltrating water reaching larger depths and the lower part of the slope. Brückl et al.[7] showed the possibility of modeling the acceleration of the slope by infiltrating water raising the pore-pressure at the basal sliding plane. The additional stress caused by the minor displacement of the top region might be a preparatory factor for the initiation of the main acceleration. The deformation of the main acceleration comprises the entire slope and mainly takes part within the sliding zone. This deformation creates seismic events below the detection threshold of the seismic network. Only a barrier at the eastern part of the slope causes an increase of the shear stress and therefore the type B events with magnitudes large enough to be detected by the seismic network are created. When the infiltrating groundwater starts to leave the area of the landslide, the pore-pressure decreases leading to a re-stabilization of the slope. This causes the disappearance of the type B events from the seismic records. "*

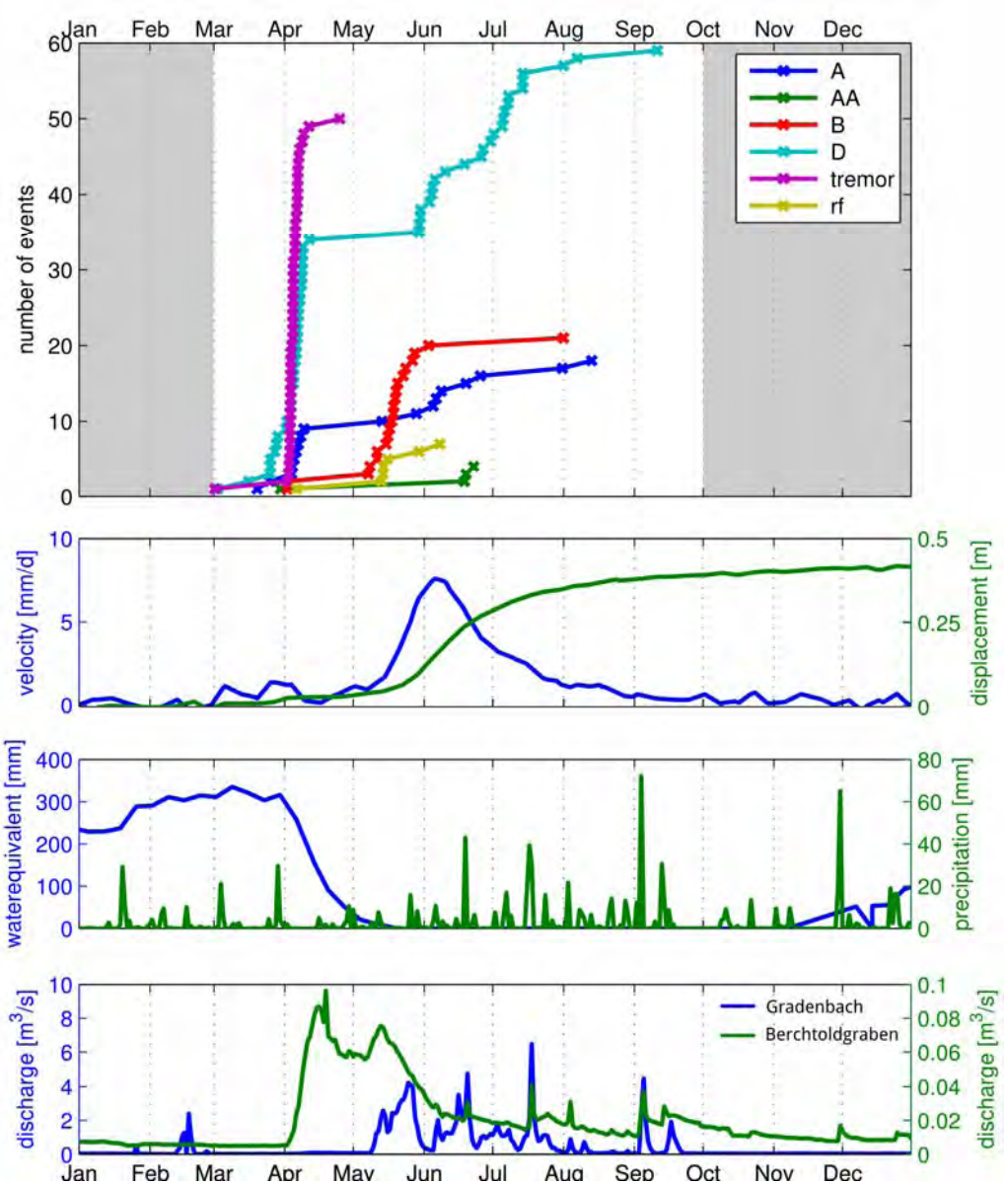

Figure 5.12: The cumulative number of slope events related to the displacement and the hydrological parameters measured on the Gradenbach landslide.

6 Seismic activity of the Steinlehnen rockslide during the acceleration phase in June, 2010

The seismic data from June 6, 2010 to June 28, 2010 was processed within the framework of the master thesis[9] done by Stefan Weginger at the Vienna University of Technology. For this time span an areal measurement of the displacement of the slope accomplished with GB-InSAR was available (see chapter 2.2). The data set of this time period was screened for seismic events originating from the mass movement using the methods described in chapter 12.1 and 12.4 . The events were detected using the adapted STA/LTA detection algorithm described in chapter 12.4 . During the from June 6 to June 28, 2010, 3195 events were detected. From the interactively determined seismic events, the threshold values for the fuzzy classification (see chapter 12.5) were determined using the strongest events. The

objective classification was performed and compared to the results from the interactive classification. To relate the detected seismic events to the displacement of the slope, the epicenters of the events were localized using the amplitude decay localization method (see chapter 12.3).

6.1 Interactive screening and classification

The detected event were interactively screened (see chapter 12.4) and based on e.g. the shape of the waveform, the frequency content and the signal shape in the spectrogram, the events were assigned to event classes. The first step of the classification was the separation of the events into groups of known seismic signals (e.g. earthquakes, anthropogenic and environmental noise, electronic noise) and those events which can't be assigned to any of the known signals. The latter events were named *candidates*. The following groups were used:

- **environmental noise**

Many of the seismic signals recorded by the seismic stations had an anthropogenic source (e.g. car- and air traffic, forest operation) or a source related to meteorological effects (e.g. thunderstorm). These events, especially those with an anthropogenic source were easy to identify in the spectrograms and by the apparent velocity measured over the seismic network which was that of air-speed. In the spectrogram, the environmental noise events usually showed narrow-band shapes with sometimes constant frequencies (see figure 6.1). The signals of by-passing airplanes and helicopters clearly showed the Doppler effect in the spectrogram (see figure 6.1) or harmonic waves. Forest operation and other human activity like construction work, sawmill and similar industry was identified by the limitation of these signals to the general working hours. Sometimes it even was possible to identify the lunch break in the seismic recordings.

- **earthquake**

Global, regional and local earthquakes were identified using the earthquake catalogue of the Central Institute for Meteorology and Geodynamics (ZAMG) and the waveform data of the ZAMG observatory WTTA.

- **false positive**

False positives were those detected signals which were clearly not related to any seismic or environmental source. They mainly consisted of electronic noise (e.g. spike signals) or an increase of the general ambient seismic noise.

- **candidate**

All events which couldn't be assigned to any of the above groups were labeled as candidates. This event group contains all events which have a source which maybe is related to the displacement of the rockslide. The candidate events have been further classified. Events with similar properties have been assigned to alpabetically numbered classes.
From the 3195 detected events, 2485 events were assigned to the candidates group, 611 as environmental noise, 75 as earthquakes and 24 as false positives. For the further classification of the candidate events, only strong events were used.

As a selection criteria of the strong events, the following relation was used:

$$A^2 l > S \tag{2}$$

where A is the mean amplitude, l the event length and S the selection criteria.
After the screening of all selected candidate events, 6 classes were identified: a, h, i, ln, n and rf. Table 6.1 summarizes the characteristics of the individual event classes and figure 6.2 gives example events for each candidate class. The rf events were additionally verified with the GB-SAR images, on which the trails of the rockfalls were visible. This allowed a secure identification of rockfalls and the correlation of the seismic waveform to the rockfall event (see figure 6.3).

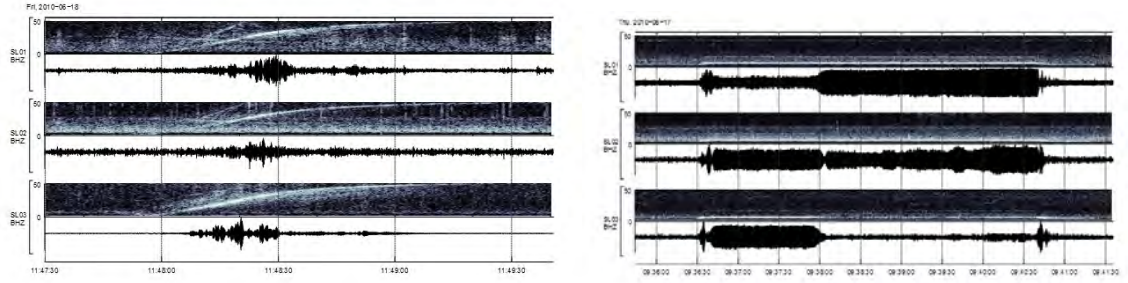

Figure 6.1: Examples of environmental noise signals.

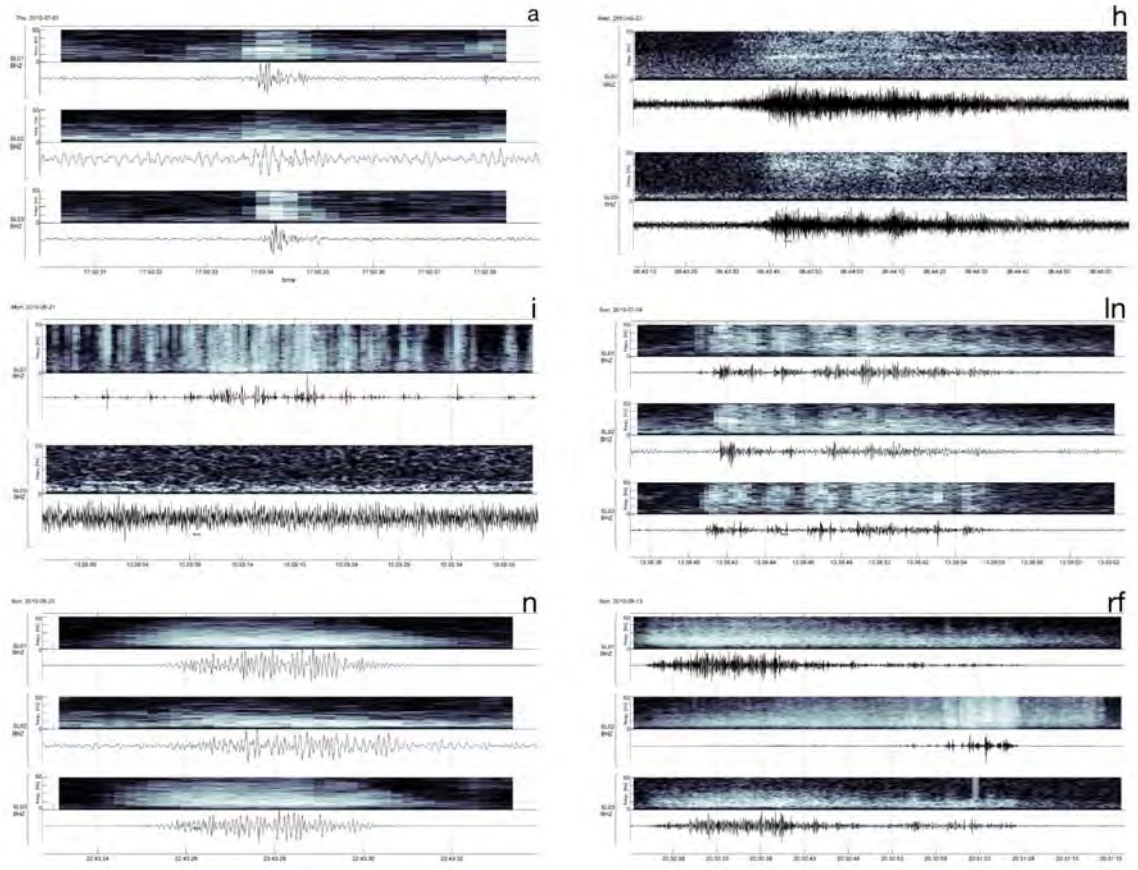

Figure 6.2: Example events of the candidate event classes.

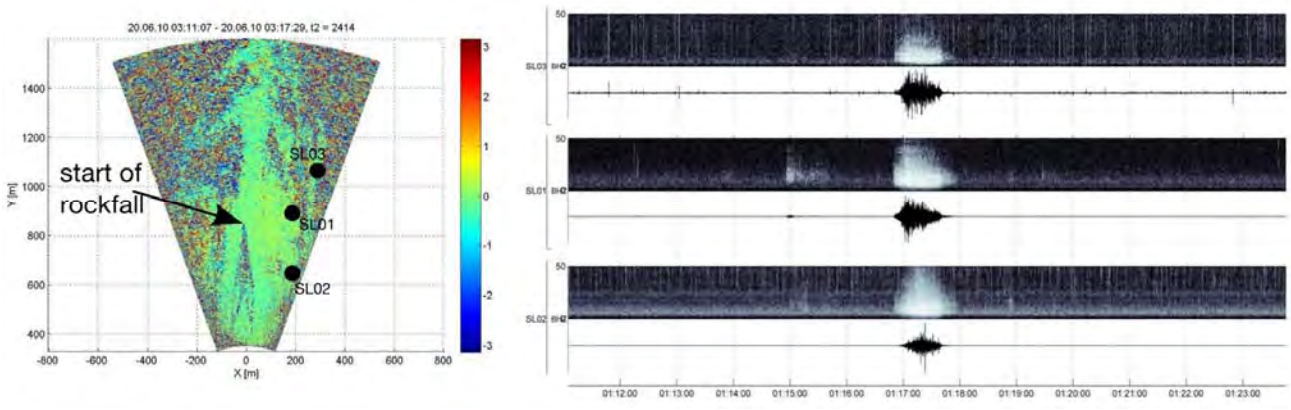

Figure 6.3: Example of a rockfall event (class rf) identified in the GB-SAR image.

Klasse	Länge	Beschreibung
a	~1s	Short events with a broadband frequency spectrum and energy content in the high frequency bands.
h	~ 20s – 60s	Events with a low signal-to-noise ratio. The show a broadband frequency spectrum with the energy maximum in the high frequency bands. The amplitude envelope doesn't show a significant maximum during the length of the event.
i	variable	A time period during which randomly distributed spike-like signals occured.
ln	~ 10s – 60s	Long events with several maxima of the envelope. The signature is similar to rf events, but no offset in time of the envelope is present.
n	~ 5s – 20s	Events with a waveform dominated by low-frequent content. The events show a gradually rising onset and end of the event.
rf	~ 10s – 60s	Rockfall events. Usually a signal with a good signal-to-noise ratio. The onset of the event shows a gradually rising amplitude and during the length of the event, several local maximima of the amplitude envelope are present. The absolute maxima of the envelope is offset in time at recordings of the individual stations of the seismic network. Many of the rockfall events were also identified on GB-SAR images.

Table 6.1: Characterization of the event classes.

6.2 Automatic classification

250 of the strongest classified candidate events from the interactive classification were used to extract the parameter thresholds for the fuzzy classification (see chapter 12.5). The events classified using the interactive classification were re-processed using the fuzzy classification. The comparison of the results from the interactive and the fuzzy classification are given in figure 16.4. The interactive and the fuzzy classification show a good correlation. All further processing was done using the events classified with the fuzzy classification.

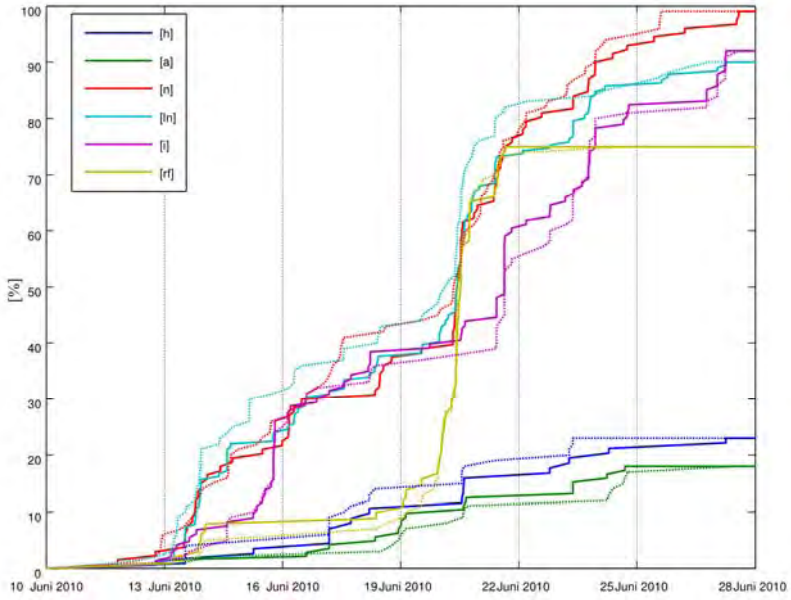

Figure 6.4: Cumulative sum of the events classified by the interactive method (dashed lines) and the fuzzy classification (solid lines). The data of the event classes are normalized to the maximum of the event classes and to the absolute maximum of all event classes.

6.3 Localization of the seismic events

The localization method using the amplitude decay described in chapter 5.3 was used to localize the epicenters of the candidate events of the Steinlehnen rockslide. Usually, the amplitudes of seismic waveforms measured by geophones are heavily influenced by the near-surface structure of the earth beneath the seismic stations and the coupling of the geophone to the soil. This site-specific amplification or attenuation of the seismic amplitudes has to be corrected before using the amplitude decay localization method. To determine the coupling factors of the seismic stations, the recordings of teleseismic- and regional earthquakes were used. Because the station spacing of the seismic network Steinlehnen is small compared to the epidistances of the analyzed earthquakes, it can be assumed, that the recorded amplitudes should be the same for all stations of the network.
To compute the station correction factors, for all teleseismic- and regional earthquakes the maximum amplitudes were measured and the mean of these maximum values was determined for each stations. The variation among the stations of the average values was a measure for the coupling factors. The average values were normalized to the maximum and the coupling factors were computed using the inverse of the normalized average maximum amplitudes. All measured amplitudes used for the event localization have been corrected using the correction factors given in table 6.2.
For the amplitude decay d used in equation (3) the value of 1.6 was used. This value, which includes all damping effects (e.g. geometric spreading, intrinsic attenuation, reflection and refraction), based on experiences from seismic experiments at sites with comparable geology and morphological settings. The operational reliability of the localization algorithm was verified using rockfall events with epicenters determined by the GB-SAR monitoring. Figure 6.5 gives an example

of a localization of a rockfall event which was also visible on a GB-SAR image. This example shows how the localization using amplitudes measured at different times of the rockfall event can be used to track the trace of the falling rock.
Figure 6.6 shows the localizations of single events of the individual candidate classes. Only events with a good signal-to-noise (SNR) ration and recordings on all 3 stations were used for the single event localization. To integrate the amplitude recordings of weak events with a small SNR or with recordings on 2 stations only, the mean station amplitude of each event class was computed and used for the localization. This resulted in a mean epicenter of the individual event classes (see figure 6.7. These mean class-epicenters were used for the assignment of the event classes to the processes involved in the acceleration of the rockslide. From figure 6.7 it can be concluded, that the candidate event classes i, ln, n and rf had an epicenter inside the boundaries of the rockslide. Therefore, it was assumed, that their seismic source was related to the displacement of the slope. Additionally, the rf events were clearly identified as rockfall events using the GB-SAR images, all the other event classes didn't show any signature on the GB-SAR images. This lead to the conclusion, that the events of class i, ln and n were related to sub-surface sources. The candidate events of class a and h showed epicenters outside the rockslide boundary and were therefore not considered as events originating from the rockslide.

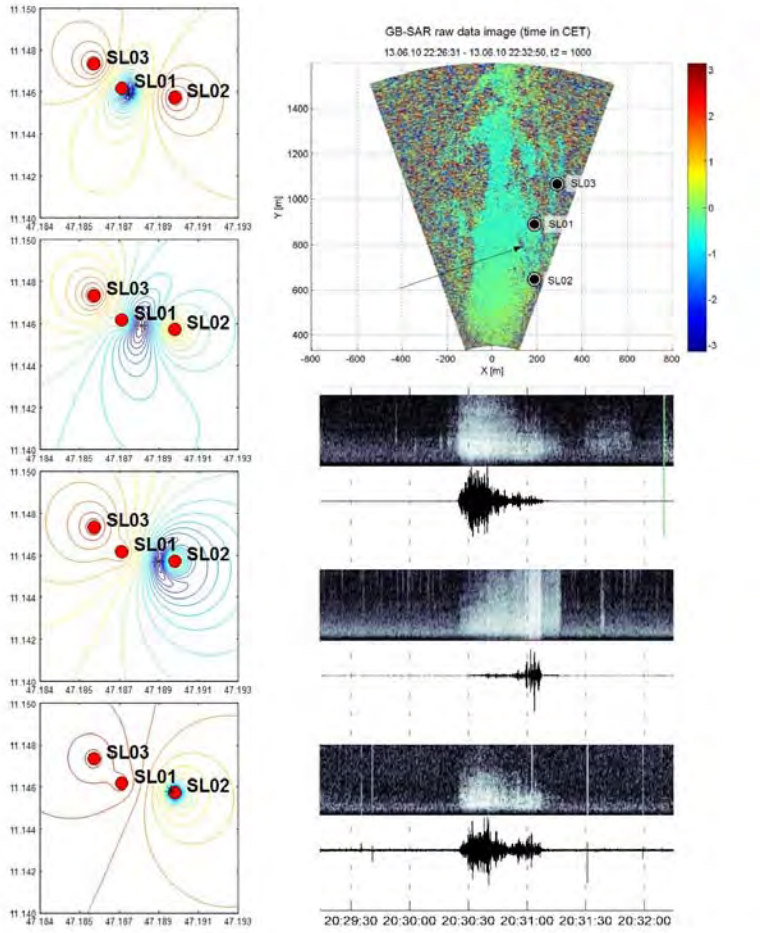

Figure 6.5: Example of the localization of a rockfall event and the verification of the results with the GB-SAR image.

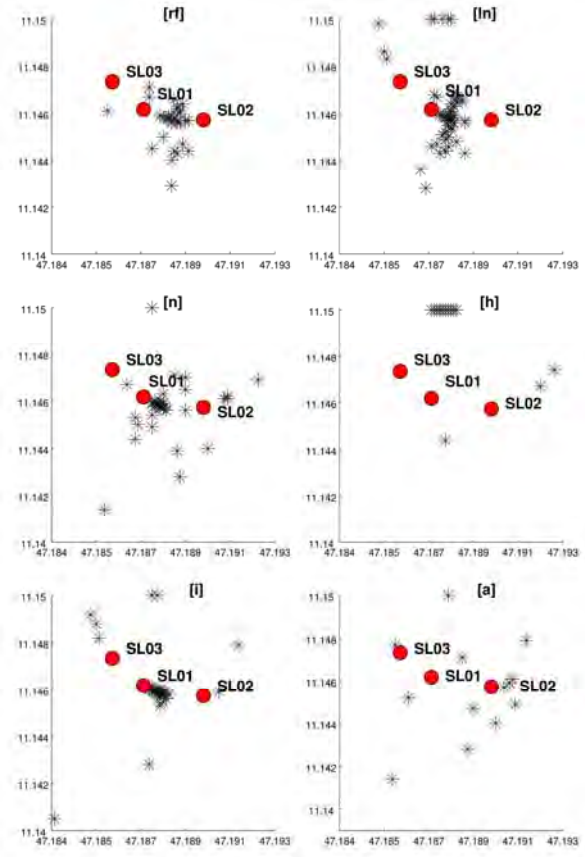

Figure 6.6: Epicenters (black stars) of the events with amplitude recordings on 3 stations and a good SNR.

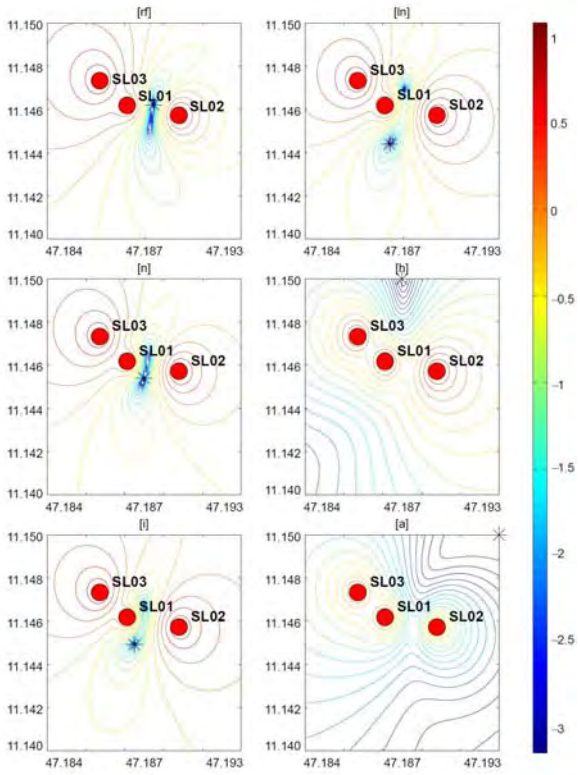

Figure 6.7: Mean epicenter of the event classes.

	Station		
	SLO1	**SLO2**	**SLO3**
mean normalized max. amplitude	0.6	1	0.4
correction factor	1.7	1	2.5

Table 6.2: The computed amplitude correction factors of the seismic stations SLO1, SLO2 and SLO3 of the seismic network Steinlehnen.

6.4 The relation of the seismic activity to the displacement of the slope

The cumulative sum of the events which were related to the displacement of the slope (class i, ln, n and rf) together with the displacement and velocity of the rockslide computed from the GB-SAR monitoring in given in figure 6.8. From this figure, it can be seen, that the increase of the occurrence of seismic events (especially class i, ln and n) starts around June 13. This increase is accompanied by a slight increase of the displacement rate. The main acceleration of the investigated slab (see figure 6.2) started around June 20. With this acceleration of the slope also the occurrence of seismic events increased. Especially the rockfall events (class rf) showed a major increase during the period of acceleration of the slope. The cumulative sum of class rf events in figure 6.8 shows, that the rockfall activity ceased after the slab started to re-stabilize around June 21. The occurrence of events associated to the other event classes (class i, ln and n) continued during the time period of re-stabilization, but the frequency of recorded events decreased with time.
To estimate the energy of the events, the class localization described in chapter 6.3 were used to reduce the event amplitudes to a common epidistance. The event data was reduced to an epidistance of 100m from the epicenter determined for the according event class by

$$x_{100} = x \frac{\Delta^d}{100^d} \tag{3}$$

where x_{100} is the corrected amplitude at an epidistance of 100m, x the amplitudes of the event, Δ the epidistance to the class location and d the amplitude decay (d=1.6 was used for this study). The event energy E_j at station j was computed by the arithmetic mean of the squared data samples weighted by the event length:

$$E_j = l \frac{1}{N} \sum_{i=1}^{N} x_{100,i}^2 \tag{4}$$

where l is the event length and N the number of amplitude samples. The energy of an event was the arithmetic mean of the energy computed for the individual stations:

$$E = \frac{1}{K}\sum_{j=1}^{K} E_j \qquad (5)$$

where K is the number of stations for which an energy value was computed.

The cumulative sum of the energy of the class i, In and n events together with the displacement and velocity of the slab is given in figure 6.9. From this figure, it can be seen, that the major energy of the class i events is released between June 13 and June 16 at the beginning of the slight acceleration. The main acceleration starting on June 20 is not reflected in the cumulative sum of class n events. For class In and n events, the most prominent increase in the cumulative energy coincides with the main acceleration of the slope. Whereat it has to be noted, that the large step in the cumulative energy of class n events is caused by a strong single event on June 20 at 22:43 (see figure 6.10). The localization of this event shows, that the epicenter is located close to the top scarp of the slab.

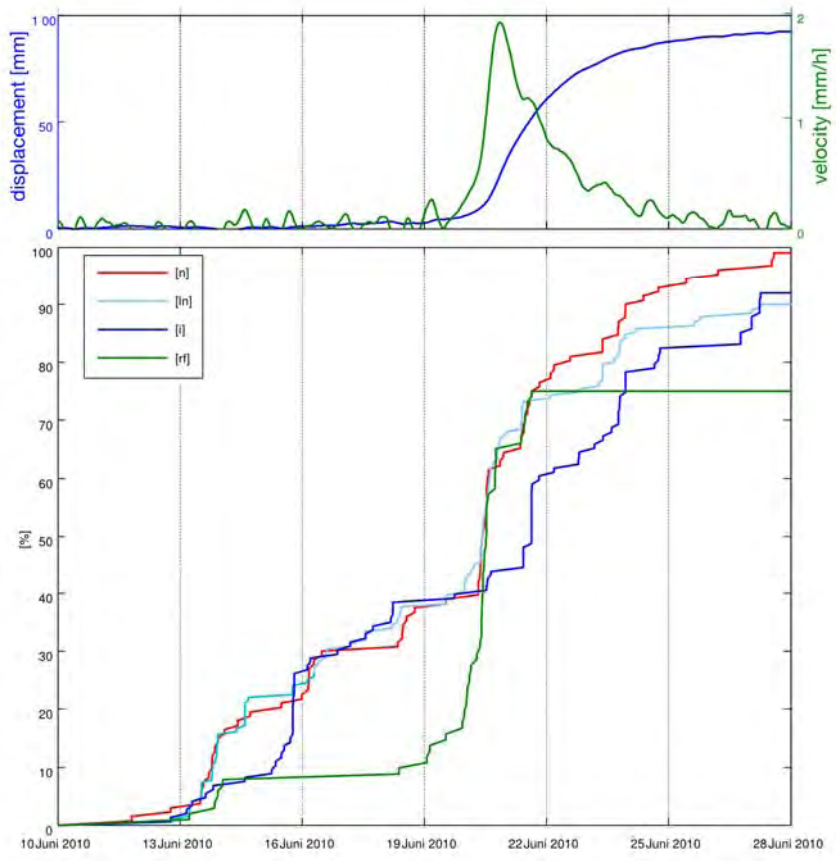

Figure 6.8: (bottom) Cumulative sum of the event classes i, In, n and rf together with (top) the displacement and velocity of the rockslide measured by GB-SAR.

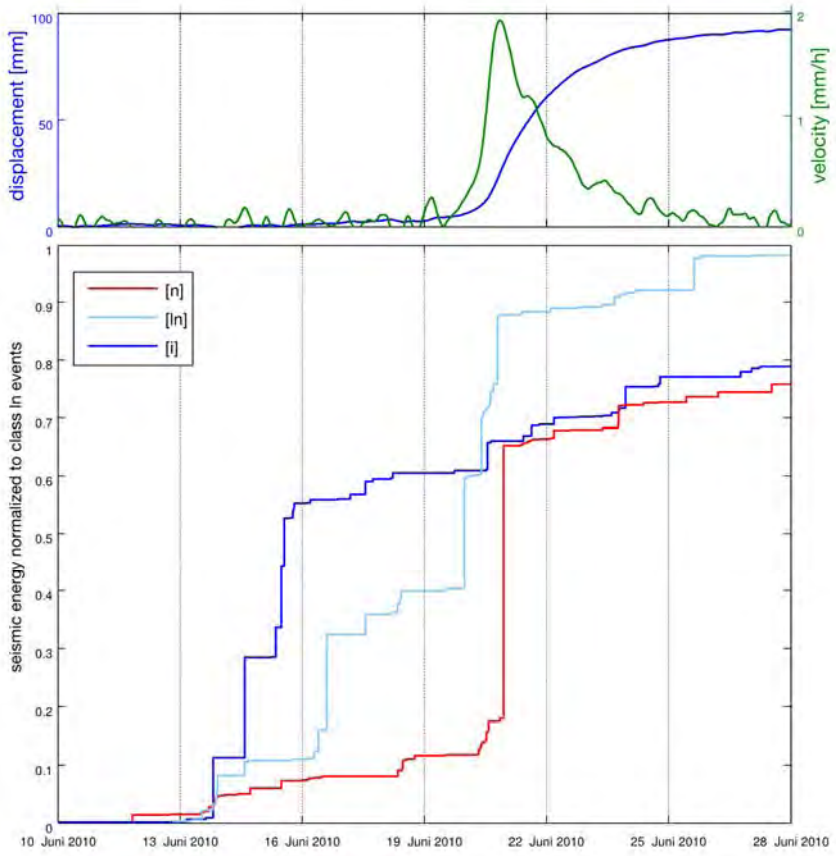

Figure 13: (bottom) Cumulative sum of the energy of the event classes i, ln and n together with (top) the displacement and velocity of the rockslide measured by GB-SAR.

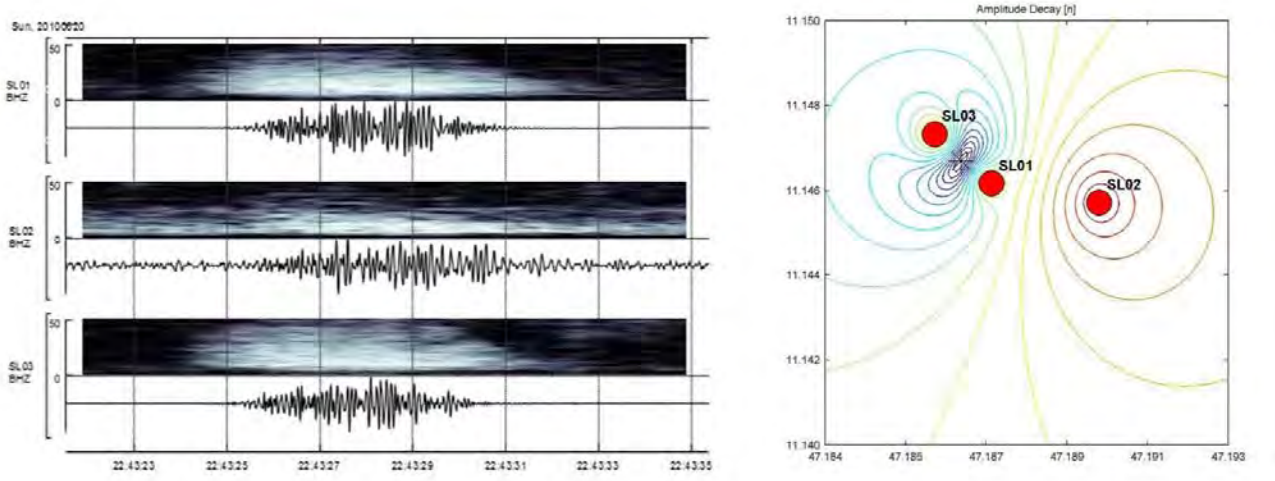

Figure 6.10: (left) Seismic traces and spectrograms of the class n event causing the large energy step in the cumulative energy on June 20 at 22:43. (right) the localization of the class n event.

7 Patterns in seismic background noise related to precipitation and groundwater infiltration

Within the framework of the master thesis "Seismic Noise Analysis at the Gradenbach Landslide "[16] written by Andrea Draxler, the ambient noise recordings of 3 years (2008 to 2010) of the seismic network Gradenbach were analyzed. The motivation of the thesis was to test, if the analysis of the ambient seismic noise is an appropriate method to gain information about the condition of the deep-seated gravitational slope deformation and its reaction to environmental influences.

7.1 Visualization and screening of the ambient seismic noise

The available data from the seismic network Gradenbach was used for the computation. The spectrograms of the years 2008 to 2010 were computed using the power spectral density (PSD) as described by McNamara and Buland[17] with slight adaptions of some parameters[16]. The window length for the PSD computation was 300 seconds with a 50% overlap. The number of spectral bins used for the Fast Fourier Transform (FFT) was 8192. This lead to spectrogram images containing 576 spectra per day. Daily-, weekly-, monthly and yearly plots were created from the spectrograms and used for the screening for anomalies in the ambient seismic noise. The spectrograms were visualized together with the displacement-, the hydrological- and the meteorological data. Two distinct patterns in the spectrogram were identified. First, the occurrence of increased seismic energy in the ambient noise at certain frequency bands with the beginning of the snow-melt and second, the occurrence of recurrent patterns in the ambient noise after peaks in the precipitation.
Figures 7.1 to 7.3 show the spectrogram of station GB02 for the time period of beginning snow melt for the years 2008, 2009 and 2010, respectively. It can be seen, that with the beginning of the snow melt indicated by a decrease of the snow water equivalent, continuous patterns in the frequency range between ~10 and 30 Hz are appearing in the spectrograms. These pattern is most prominent in the year 2009, when the slope accelerated in spring, but it is also clearly visible in the years 2008 and 2010. The continuous patterns lasted until approximately the end of autumn.

Besides these continuous patterns with durations of several months, patterns of a shorter duration following times of high precipitation where identified in the spectrogram of the year 2009 (see figure 7.4). A total of 13 events where identified in the year 2009. In the years 2008 and 2010 only some similar events were found with a less prominent characteristic (see figure 7.5 and figure 7.6). The characteristics of the events following times of strong precipitation in the year 2009 are discussed in detail in the next chapter.

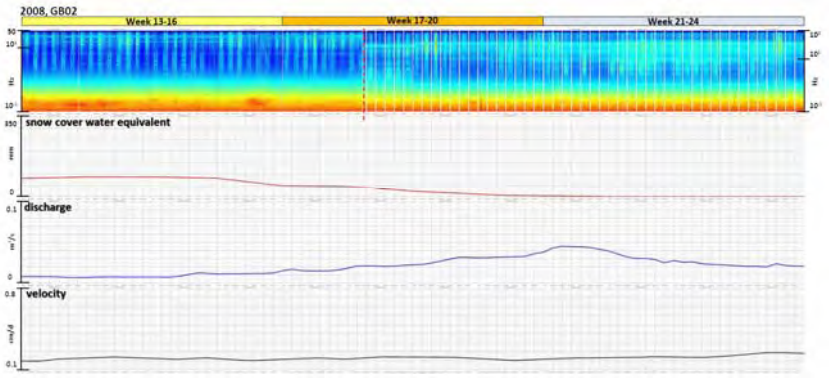

Figure 7.1:The ambient seismic noise of the weeks 13 to 24 of the year 2008. The spectrogram of station GB02 is shown together with the snow-water equivalent, the discharge of the Berchtoldgraben creek and the velocity of the slope derived from the wire-extensometer displacement data.

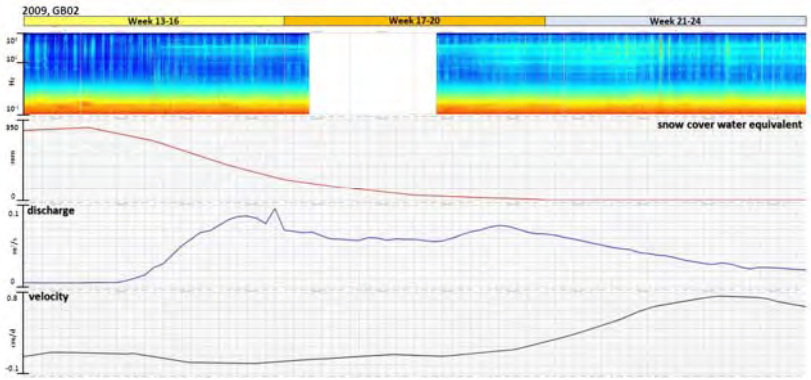

Figure 7.2:The ambient seismic noise of the weeks 13 to 24 of the year 2009. The spectrogram of station GB02 is shown together with the snow-water equivalent, the discharge of the Berchtoldgraben creek and the velocity of the slope derived from the wire-extensometer displacement data.

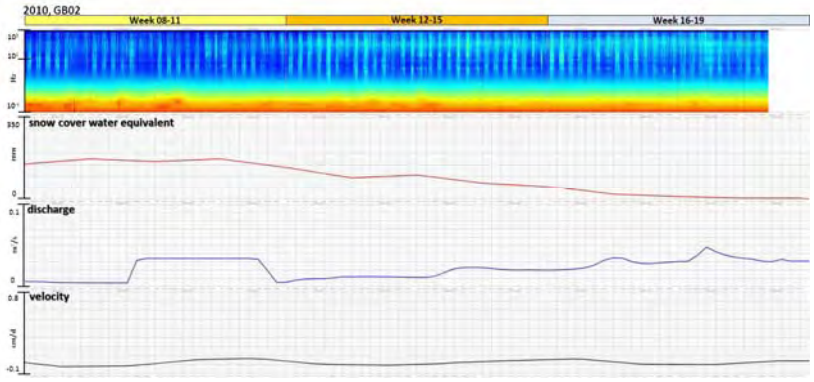

Figure 7.3:The ambient seismic noise of the weeks 13 to 24 of the year 2010. The spectrogram of station GB02 is shown together with the snow-water equivalent, the discharge of the Berchtoldgraben creek and the velocity of the slope derived from the wire-extensometer displacement data.

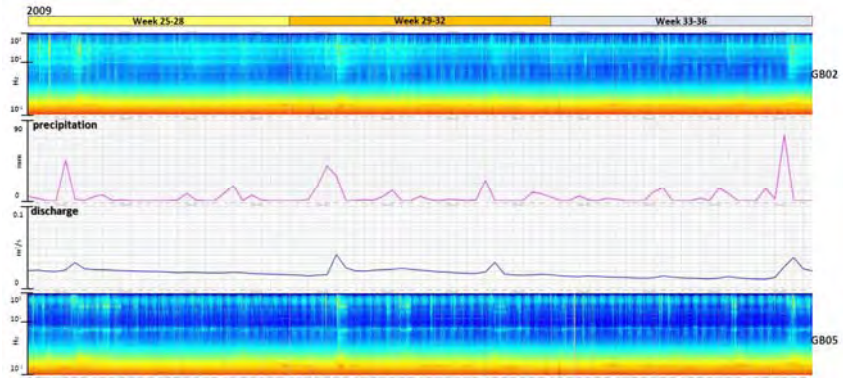

Figure 7.4: The spectrograms of station GB02 (top) and GB05 (bottom) of weeks 13 – 24, 2009 are shown together with the precipitation and discharge of the Berchtoldgraben creek. The peaks in the precipitation marked with letters c to f indicate those times of intense rainfall for which following patterns in the spectrogram were identified.

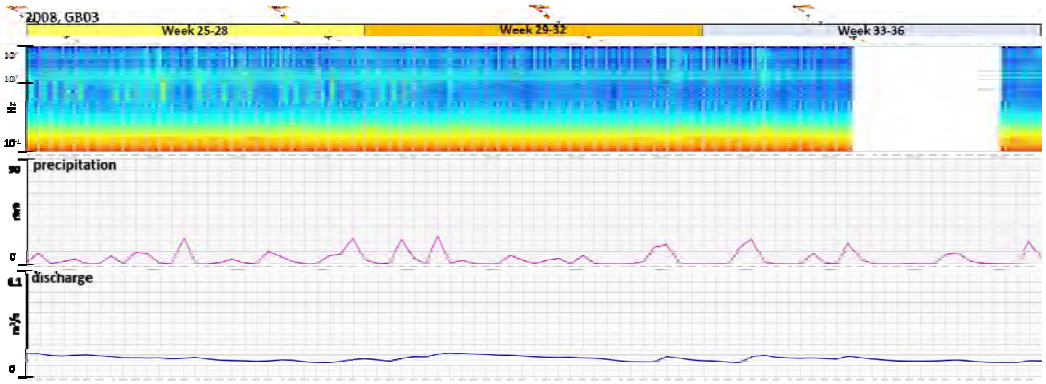

Figure 7.5: The spectrogram of station GB02 (top) of weeks 13 – 24, 2008 is shown together with the precipitation and discharge of the Berchtoldgraben creek. The peaks in the precipitation marked with letters a and b indicate those times of intense rainfall for which following patterns in the spectrogram were identified.

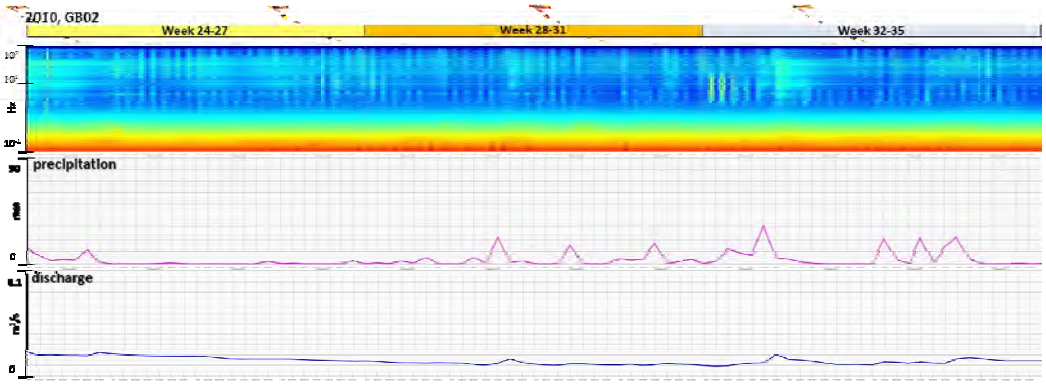

Figure 7.6: The spectrograms of station GB02 (top) of weeks 13 – 24, 2010 is shown together with the precipitation and discharge of the Berchtoldgraben creek. The peaks in the precipitation marked with letters g and h indicate those times of intense rainfall for which following patterns in the spectrogram were identified.

7.2 Ambient seismic noise events related to precipitation

To better highlight the patterns which stand out against the general ambient seismic noise, the average daily noise for each weak was computed and removed from the spectrograms resulting in differential spectrograms highlighting the variation from the general ambient seismic noise (see figure 7.7).
The differential spectrograms were used to create stacks of the events to better highlight possible similarities in frequency characteristics and temporal evolution of the events. For each event the semblance of the differential spectrograms of all available stations was computed. The common zero-point for the semblance stacks was the time of the foregoing precipitation peak. The semblance was computed for a time period of 96 hours. The semblance highlighted the similarities of the differential spectrograms of the individual stations. Two examples of semblance stacks are given in figure 7.8. They show the main characteristics of the observed signals with a high frequency onset followed by a low frequent part some hours later. This two main parts are also highlighted by the semblance stack of all 11 event semblance stacks (see figure 7.10). From this figure it can be seen, that the delay of the high- and low-frequent part of the events is systematical. The high-frequent part started ~15h after the precipitation peak. The low frequent part was delayed by ~25h after the precipitation peak.

The clearly systematic delay of the different parts of the 11 events used for the semblance stack support the assumption, that the patterns in the ambient seismic noise is related to the infiltration of the water into the slope.

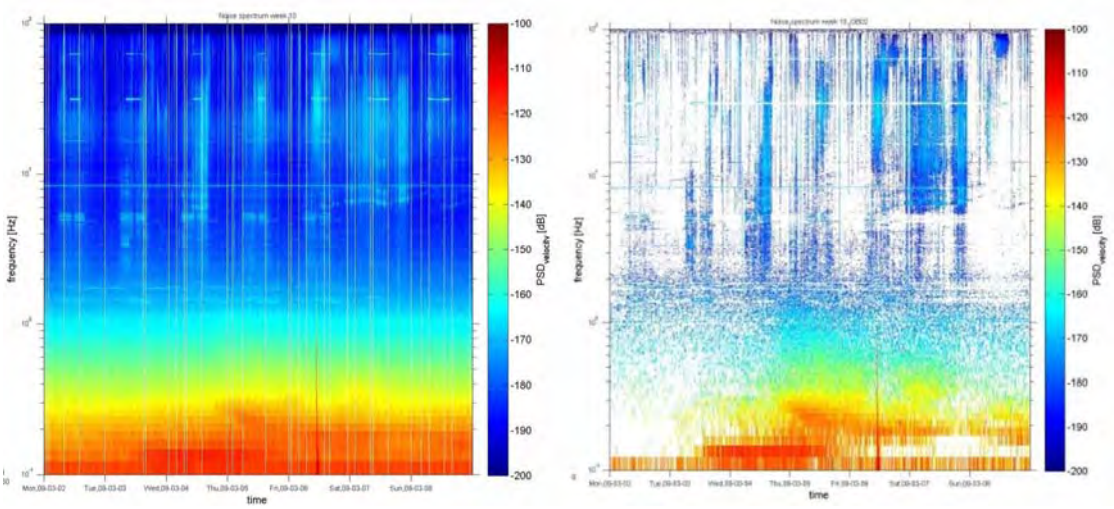

Figure 7.8: Example of the enhancement of seismic patterns in the ambient seismic noise by the removal of the daily noise from the spectrograms. Left shows the original spectrogram of one week (week 10, 2009) and the right image shows the same week after the removal of the noise.

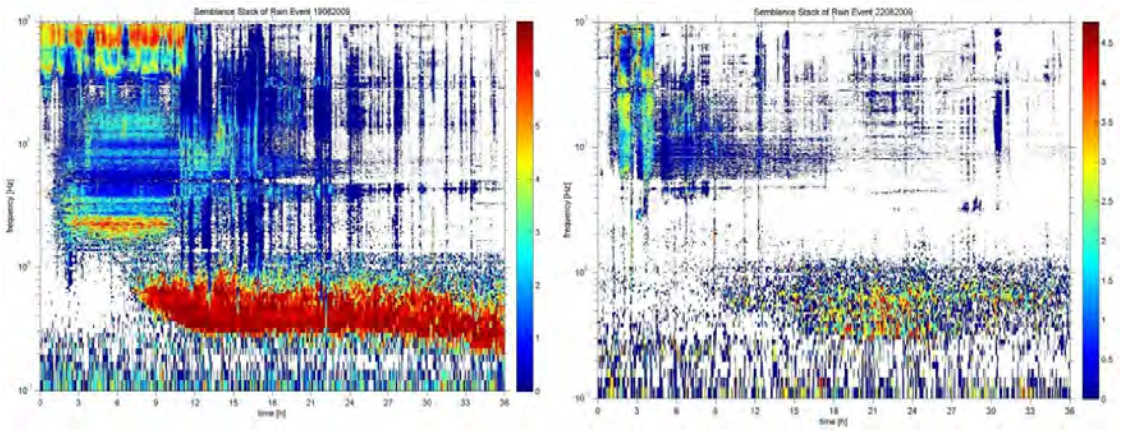

Figure 7.9: Event semblance stacks of (left) event 2 and (right) event 8.

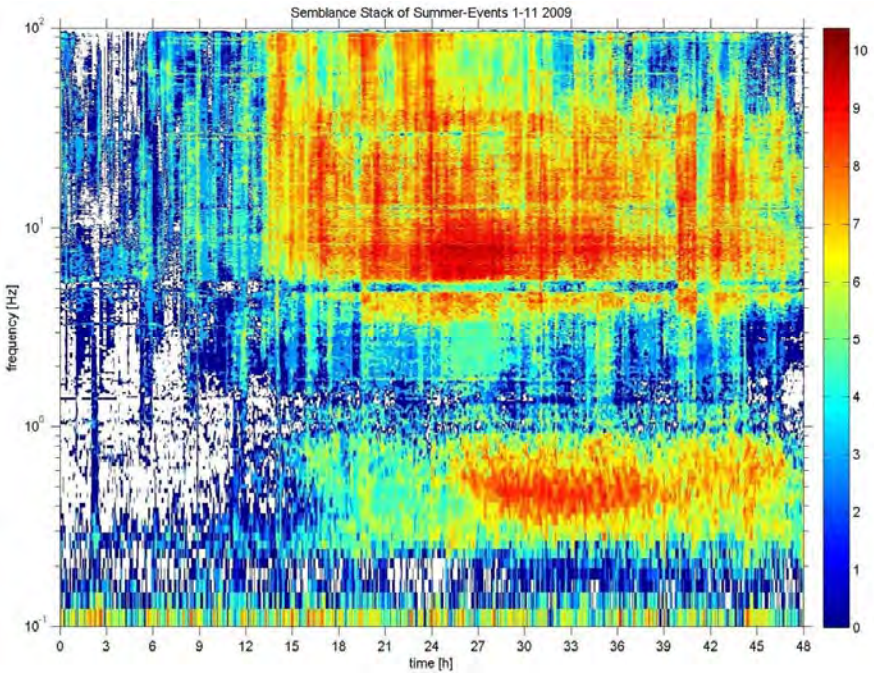

Figure 7.10: Semblance stack of 11 event semblance stacks. The time 0 corresponds with the precipitation peak foregoing the seismic signal. The high frequency part of the event starts at ~15h after the precipitation peak; the low frequent part starts about 25 hours after the precipitation peak.

8 Polarization of seismic waves recorded with surface-based stations at the Gradenbach landslide

In her master thesis "Seismic signal analysis using polarization attributes and its applications"[18], Katharina Doblhoff-Dier evaluated various methods of polarization analysis, tested them on global- and regional earthquake data recorded at the monitoring network Gradenbach and applied selected methods to the high-frequent data of the event types recorded during the acceleration of the slope. Doblhoff-Dier has implemented a vast amount of state-of-the-art polarization analysis methods in Seismon[19], and tested them on global earthquake data recorded by the ZAMG

observatoy station CONA (see figure 8.1 for an example). The following methods have been evaluated and implemented in Seismon: covariance matrix methods[20], complex covariance matrix method[21], spectral matrix method[22], instantaneous attributes method[23], and Stockwell-transform method[24,25]. A detailed description of the evaluated polarization analysis methods and their implementation in Seismon is given in the report "Implementation of a polarization analysis for Seismon"[19] .
The covariance matrix- and the complex covariance matrix method was used to analyze the polarization of local earthquake data and slope events of the acceleration phase 2009 recorded at the seismic network Gradenbach.

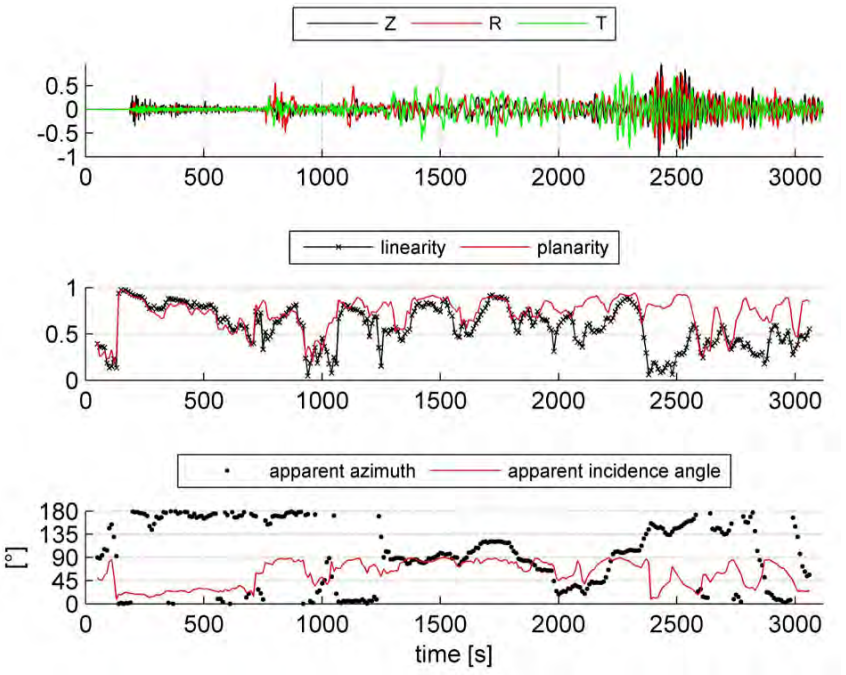

Figure 8.1: Example of the analysis of a global earthquake recorded at CONA using the covariance matrix method. (source: Doblhoff-Dier[18])

8.1 Polarization of local earthquakes recorded at the seismic network Gradenbach

An important question to answer was, if the waveforms recorded with the stations of the Gradenbach seismic network show polarization at all or if all the polarization information of the waveform was lost due to near-surface heterogenities and effects of the free surface. Therefore, the polarization of the waveforms of local earthquakes recorded with the seismic network Gradenbach was compared to that computed for broadband observatory stations of the ZAMG. Since near-surface heterogeneities disturb low-frequent seismic waves less that high-frequent waves, the bandwidth of the geophones was extended by removing the instrument response and applying a high-pass filter. The frequency response of the 4.5 Hz geophones was removed by inverse filtering and a 0.7 Hz high-pass filter was used to stabilize the inverse filtering and the restrict the investigated frequency range to those values which were not dominated by electronic noise. The data was filtered with a 0.7Hz to 2Hz or a 1Hz to 3Hz band-pass filter before the polarization analysis.

The polarization (linearity, planarity, apparent azimuth and apparent incidence) was determined using the covariance matrix method with time windows between 1s an 2s and a 95% window overlap. The polarization values were considered as significant if the linearity was higher than 0.65 and the planarity was higher than 1.4 times the linearity for at least 4 consecutive sliding windows in the near vicinity of the picked P-wave onset. Furthermore, polarization attributes were rejected if the apparent azimuth changed too rapidly with time.
With the rules stated above, the polarization of an earthquake could very often be determined for very few stations of the network. This didn't lead to an interpretable data-set. Therefore, the polarization of selected clusters of earthquakes from a common source region was computed. It was expected, that the back-azimuth computed for the earthquakes should be approximately the same.Three earthquake clusters with source regions in Friaul, Poland and the region around Innsbruck were used. The results of the computed back-azimuth are given in figures 8.2 to 8.4.

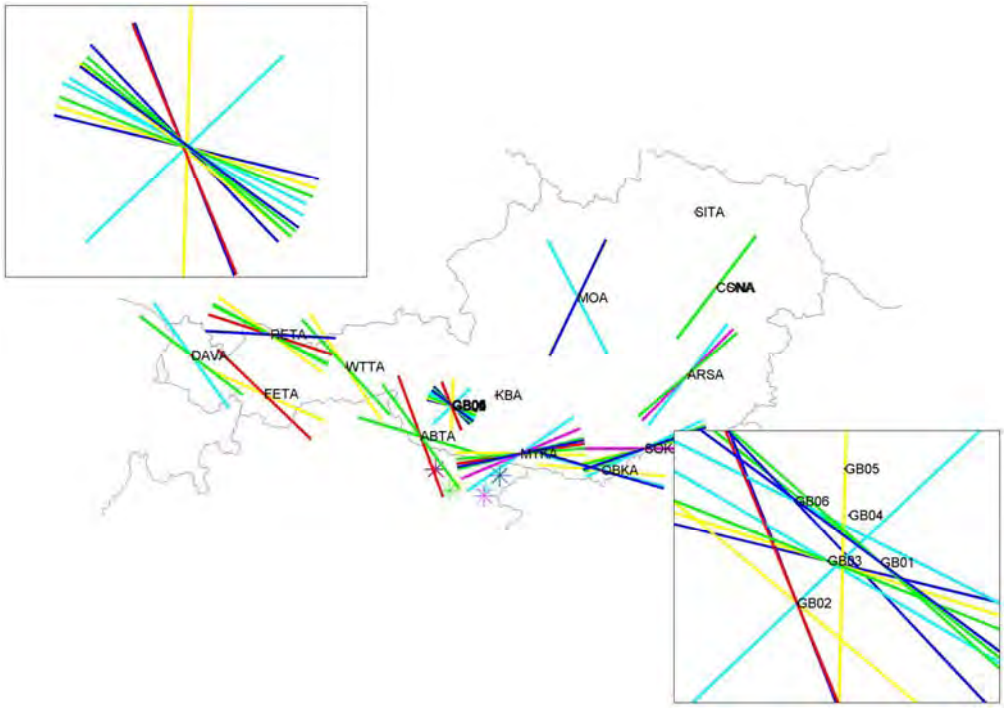

Figure 8.2: P-wave back-azimuth for several earthquakes located in the Friaul region, recorded at Gradenbach and several ZAMG observatory stations. The insets are zoomed-in views of the sations at Gradenbach (upper left: 20kmx20km; lower right: 2.5kmx2.5km). Each color depicts the results of one earthquake whose location is represented by a star in the same color. (source: Doblhoff-Dier[18])

The conclusions drawn by Doblhoff-Dier were[18]: (a) it is possible to obtain meaningful results from a polarization analysis at Gradenbach in the sense that the P-wave onset of events located close to each other typically show the same main direction of motion; (b) the polarization is weaker at Gradenbach compared to neighboring observatory stations; (c) the polarization at the Gradenbach stations could be measured less frequently with a sufficient quality; and (d) for some earthquakes with epicenters in the same region, the measured direction of motion at the Gradenbach stations showed a common bias.

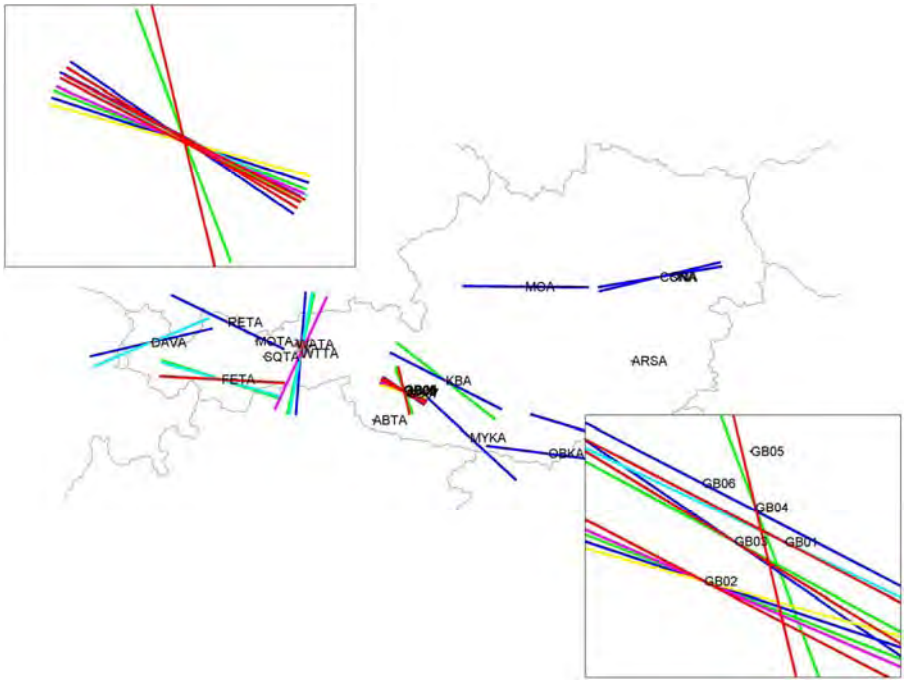

Figure 8.3: P-wave back-azimuth for several earthquakes located near Innsbruck, recorded at Gradenbach and several ZAMG observatory stations. The insets are zoomed-in views of the sations at Gradenbach (upper left: 20kmx20km; lower right: 2.5kmx2.5km). Each color depicts the results of one earthquake whose location is represented by a star in the same color. (source: Doblhoff-Dier[18])

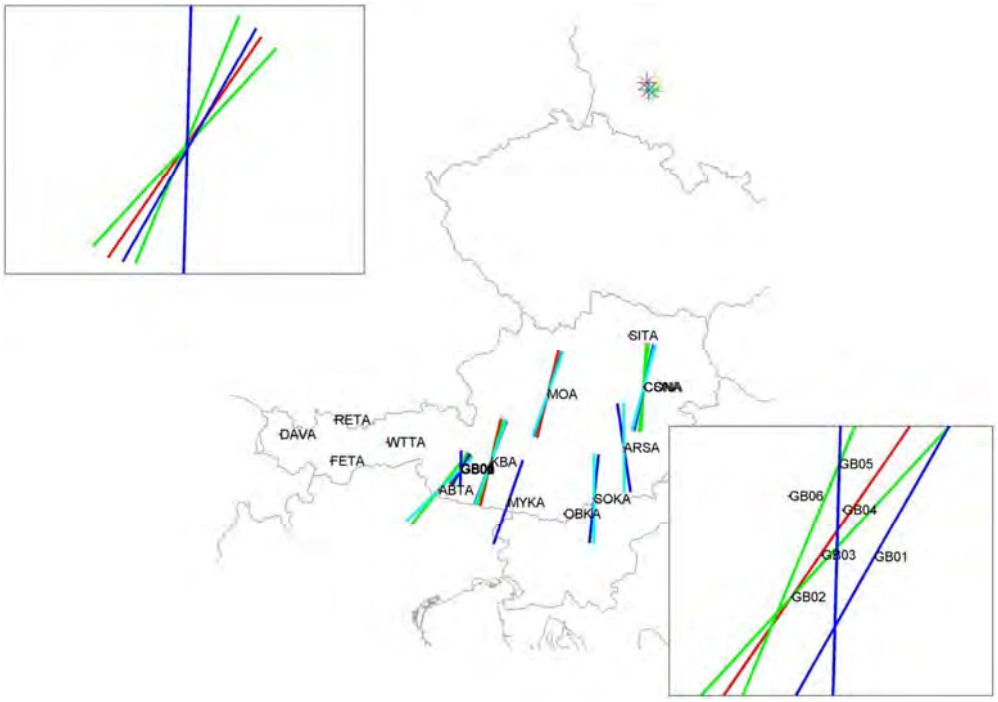

Figure 8.4: P-wave back-azimuth for several earthquakes located in Poland, recorded at Gradenbach and several ZAMG observatory stations. The insets are zoomed-in views of the sations at Gradenbach (upper left: 20kmx20km; lower right: 2.5kmx2.5km). Each color depicts the results of one earthquake whose location is represented by a star in the same color. (source: Doblhoff-Dier[18])

8.2 Polarization of event classes of the acceleration phase 2009

The analysis of the polarization of the waveform of slope events (see chapter 5.2) recorded during the acceleration phase 2009 didn't result in consistent and significant polarization attributes. For most of the events, the criteria defined in chapter 8.1 for reliable polarization attributes where not reached. This could be attributed to the higher frequency content of the slope events (> 10Hz), which could increase the influence of the near-surface heterogeneities on the waveform. Only the type B slope events showed consistent polarization attributes.

Ten type B events were analyzed using the complex covariance method with a sliding window of 1s. After the removal of the instrument response as described in chapter 8.1 , the data was filtered with a 1Hz high-pass filter. The majority of the type B events showed a stable apparent azimuth and a low degree of ellipticity over the whole event, as can be seen in figure 8.5. The average apparent azimuth was computed for all events. Especially the type B events recorded between May 15 and May 20, 2009 showed very similar apparent azimuths (see figure 8.6).

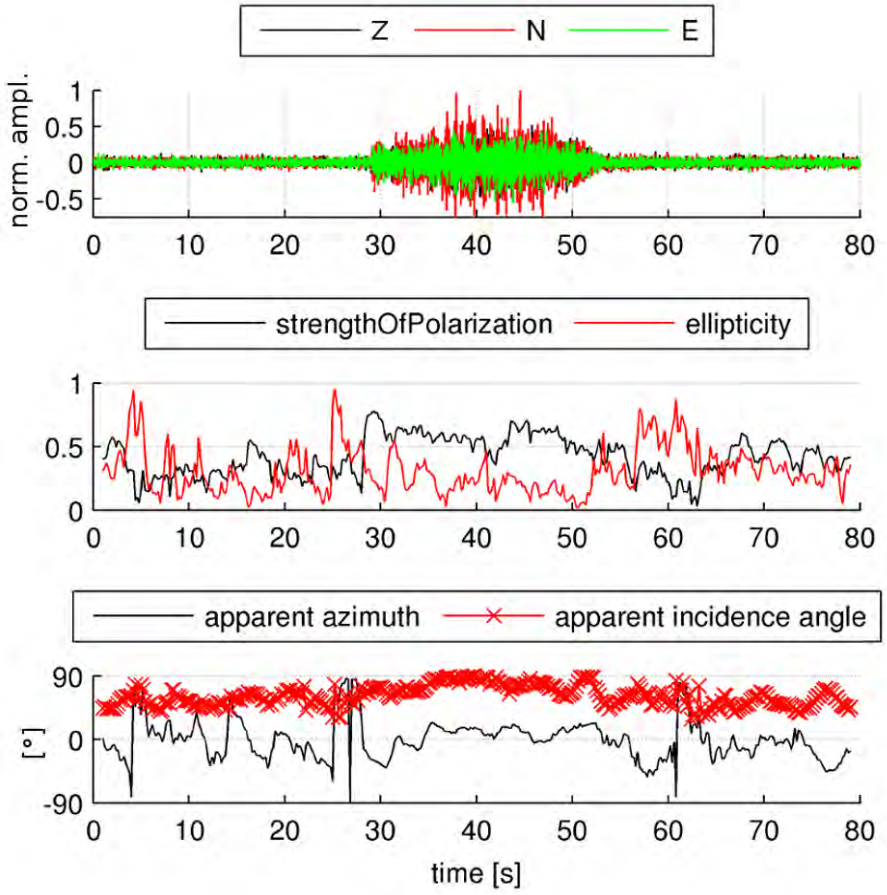

Figure 8.5: Example of the polarization of a type B event. The data was taken from the type B event on May 16, 2009 19:31:40 recorded at station GB04.

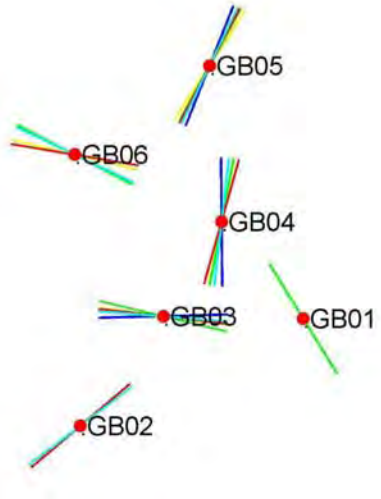

Figure 8.6: The mean apparent azimuth of type B events recorded between May 15 and May 20,2009. (source: Doblhoff-Dier[18])

9 Relation of displacement rate to hydrological parameters

From the observations made during this project at the deep-seated gravitational slope deformation Gradenbach, it is obvious that there is a strong relation between the hydrological settings, the displacement of the slope and the seismic activity. The most important factor influencing the stability of a slope is the pore water pressure[2]. Brückl et al.[2] showed that the hydrostatic water level observed in the boreholes of the Gradenbach landslide are controlled by perched water tables within the main body of the landslide and therefore are not suitable to gain direct information on the hydrostatic water level at the basal sliding zone. This lead Brückl et al.[2] to derive a proxy of this quantity from the hydro-meteorological data related to infiltration.

The infiltrating water was estimated using the snow melt and precipitation measured at Gradenbach by the BFW. The proxy of the hydrostatic water level was constructed by fitting the annual variation of the weighted sum of the total monthly infiltration (100% melt water, 50% liquid precipitation) to the mean annual variations of the hydrostatic water levels recorded by the borehole gauges. This modeling was done by filtering the average monthly infiltration with a selected operator Wp = [0 4 12 8 4] which represents the weights of the actual and 4 previous months (see figure 9.1).

Brückl and Parotidis[14] introduced the concept of subcritical crack growth as the process which controls the velocity of quasi-continuous deformation of the main body of a mass movement, but also the sliding velocity at the basal surface of rupture. Based on this concept and using a simple one-dimensional slider block model Brückl et al.[2] derived a relation between the sliding velocity $V(t)$ and the proxy of the hydrostatic water level:

$$V(t) = C_1 (proxy(t) + H_0)^n \qquad (6)$$

where the units for *proxy(t)* and H_0 is [m], n=8 according to Brückl and Parotidis[14] and the constants C_1 and H_0 are determined by fitting the integral of the calculated velocities to the corresponding values observed by the extensometer using a 2D grid search.

Figure 9.2 shows the prediction of the slope movement using equation (6) and $\mathbf{C}_1$=5.2E-8 *m/month* and H_0 =2.55 *m* for the years 1996 to 2012. The quasi-stationary phase between 2002 and 2008 and the acceleration phase in 2009 are very well modeled, also the beginning of the acceleration phase in 1999 is quite well simulated. But the large acceleration of the slope in 2001 is completely missed.

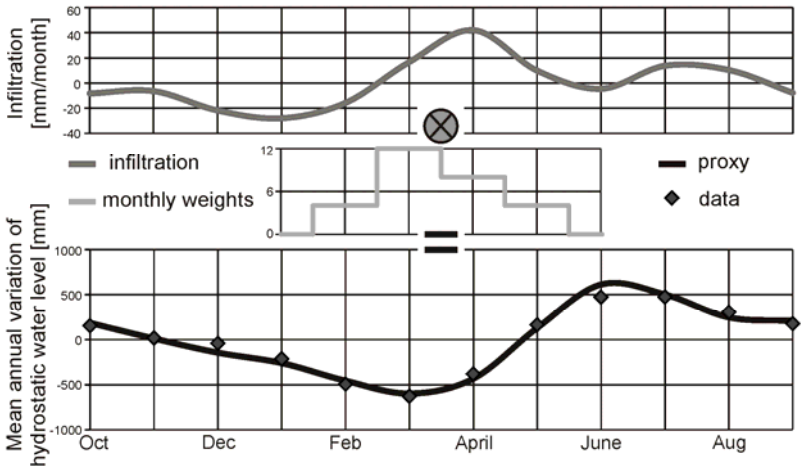

Figure 9.1: Modeling of the mean annual hydrostatic water level variations by a proxy computed by convolving the average monthly infiltration (snowmelt 100%, precipitation 50%) with the filter operator [0 4 12 8 4]. The coefficients of this operator represent the weights of the infiltration of the current and the 4 preceding months. The average monthly infiltration and the average monthly hydrostatic water level were computed as median for the period 2003 – 2012. Source: Brückl et al.[2].

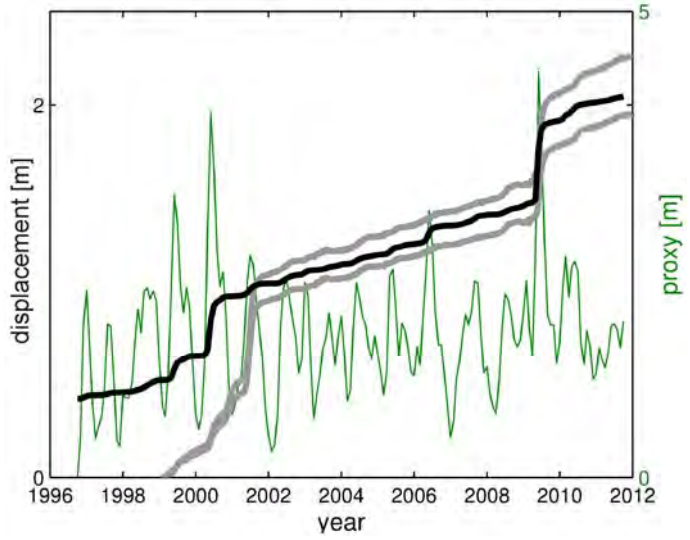

Figure 9.2: Prediction of slope movement (black line) using the proxy of the hydrostatic water level (green line) and (6). For reference, the data from the two wire extensometers (gray lines) is plotted. Source: Brückl et al.[2]

10 Unsupervised classification of seismic events using self-organizing maps

For the objective classification of seismic events recorded at the deep-seated gravitational slope deformation Gradenbach, the use of Self-Organizing Maps (SOM) was evaluated. SOM is an effective software tool for the visualization of high-dimensional data. It converts complex statistical relationships between high-dimensional data items into simple geometric relationships on a low-dimensional display. Köhler et al.[26] showed that SOM can be used for the classification of seismic waveforms. Figure 10.1 gives an example of the usage of SOM to analyze a simple data set consisting of 3 clusters of data points in a three-dimensional space. This example shows how the SOM can be used to identify groups of data points which share common attributes. A big advantage of this method is, that the identification of clusters in the data set is done without any prior knowledge of the data set itself. For this work the Matlab SOM toolbox was used.
Applied to the classification of seismic events, the data set consists of characteristic features of the seismic events (e.g. length, max. amplitude, ..). The following features where used for the SOM classification:

- the power spectral density divided into bins with a width of 2 Hz (psd_X);
- the event length;
- the standard deviation of the max. amplitudes measured on the stations (env_max_std);
- the waveform shape, which was represented by a measure of the area beneath the graph of the cumulative sum of the histogram of the envelope of the seismogram (envr);
- the energy buildup, which was measured by quantiles (25, 50, 75, 90) of the cumulative sum of the squared amplitude of the seismogram (eb_12, eb_50, eb_75, eb_90, ebr).

The unsupervised classification of the seismic events recorded at Gradenbach using SOM and k-means clustering was tested. The k-means cluster algorithm groups a set of data points into k clusters, so that the quadratic variation of the data points from the center of the cluster is minimized. The result of a mapping of selected features of the slope events to SOM is given in figure 10.2. Each map shows the mapping of the events which where interactively classified. The features given in the component maps in figure 10.3 where used. Ideally, for each map, the data points should form unique clusters. It can be seen, that there is a certain amount of separation among the interactively classified event types, but the interactive classification is not reproduced exactly by the SOM mapping and clustering. Most of the type tremor events are assigned to the purple and magenta clusters, type B events are mostly contained in the gray cluster. Many of the type D events are contained in the beige region, but there are also a lot of these event types spread in other clusters and mixing up with type A events. The type AA and type rf, which were clearly distinguished in the interactive classification don't form any clear cluster.
This shows, that the method itself may be suitable for the automatic and unsupervised classification of the slope events, but some features have to be added to better separate the event types.

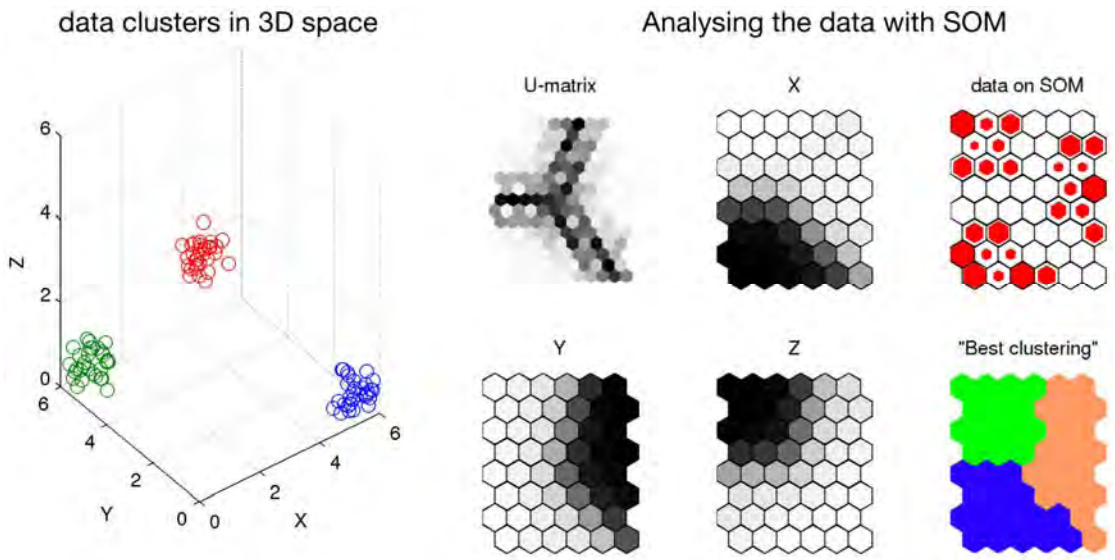

Figure 10.1: Illustration of an application of SOM to visualize the properties of a simple three-dimensional data set. The xyz data which is separated into 3 clusters (red, green and blue data points on the left) are analyzed using SOM. The coordinates are mapped to the hexagonal map. Each data point can be mapped to the SOM (data on SOM) and a k-means clustering separates the data points into three groups ("Best clustering").

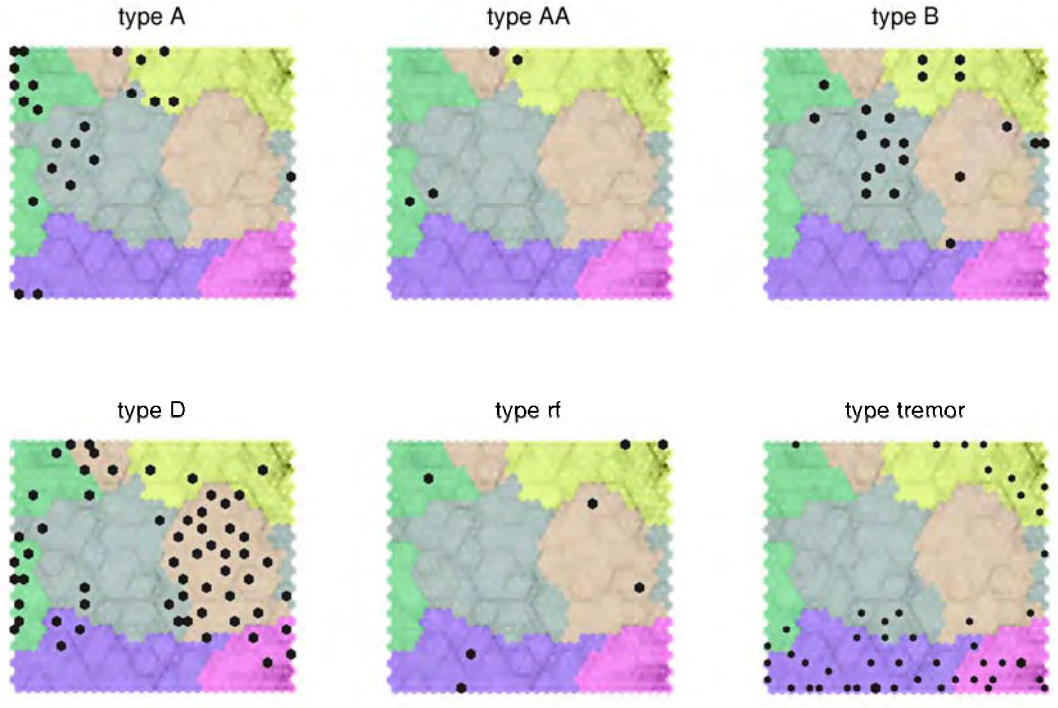

Figure 10.2: The mapping of the Gradenbach slope events on SOM. The k-means clustering with 6 clusters is overlayn.

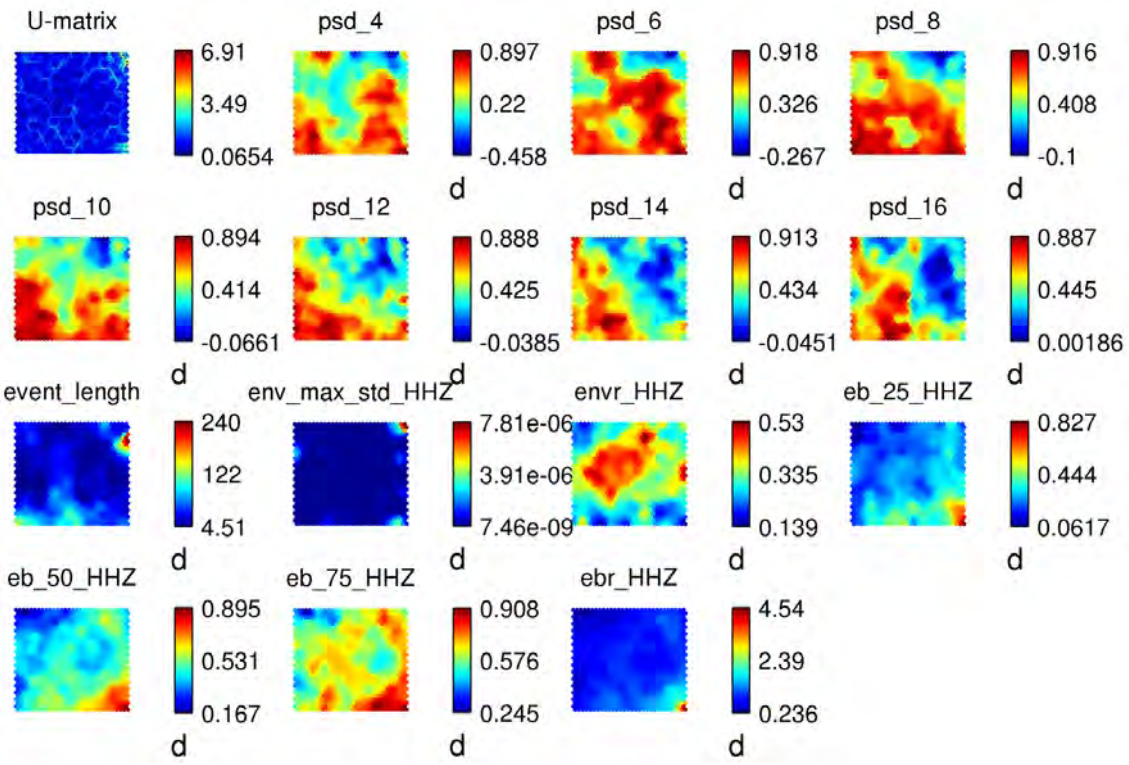

Figure 10.3: The component maps of the features used for the SOM given in figure 10.2.

11 Near real-time visualization of seismicity at the Gradenbach landslide

The NRT data of the seismic network Gradenbach is continuously processed to create power spectral density (PSD) plots (see chapter 7) for the visualization of the seismic activity. The PSD plots are uploaded to the homepage of the Gradenbach Observatory where they are visualized online together with the deformation and hydro-meteorological data[2] .
The Gradenbach observatory homepage http://gbonline.tugraz.at was programmed by the Institute of Engineering Geodesy and Measurement Systems at the Graz University of Technology.

Daily- and weekly PSD plots are computed and uploaded to the server every hour. The PSD plots with a period of 4 weeks are computed once every day at midnight. Figure 11.1 shows a screenshot of the Gradenbach Observatory homepage showing the seismic monitoring section.

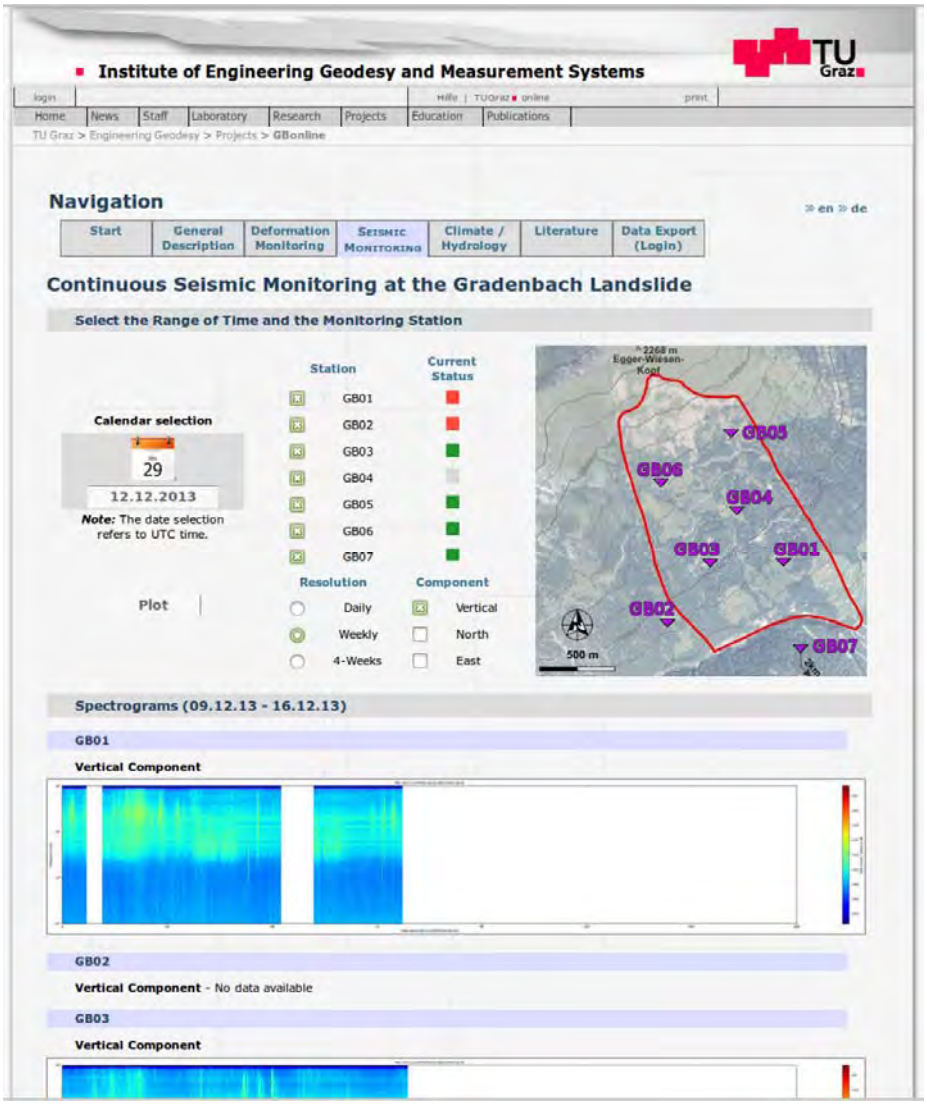

Figure 11.1: Screenshot of the Gradenbach Observatory homepage showing the seismic monitoring section.

12 Data processing methods

To process the data recorded at the study sites Gradenbach and Steinlehnen, several processing methods have been developed, adapted and used. This chapter describes the base of these processing methods. More detailed descriptions can be found in the according dissertation[7] and master thesis[9].
Much work has been done to develop methods for detecting and classifying seismic events without any prior knowledge of the events to be detected.

12.1 STA/LTA event detection

For the detection of seismic events at Steinlehnen, a STA/LTA detection algorithm [28,29] was used. The STA/LTA algorithm detects amplitude variation in a seismogram by comparing the short-term average (STA) of a characteristic function (e.g. absolute value) derived from the time-series with the long-term average (LTA) of the

characteristic function. The STA and LTA are computed as moving average filters of different length. The LTA mimics the ambient seismic noise and the STA represents the short-time variations (events) of the seismogram.
The vertical component of the seismic data, filtered with a 1Hz Butterworth high-pass filter was used for the STA/LTA event detection. The characteristic function was computed using the square of the envelope of the seismogram. Figure 12.1 shows the principal steps used for the described STA/LTA event detection. For the STA and LTA functions, moving average windows of 1s and 3600s length were used, respectively. To avoid the disturbances of the STA and LTA function due to short signals with very large amplitudes (e.g. spikes due to electronic disturbances), the to averages were computed using the median. To reduce the computational cost, the LTA was not computed as an overlapping, moving average, but for fixed, non-overlapping time-spans of 3600s length. The STA was computed for each time-sample as a true moving average filter.
The threshold function thrf was computed by

$$thrf = \frac{STA}{LTA} \tag{7}$$

To declare the start and end of an event, the thrf function was compared with the thr_{start} and thr_{stop} criteria. If thrf excessed thr_{start}, the start of an event was declared. Once the start of an event has been declared, thrf was compared to the thr_{stop} value, which usually is smaller than thr_{start}. If the thrf went below thr_{stop}, the end of the event was declared and the comparison of thrf with thr_{start} was activated again. The threshold values used for the event detection were: thr_{start} = 12, thr_{stop} = 8.
The selected threshold values resulted in a very sensitive detector. This caused a large amount of false positives, which usually were noise burst with a short duration. To remove these false positives from the detected events, events with an event length smaller than 1s were rejected. Additionally, consecutive events with a gap between the two events smaller than 1 second have been combined to a single events.

The limits of the detected events were extended with pre- and post-event time windows of 1s to ensure, that the complete event was included inside the event limits.

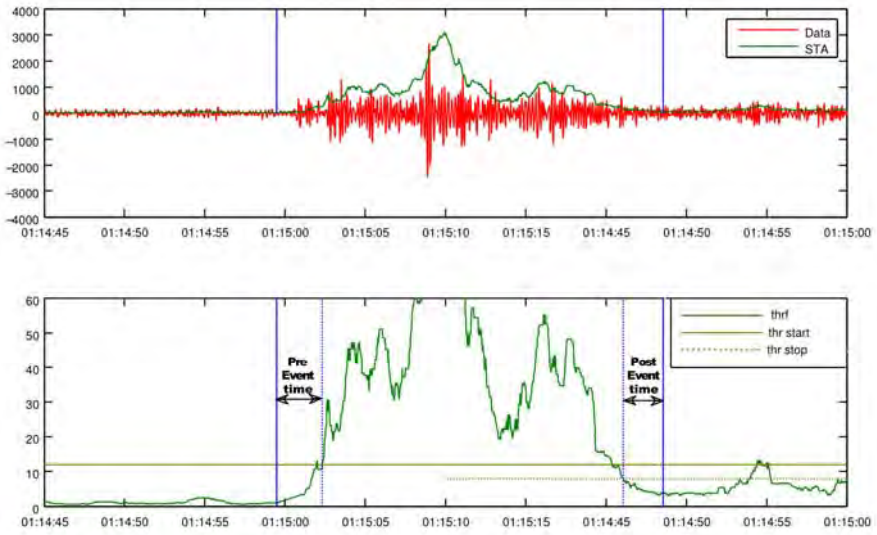

Figure 12.1: Example detection of an event illustrating the parameters used for tuning the STA/LTA detector.

12.2 Pattern extraction event detection

For the detection of the seismic events recorded with the seismic network Gradenbach, a detection algorithm based on extraction of signal patterns from spectrogram images was developed by Stefan Mertl[7]. Compared to the STA/LTA approach described in chapter 12.1 , the pattern extraction is more suitable for detecting events with a low signal-to-noise ratio and no prior knowledge of the characteristics of the event.

The base of the pattern extraction is the spectrogram of a seismic trace. It is computed as the short time Fourier transformation of the seismogram. The advantage of the spectrogram is that is visualizes the signal in a way that is very easy to read for humans and to identify patterns which stand out against the general ambient seismic noise. The aim of the pattern extraction event detection is to mimic this ability of humans using computer algorithms.

The major steps that are involved in the pattern extraction are (a) compute the spectrogram of a seismogram, (b) find all signals in the spectrogram and (c) extract these signals from the spectrogram. The flowchart in figure 12.2 outlines the processing steps used to extract patterns from the spectrogram and figures 12.4 to 12.8 show the major steps of the flowchart in figure 12.2 for one example seismogram (see figure 12.3).

The processing starts with the computation of the spectrogram as a short-time Fourier transformation (SFT) using the spectrogram function of Matlab. During the whole processing, the spectrogram is treated as an image without any physical background.

A logarithmic scaling is applied to the spectrogram and the noise-model computed for the processed time-span is removed from the spectrogram (figures 12.4 and 12.5). The noise removal eliminates the stationary transients (e.g. electronic hum) and highlights any variation from the seismic background noise. It has to be emphasized, that the noise model and thereafter the pattern extraction result

strongly depends on the processed time-span. To extract the patterns from the noise-free spectrogram, a seeded region growing algorithm[29,chap.10] was used. The region growing procedure starts with a set of seed points (figure 12.6) from which the regions are grown by appending neighboring pixels based on some predefined rules (e.g. similar intensity values). The seed points and the region growing spectrogram (a blurred and contrast stretched version of the noise-free spectrogram, figure 12.7) were taken as the input of the region growing algorithm to extract the patterns in the region growing spectrogram. Pixels neighboring the seed points are joined to the region until the intensity difference between the seed point pixel and the neighboring pixel drops below a threshold value. The resulting binary image is further cleaned using image closing and opening (see figure 12.8). A more detailed description of the pattern extraction algorithm including all equations needed to reproduce the pattern extraction algorithm is given in the dissertation "Characterization of local seismic events on the deep-seated gravitational slope deformation Gradenbach."[7]

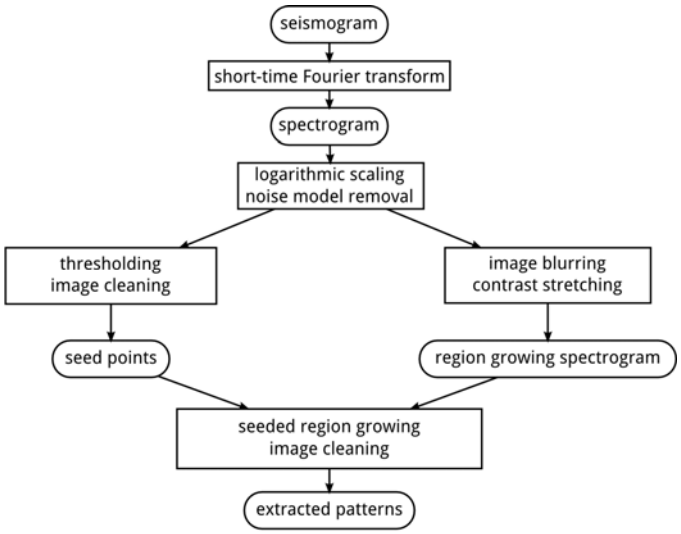

Figure 12.2: The flowchart of the pattern extraction processing steps.

The pattern extraction is a single station process and, depending on the analyzed time-span, usually results in a huge amount of signal patterns without any relation to each other. The most important point in declaring a seismic event is the occurence of related seismic signals on multiple stations with traveltime differences that reasonably reflect the local velocity structure. In local- and regional earthquake analysis, the event-binding usually requires a sophisticated algorithm. This includes the localizations of possible hypocenters to compute theoretical travel-times to which the first onsets of the detected patterns are compared to. Because for many weak events reliable first onsets can't be determined, a simplified algorithm using the begin times of the extracted patterns to bind the single-station events has been used. This simplification adds the drawback of a larger amount of false positive event declarations. The comparison of the event begin times is done using a complete linkage cluster analysis of the travel-time differences. The result of the event binding process is a list of events with a quality factor. The quality factor is the number of stations on which a pattern contributing to the event has been extracted.

The higher the quality factor, the more likely the detected event is a seismic event of special interest. Figure 12.9 gives an example of a detected event with contributing patterns on six stations.

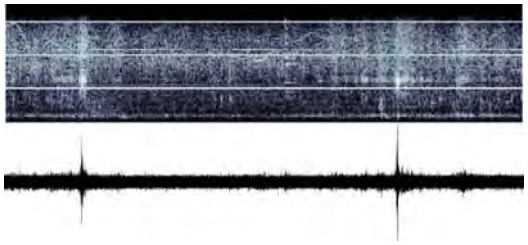

Figure 12.3: Seismogram (bottom) and spectrogram (top) of a 5 minutes recording at Gradenbach. The axes of the seismogram and spectrogram are omitted on purpose because for the dection process, which treats the spectrogram as an image, these values are not of interest.

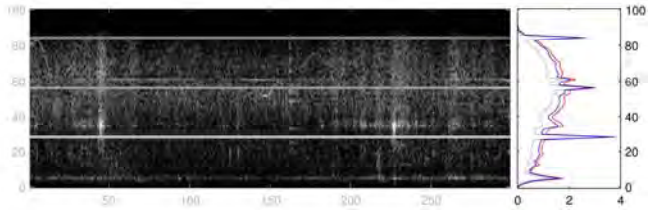

Figure 12.4: The original spectrogram and the computation of the noise model. The logarithmic scaled spectrogram is shown on the left. The noise-model is computed using the median (M50 percentile, gray line on the left) of each frequency bin and adding a representation of the noise variation. This variation can be represented by the differences of the M75 - M50 percentiles or the standard deviation (each computed along the frequency bins). The blue line shows the M75-M50 difference added to the median and the red line is the standard deviation added to the median.

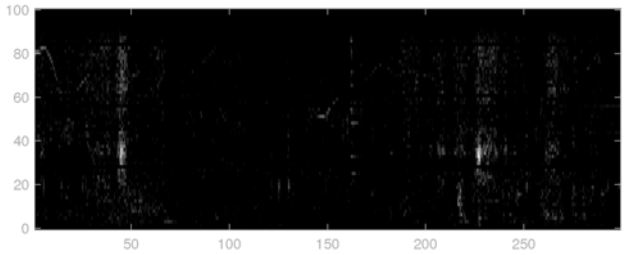

Figure 12.5: The spectrogram after logarithmic scaling and removal of the noise model.

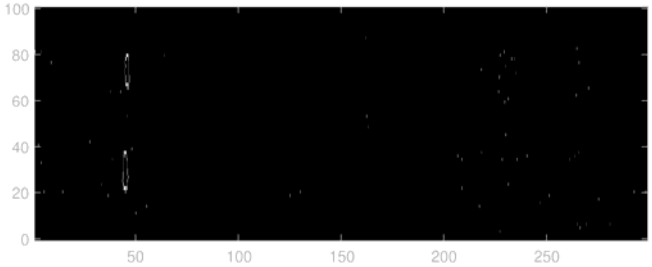

Figure 12.6: Computed seed points used for the seeded region growing algorithm.

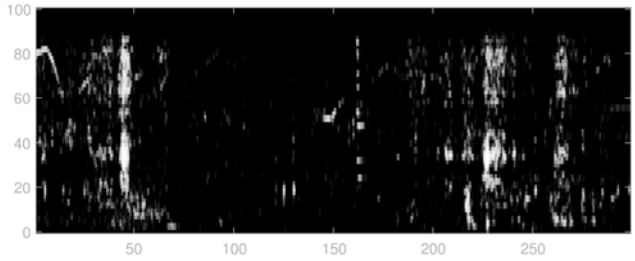

Figure 12.7: Blurred and contrast stretched region growing spectrogram.

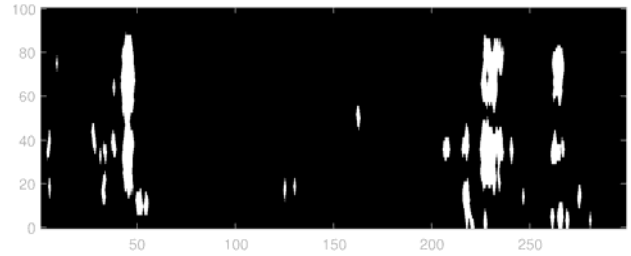

Figure 12.8: The extracted patterns after cleaning the patterns by closing and opening of the image.

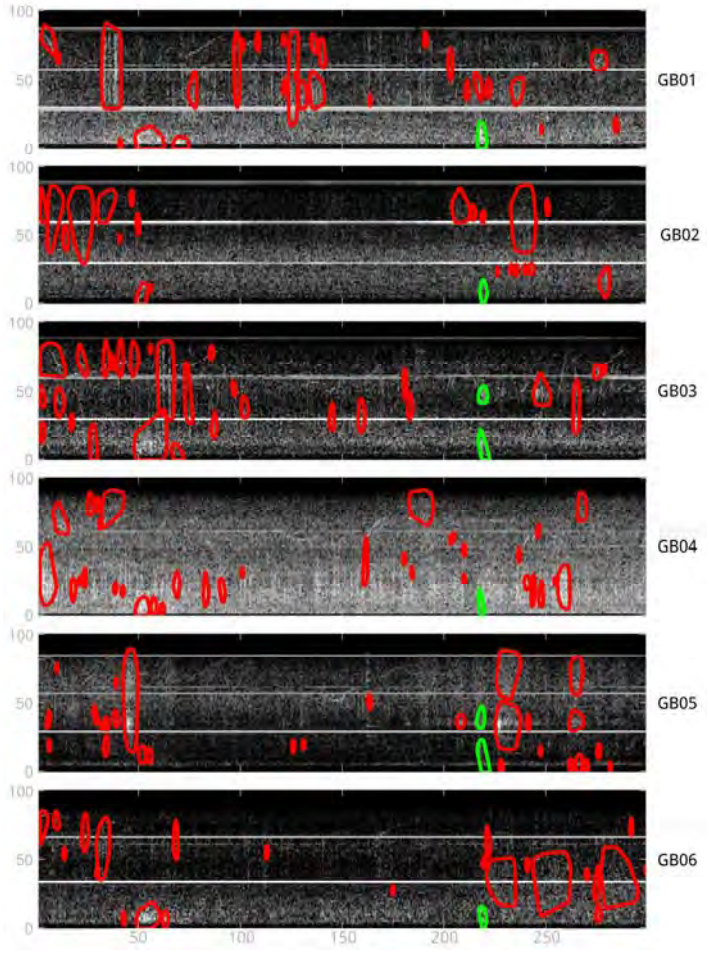

Figure 12.9: This example demonstrates the event binding based on cluster analysis of the begin times of the single station events. The red polygons mark the extracted patterns on each station. The green polygons highlight the patterns which have been linked to a common event recorded on 6 stations.

12.3 Event localization using seismic waveform amplitudes

In many cases of seismic events recorded on the mass movements Gradenbach and Steinlehnen, reliable phase time picks couldn't be determined. This was mainly caused by gradually rising amplitudes at the onset of the events or by a small signal to noise ratio. For these events, a localization algorithm based on the amplitude decay of seismic waves was used. Similar localization methods were already used for the localization of rock-falls[30] and pyroclasitic flows[31]. The used algorithm is based on the time-difference of arrival (TDOA) localization methods[31,32]. This algorithm was adapted to observed amplitude differences between two stations and it was implemented as a grid-search.
From a set of N stations of a seismic network, all possible pair-wise combinations of the station locations s_{ij}, where i = 1…N and j = 1…2, are created. For each station-pair p and q, the difference of the logarithm of the observed maximal amplitudes is computed:

$$dA_{pq}^{obs} = \log(A_p) - \log(A_q) \quad (8)$$

A regular grid g_{km}, were each grid point located at (x_{km}, y_{km}) represents a possible seismic source, is created. The theoretical amplitude G_{pkm} measured at station p from a source at g_{km} is computed based on a given amplitude decay d with distance r for every grid point.

$$r_{pkm} = \sqrt{(s_{p1} - x_{km})^2 + (s_{p2} - y_{km})^2} \quad (9)$$

$$G_{pkm} = \frac{1}{r_{pkm}^d} \quad (10)$$

These grids are used to compute a grid of theoretical amplitude differences measured at stations p and q with a source at grid point g_{km}:

$$dA_{pqkm}^{the} = \log(G_{pkm}) - \log(G_{qkm}) \quad (11)$$

To find the location of the seismic source, the minimum of the sum of the squares of the errors between the observed and theoretical amplitude differences is searched. Therefore, for each station-pair p,q, the sum of the squares of the differences between the theoretical and observed amplitude differences is computed:

$$R_{km} = \sum_{p=1}^{N} \sum_{q=1}^{N} (dA_{pqkm}^{the} - dA_{pq}^{obs})^2 \quad (12)$$

The minimum of the grid R_{km} is the location of the seismic source of the observed signal. An example localization of a rockfall is shown in Figure 12.10.

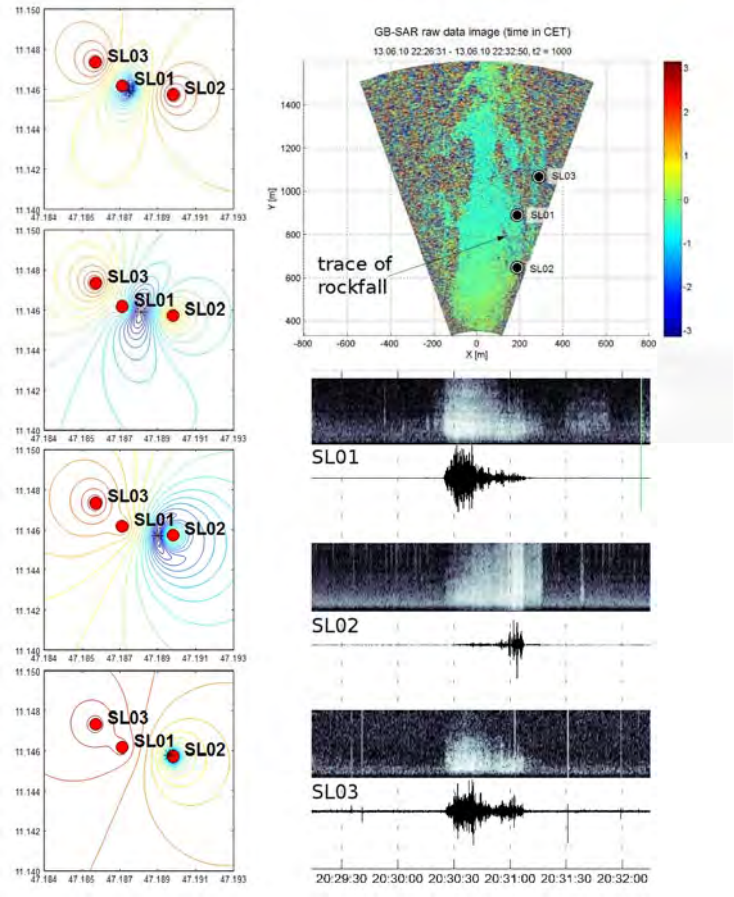

Figure 12.10: Example localization of a rockfall. The GB-SAR image (top right) shows the trace of the rockfall which was recorded by the stations SLO1, SLO2 and SLO3. The rock starts near station SLO1 and travels towards station SLO2. The 4 localization results on the left side show the epicenters of the rockfall at 4 different moments.

12.4 Interactive event screening and classification

To validate the detection results from one of the detection methods described in chapters 12.1 and 12.2 , the dataset is screened by an operator using the results from the event detection presented in an intuitive way along with the seismic data. The spectrogram with the signal enhancement, the detected events and additional information (e.g. earthquake catalogues, observatory waveform data) is displayed on the computer screen using the Seismon software (see figure 12.11). The aim of the event screening is to remove all known seismic signals (e.g. earthquakes, man-made signals) and obvious seismic noise from the data set and to keep only those events, that are likely to be caused by the displacement of the slope. The event screening and classification can be divided into the following major steps:

- Eliminate seismic events of known sources (e.g. earthquakes);
- Eliminate events that are not related to a natural seismic source (e.g. man-made noise, sonic signals);
- Find similarities in features (e.g. frequency content, waveform) to divide the remaining events into classes;
- Check of the plausibility of the mass-movement being the seismic source of the event classes.

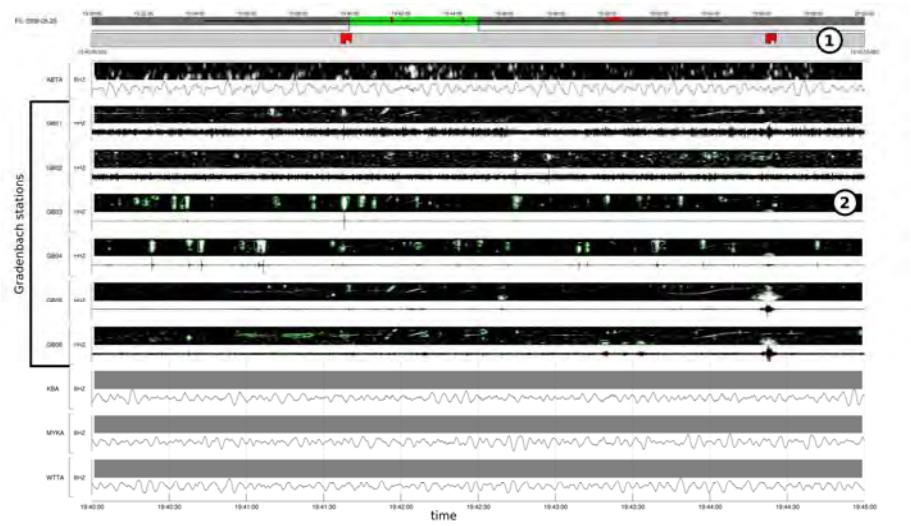

Figure 12.11: Example of a dataset displayed for event screening in Seismon. (1) is the area showing the event markers of the events detected by the pattern extraction. (2) are the vertical component traces with the extracted patterns of the stations (GB01 - GB06) located at the mass movement. The other stations show the waveform data from nearby observatory stations for better identification of earthquakes.

12.5 Objective classification using fuzzy logic

The interactive classification described in chapter 12.4 is heavily biased by the experience of the person doing the classification. To avoid this influence and to create reproducible classification results an objective classification is desirable. For data-sets with known event types and where these event types can be characterized which certain event properties computed from the seismic data, a classification based on fuzzy logic can be used.

To perform a fuzzy logic classification, a training data set with seismic events which already have been assigned to a certain class is needed. The training dataset usually is determined using the interactive event screening and classification methods. From the training data set, which should contain events which can be clearly assigned to certain event class, a set of characteristic properties (e.g. event length, max. amplitude) of each event is computed. From these properties, limits are computed which characterize a certain event class (e.g. 0<= event length <=5 class A; 5 > event length <= 10 class B). Ideally, the limits of the characteristic properties of events of individual event classes don't overlap, and an event can be clearly assigned to an event class. In reality, the characteristic properties of the event classes are overlapping and a clear assignment to a single event class is not possible. For these cases, fuzzy logic[34] is a valuable tool to perform the classification based on the diffuse separation of the event subsets. Weginger[9] describes how the results of the interactive classification of the seismic events detected at the rockslide Steinlehnen were used to determine the parameter limits for the fuzzy classification. The properties used for the fuzzy classification of this study were:

Event length

The event length is based on the STA/LTA detection results described in chapter 12.1 and it is defined as the time-period between the event start and the event end.

Average event amplitude

The average event amplitude is the mean value of the absolute value of the amplitudes of the whole event length.

Polarization attributes linearity, planarity, apparent azimuth, apparent incidence

To compute the polarization attributes, the covariance matrix method[20] (see also chapter 8 and project report "Implementation of a polarization analysis for Seismon"[19]) was used. Standard polarization attributes[20,35] linearity, planarity, apparent azimuth and apparent incidence were used for the fuzzy classification.
From the covariance matrix, the eigenvalues and eigenvectors are computed. Based on these values, the polarization attributes are defined as

$$\begin{aligned} linearity\ L &= 1 - \frac{\lambda_2}{\lambda_1} \\ planarity\ P &= 1 - \frac{2\lambda_3}{\lambda_1 + \lambda_2} \\ apparent\ azimuth\ \theta &= \arctan\left(\frac{\Lambda_{1,E}}{\Lambda_{1,N}}\right) \\ apparent\ incidence\ \alpha &= \arccos(\Lambda_{1,Z}) \end{aligned} \tag{13}$$

where λ_i are the eigenvalues of the covariance matrix and, $\Lambda_{1,E}$, $\Lambda_{1,N}$ and $\Lambda_{1,Z}$ denote the east, north and vertical component of the the eigenvector corresponding to the larges eigenvalue of the covariance matrix.

Autocorrelation

The autocorrelation function R_{xx} at lag j for a discrete signal x

$$R_{xx}[j] = \sum_n x_n x_{n+j} \tag{14}$$

is used to characterize the self-similarity and the frequency content of the seismic signal. The characteristic parameter used for the classification is the first zero crossing of the autocorrelation function. The autocorrelation function of the seismic waveform and the envelope were used (see figure 12.11).

Cross-correlation

The cross-correlation function R_{xy} at lag j for the discrete signals x and y

$$R_{xy}[j] = \sum_n x_n y_{n+j} \tag{15}$$

is used to characterize the similarity of the waveform between two stations. If the waveform is similar for all stations of the network, the cross-correlation functions will have a maximum around the zero-lag of the cross-correlation function. If the waveform varies among the stations of the network (e.g. signals of rockfalls passing

seismic stations at different times), the cross-correlation function will show a maximum with an offset from the zero-lag (see figure 12.13). The characteristic parameter used for the classification is the offset of the maximum of the cross-correlation function from the zero-lag. The cross-correlation function is computed using the envelope of the seismic signal.

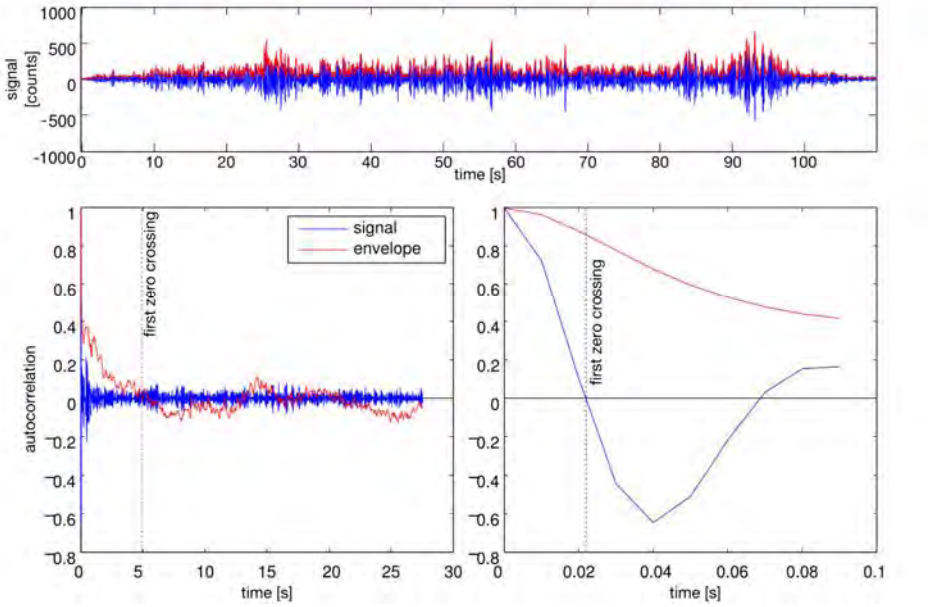

Figure 12.12: Example of the autocorrelation of an event. Top: (blue) the seismic signal and (red) its envelope; Bottom left: (blue) the autocorrelation function of the seismic signal and (red) the autocorrelation function of the envelope; Bottom right: a zoomed verision of the autocorrelation functions.

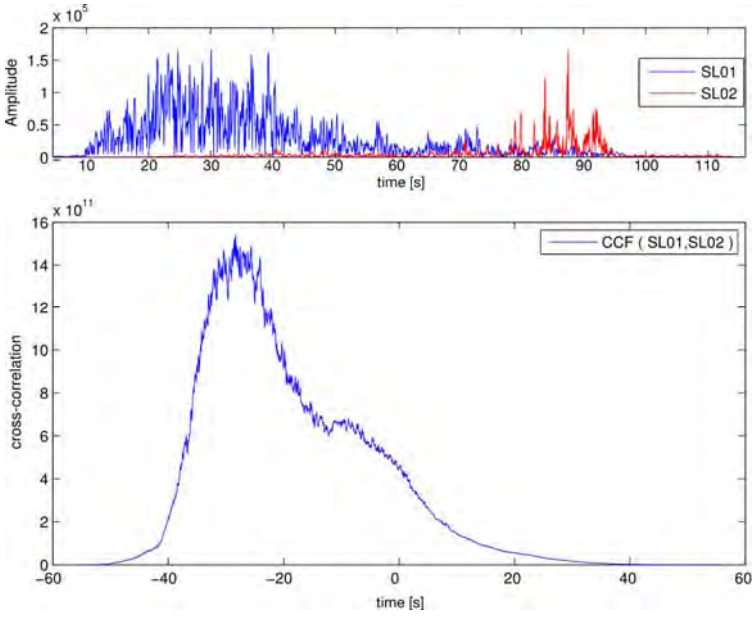

Figure 12.13: Example of the cross-correlation of an event. Top: the envelopes of the seismic signal of an event recorded at (blue) SLO1 and (red) SLO2; Bottom: the cross-correlation function of the envelopes. The offset in the cross-correlation function is clearly visible.

Amplitude histogram

The cumulative sum of the sorted amplitudes was used to characterize the shape of the waveform. The ratio of the area above and below the curve of the cumulative sum was used as a property for the fuzzy classification[9].

13 Processing software Seismon

Seismon is a seismic processing and prototyping software written for Matlab and licensed under a GNU General Public License (GPL). Seismon started as a simple tool for the import of various seismic data formats, but rapidly grew to a processing tool used within many research projects accomplished at the Department of Geodesy and Geoinformation like the seismic monitoring of landslides, local earthquake monitoring, tunnel seismic while drilling, seismic interferometry and active seismic experiments in alpine areas.
Seismon provides a graphical user interface (GUI) for a convenient handling of the processing tools and it moreover simplifies the extension of the processing methods by adding custom functions.

13.1 Software design

To fulfill the goal of a flexible software, Seismon was coded in a modular approach. The main program (named Seismon-core within this thesis) acts as a frontend to a MySQL database and manages a set of packages, which provide the functionality (modules) to Seismon (see figure 13.1). Moreover, the packages can add tools to already existing modules. This comes in handy if one wants to customize big modules (e.g. adding some special filter algorithm to the waveform display module) without changing the code of the module itself. Most important, the division into packages and modules guarantees a maintainable code.
The Seismon packages are loaded by Seismon-core during the start of the program. Each package contains one or more modules which provide various functionality to the user (see figure 13.2). During Seismon startup, two package interface functions, prefix installation.m and prefix init.m (prefix is a packages specific unique string) are called to register the modules within Seismon-core and perform some installation tasks (e.g. compile files, install documentation, …). The prefix database.m function is called only once when Seismon-core recognizes a new package. The prefix database.m function can be used to add additional database tables to the Seismon database structure. A module is a set of Matlab functions which can be accessed by Seismon using two interface functions (the module functions). The module functions (edit-function and command-function) have to be coded following given guidelines. The edit-function is called by Seismon-core to edit the configuration parameters of the related module. The command-function is called by Seismon-core when the module is executed. The module functions may call several subfunctions which don't have to follow any coding directive.

The handling of the modules and their configuration parameters is organized in Seismon using projects and collections. Before working with Seismon modules, a project has to be created. This also initializes all needed database tables which is

done by calling the package interface function prefix database.m. Within a project, one or several collections can be created. A collection can hold a set of modules and their related configuration parameters. Figure 13.3 gives an overview of the structure of a collection and the possible data flows within the modules of the collection. For each module, there are two data flows. The edit data flow (green in figure 13.3) is used to change the configuration parameters of a module using the edit function. The execution data flow (purple in figure 13.3) runs when a collection is executed by the user. This flow passes the configuration data of each module to according command function. The command function executes it's algorithms using the configuration data as an input and returns some output values. These output parameters are passed to the next module in the collection as an input data. This enables a flow-like behaviour of the collection.

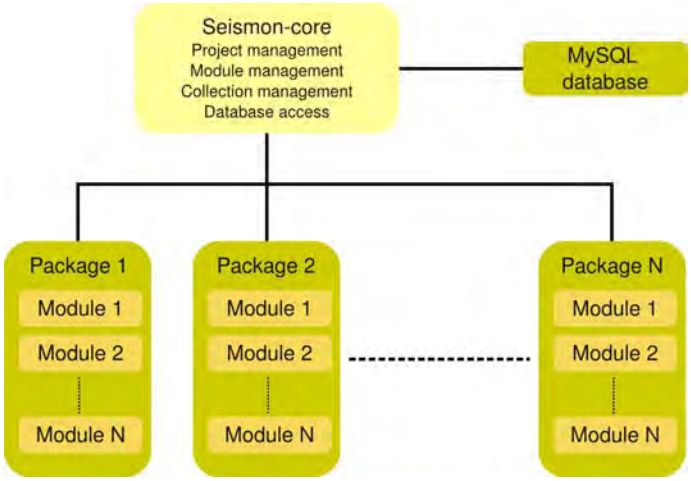

Figure 13.1: The modular design approach of Seismon. The Seismon-core manages the database communication and the packages and modules. A package is a collection of modules which provide the functionality (e.g. waveform display, event management,..) to Seismon.

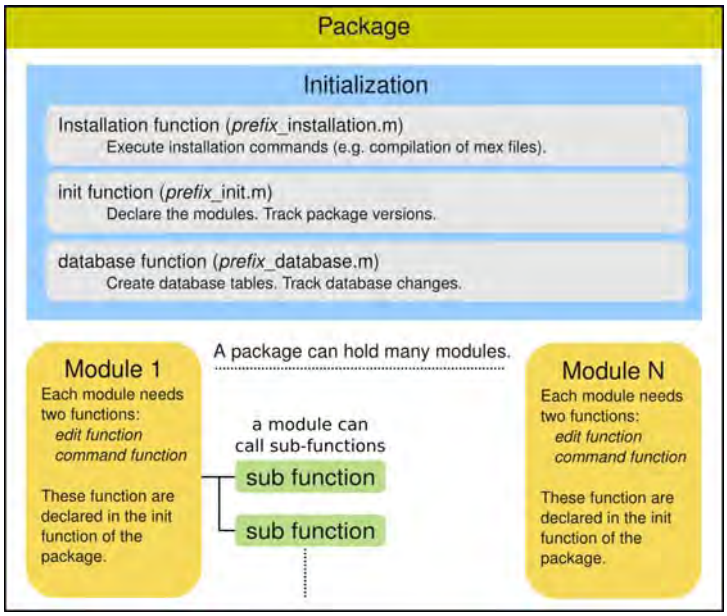

Figure 13,2: The general structure of a Seismon package.

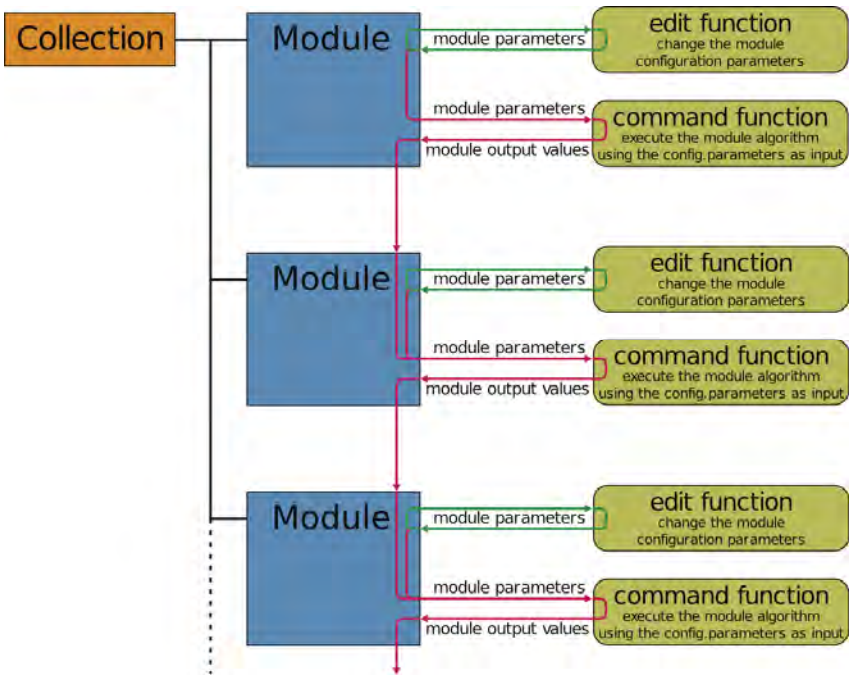

Figure 13.3: A collection is used to combine one or more modules for editing and execution. The parameters of a module can be edited using the edit function. The command function is called when the collection is executed. The module parameters are passed to the command function which returns some output values. These output values are passed to the next module in the collection and can be used by the related command function.

13.2 Use of Seismon within other projects

Seismon is intended to act as a tool supporting the work within scientific research projects. Seismon can be used to easily integrate new processing algorithms into a quasi-routine work flow. The following application examples show different projects which used or are still using Seismon, demonstrating the wide field of its possible application. The application to seismic monitoring of landslides has been extensively described in this report and therefore is not included in the following list.

Local earthquake monitoring
Within the project ALPAACT, founded by the Austrian Academy of Sciences (OEAW), Seismon is used for data management and earthquake analysis. Seismon is used as a post-processing tool after an automatic event detection done with the Earthworm software. Seismon also was used for local earthquake analysis within the CBP and ALPASS[36] projects. An example screenshot is given in figure 13.4.

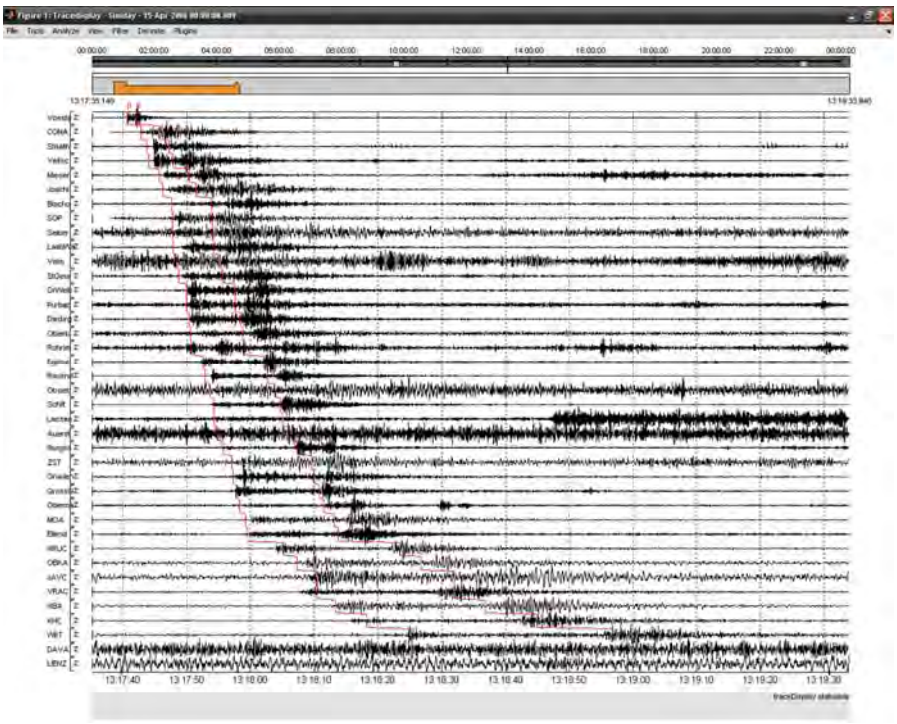

Figure 13.14: Example screenshot of Seismon used for the analysis of local earthquake data.

Permafrost mapping

Small scale active seismic experiments to map the permafrost in alpine valleys were processed using Seismon[37]. For this purpose, newly developed algorithms were integrated into Seismon. Figure 13.15 gives an example of the usage of Seismon for the processing of active seismic data for the characterization of permafrost sites.

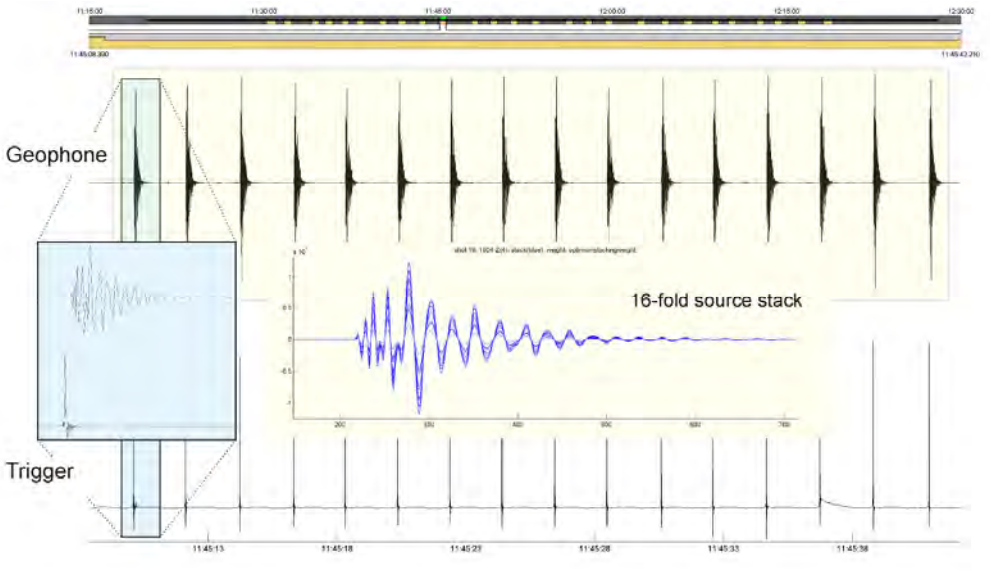

Figure 13.15: Example usage of Seismon for the processing of active seismic data used for the characterization of permafrost sites.

Tunnel seismic while drilling (TSWD)
Seismon was used to manage and analyze the data of a tunnel seismic while drilling (TSWD) pilot study in cooperation with Pöyry Infra GmbH, Salzburg. New algorithms were developed and tested using Seismon[38].

Seismic noise interferometry
Seismon was used by Behm & Snieder[39] as the base-software to develop methods for seismic noise interferometric analysis. Seismon provided the tools for data management, data visualization and quality control. The event processing tools were extended and a complete work-flow for seismic noise interferometry was developed and added to Seismon as a Seismon package.

References

1. Zangerl, C., Eberhardt, E., Schönlaub, H. & Anegg, J. in Rock Mechanics: Meeting Society's Challenges and Demands (Eberhardt, Stead & Morrison) – (Tylor & Francis Group, 2007).
2. Brückl, E. et al. The Gradenbach Observatory - monitoring deep-seated gravitational slope deformation by geodetic, hydrological, and seismological methods. Landslides 1–15 (2013). doi:10.1007/s10346-013-0417-1
3. Moser, M. & Glumac, S. Geotechnische Untersuchungen zum Massenkriechen in Fels am Beispiel des Talzuschubes Gradenbach (Kärnten). Verh. Geol. B.-A. **3,** 209–241 (1983).
4. Brückl, E., Brunner, F. K. & Kraus, K. Kinematics of a deep-seated landslide derived from photogrammetric, GPS and geophysical data. Engineering Geology **88,** 149 – 159 (2006).
5. Brückl, E. Bericht über seismische Untersuchungen im Bereich des Talzuschubes im Gradenbach. Mitteilung der forstlichen Bundesversuchsanstalt **153,** 69–73 (1984).
6. Brückl, E. & Brückl, J. Geophysical models of the Lesachriegel and Gradenbach deep-seated mass-movements (Schober range, Austria). Engineering Geology **83,** 254–272– (2006).
7. Mertl, S. Characterization of local seismic events on the deep-seated gravitational slope deformation Gradenbach. (in appraisal).
8. Heissel, G. & Mostler, H. Geoforum Umhausen Band 3. (2005).
9. Weginger, S. Detektion und Lokalisierung seismischer Signale zur Überwachung der Massenbewegung Steinlehnen. (Master Thesis, Vienna University of Technology, 2012).
10. Mertl, S. & Brückl, E. Hazard estimation of deep seated mass movements by microseismic monitoring - final report 2004 - 2008. (Vienna University of Technology, 2008).
11. Bormann, P. IASPEI New Manual of Seismological Observatory Practice (NMSOP). (GeoForschungsZentrum Potsdam, 2002).
12. Lomax, A., Michelini, A. & Curtis, A. in Encyclopedia of Complexity and Systems Science (Meyers, R. A.) 2449–2473 (Springer New York, 2009). at <http://dx.doi.org/10.1007/978-0-387-30440-3_150>
13. Lomax, A., Virieux, J., Voant, P. & Berge, C. in Advances in Seismic Event location (Thurber, C. N. & Rabinowitz, N.) 101 – 134 (Kluwer Academic Publishers, 2000).
14. Brückl, E. & Parotidis, M. Prediction of slope instabilities due to deep-seated gravitational creep. Natural hazards and earth system sciences **5,** 155–172– (2005).
15. Müller, M., Brunner, F. K. & Lang, E. Long term measurement and analysis of a deep-seated mass movement. in 5th Int. Conf. on Engineering Surveying - INGEO, Brijuni, Croatia (2011).
16. Draxler, A. Seismic Noise Analysis at the Gradenbach Landslide. (Master thesis Vienna University of Technology, ,2013).
17. McNamara, D. E. & Buland, R. P. Ambient Noise Levels in the Continental United States. Bulletin of the Seismological Society of America **94,** 1517–1527

(2004).
18. Doblhoff-Dier, K. Seismic signal analysis using polarization attributes and its applications. (Master Thesis, Vienna University of Technology, 2011).
19. Doblhoff-Dier, K. Implementation of a polarization analysis for Seismon. 34 (Vienna University of Technology, 2010).
20. Flinn, E. A. Signal analsis using rectilinearity and direction of particle motion. Proceedings of the IEEE **53,** 1874–1876 (1965).
21. Vidale, J. E. Complex polarization analy sis of particle motion. Bulletin of the Seismological Society of America **76,** 1393–1405 (1986).
22. Samson, J. C. & Olson, J. V. Data-adaptive polarization filters for multichannel geophysical data. Geophysics **46,** 1423–1431 (1981).
23. Schimmel, M. & Gallart, J. The use of instantaneous polarization attributes for seismic signal detection and image enhancement. Geophys. J. Int. **155,** 653–668– (2003).
24. Stockwell, R. G., Mansinha, L. & Lowe, R. P. Localization of the complex spectrum: the S transform. Signal Processing, IEEE Transactions on **44,** 998–1001 (1996).
25. Pinnegar, C. R. Polarization analysis and polarization filtering of three-component signals with the time-frequency S transform. Ge **165,** 596–606 (2006).
26. Köhler, A., Ohrnberger, M. & Scherbaum, F. Unsupervised feature selection and general pattern discovery using Self-Organizing Maps for gaining insights into the nature of seismic wavefields. Computers & Geosciences **35,** 1757–1767 (2009).
27. Allen, R. Automatic earthquake recognition and timing from single traces. Bulletin of the Seismological Society of America **68,** 1521–1532– (1978).
28. Allen, R. Automatic phase pickers: their present use and future prospects. Bulletin of the Seismological Society of America **72,** S225–S242– (1982).
29. Gonzalez, R. C., Woods, R. E. & Eddins, S. L. Digital Image Processing Using Matlab. (Pearson Prentice Hall, 2004).
30. Pitman, B. E., Patra, A., Calder, E. S., Bian, X. & Smith, P. Energy Approach of Localization of Volcanic Rockfall Source of SHV, Montserrat.
31. Jolly, A., Thompson, G. & Norton, G. . Locating pyroclastic flows on Soufriere Hills Volcano, Montserrat, West Indies, using amplitude signals from high dynamic range instruments. Journal of Volcanology and Geothermal Research **118,** 299–317 (2002).
32. Gustafsson, F. & Gunnarsson, F. Positioning using time-difference of arrival measurements. in 2003 IEEE International Conference on Acoustics, Speech, and Signal Processing, 2003. Proceedings. (ICASSP '03) **6,** VI–553–6 vol.6 (2003).
33. Daku, B. L. F., Salt, J. E. & Sha, L. An algorithm for locating microseismic events. in Canadian Conference on Electrical and Computer Engineering, 2004 **4,** 2311–2314 Vol.4 (2004).
34. Kruse, R., Gebhardt, J. & Klawonn, F. Fuzzy-Systeme. (Teubner B.G. GmbH, 1995).
35. Kennet, B. L. N. The Seismic Wavefield. (Cambridge University Press, 2002).
36. Hausmann, H. et al. New seismic data improve earthquake location in the Vienna Basin area, Austria_. Austrian Journal of Earth Sciences **103,** 2–14

(2010).
37. Hausmann, H., Krainer, K., Staudinger, M. & Brückl, E. Continuous recording of seismic signals in Alpine permafrost. in EGU General Assembly Conference Abstracts **11,** 10330 (2009).
38. Brückl, E., Chwatal, W., Mertl, S. & Radinger, A. Exploration Ahead of a Tunnel Face by TSWD-Tunnel Seismic While Drilling. Geomechanics and Tunnelling **5,** 460–465 (2008).
39. Behm, M. & Snieder, R. Love waves from local traffic noise interferometry. The Leading Edge **32,** 628–632 (2013).